# High Speed Electron Microscopy

## Engineering of a commercial multi-beam scanning electron microscope with transmission imaging

Zuidema, W.

**DOI**
10.4233/uuid:bd8a8edb-3ccb-4f2f-9212-bc6e14af41bb

**Publication date**
2023

**Document Version**
Final published version

**Citation (APA)**
Zuidema, W. (2023). *High Speed Electron Microscopy: Engineering of a commercial multi-beam scanning electron microscope with transmission imaging*. [Dissertation (TU Delft), Delft University of Technology]. https://doi.org/10.4233/uuid:bd8a8edb-3ccb-4f2f-9212-bc6e14af41bb

# HIGH SPEED ELECTRON MICROSCOPY

ENGINEERING OF A COMMERCIAL MULTI-BEAM SCANNING ELECTRON MICROSCOPE WITH TRANSMISSION IMAGING

## Proefschrift

ter verkrijging van de graad van doctor
aan de Technische Universiteit Delft,
op gezag van de Rector Magnificus prof.dr. ir. T.H.J.J. van der Hagen
voorzitter van het College voor Promoties,
in het openbaar te verdedigen op 13 november 2023 om 15:00 uur.

door

**Wilco ZUIDEMA**

Master of Materials Science and Engineering, Technische Universiteit Delft, Nederland
geboren te het Bildt, Nederland.

Dit proefschrift is goedgekeurd door de promotoren.

Samenstelling promotiecommissie bestaat uit:

| | |
|---|---|
| Rector Magnificus | Voorzitter |
| em. prof. dr. ir. P. Kruit | Technische Universiteit Delft, promotor |
| dr. ir. J.P. Hoogenboom | Technische Universiteit Delft, copromotor |

Onafhankelijke leden:

| | |
|---|---|
| prof. dr. ir. J.L. Herder | Technische Universiteit Delft |
| prof. dr. F.P.J. Schuurmans | Universiteit Twente |
| prof. dr. S. Stallinga | Technische Universiteit Delft |
| dr. B.N.G. Giepmans | Universitair medisch centrum Groningen |
| dr. A.M.G. Mohammadi Gheidari | Thermo Fisher Scientific |

*Keywords:* Electron Microscopy, High-Throughput, Multibeam, Transmission imaging

*Printed by:*

*Front & Back:* AI generated



ISBN 000-00-0000-000-0

An electronic version of this dissertation is available at
http://repository.tudelft.nl/.


# CONTENTS

**Summary** **vii**

**Samenvatting** **ix**

**1 Introduction** **1**
1.1 High-throughput imaging . . . . . 1
1.2 Options for high-throughput imaging . . . . . 3
1.3 Multibeam systems at the Delft University of Technology. . . . . 4

**2 Detection system** **9**
2.1 Introduction . . . . . 9
2.2 Model . . . . . 12
2.2.1 Performance parameters. . . . . 12
2.2.2 Monte Carlo model setup . . . . . 15
2.3 Monte Carlo simulation of the model sample . . . . . 17
2.3.1 Analytical model . . . . . 23
2.4 Experimental setup for model verification . . . . . 25
2.5 Experimental results . . . . . 26
2.6 Resolution loss . . . . . 31
2.7 Summary and conclusions . . . . . 33

**3 Considerations for transmission detection** **41**
3.1 Introduction . . . . . 41
3.2 Detector selection . . . . . 41
3.3 Scintillator selection . . . . . 45
3.4 Scintillator and coating surface quality. . . . . 51
3.4.1 Scintillator surface defects. . . . . 52
3.4.2 Coating defects (granularity) . . . . . 52
3.5 Scintillator saturation . . . . . 53
3.5.1 Model . . . . . 56
3.5.2 CNR and SNR when imaging with a saturated scintillator. . . 59
3.5.3 Dark field imaging . . . . . 60
3.5.4 Dopant concentration inhomogeneity . . . . . 61
3.5.5 Saturation reduction . . . . . 62
3.6 Summary and conclusion . . . . . 62

**4 Hardware for the image acquisition in multi-beam STEM** **67**
4.1 Introduction . . . 67
4.2 Detector selection . . . 68
4.3 Crosstalk . . . 69
4.4 Stage . . . 71
4.4.1 Stage scan combined with beam scan . . . 71
4.4.2 Beam scan and optical de-scan . . . 82
4.5 Light optics and de-scan . . . 85
4.5.1 Optics . . . 85
4.5.2 De-scan . . . 86
4.5.3 Galvanometer performance . . . 88
4.5.4 Scan pattern . . . 91
4.6 Summary and Conclusions . . . 93

**5 Multi-beam imaging in the FAST-EM prototype** **99**
5.1 Introduction . . . 99
5.2 Electron optical and light optical system . . . 100
5.2.1 Microscope setup . . . 100
5.2.2 Detector . . . 104
5.2.3 Test samples . . . 104
5.3 Alignment and calibration . . . 105
5.3.1 Light optical alignment . . . 105
5.3.2 Electron optical alignment . . . 109
5.3.3 Resolution . . . 115
5.4 Imaging . . . 117
5.4.1 Dark level and gain calibration . . . 117
5.4.2 Mega-field imaging . . . 118
5.5 Conclusion . . . 120
5.6 Acknowledgments . . . 121

**6 Valorization of the Delft Multi Beam SEM** **125**
6.1 Final FAST-EM Configuration . . . 127

**7 Conclusion** **129**

**Acknowledgements** **133**

**List of Publications** **135**

# SUMMARY

In this thesis, the design and engineering considerations for a multi-beam scanning electron microscope (MBSEM) are discussed. This microscope can benefit biological research in various ways. It can give new insights into the inner workings of a multitude of biological systems that were hard to get using previously existing instrumentation. For instance, a higher throughput gives the option to do statistical analysis of multiple samples instead of drawing conclusions from only one. The goal of this thesis was to get from a proof of principle to a final system that can actually be used to do the research. It is divided into 5 chapters showing a step-by-step process of getting to the final system as it is now on the market.

Chapter 1 is an introduction to the subject showing the current state of the art with respect to high throughput imaging.

Chapter 2 Describes a novel imaging method in scanning electron microscopes. This chapter does not focus on the multi-beam application but shows it in the context of the often-used backscatter imaging. In this method, we place the tissue section directly on top of a thin scintillator screen (thinner than 200 μm) which is coated with a conductive layer. The light signal generated by the electrons transmitted through the sample is collected by a high NA objective lens and the light is imaged onto a photon detector outside of the vacuum chamber. A noise model is created to calculate the signal-to-noise ratio and the contrast-to-noise ratio of this imaging method. It shows that the best images are generated around a landing energy of about 5keV. There are some dependencies on sample thickness, staining level, and light collection efficiency which are also explored. This method does lower the resolution in the image to some extent (by a factor of 2 at low energies and thick sections), which is shown at the end of the chapter.

Chapter 3 Goes into the considerations that have to be taken into account when dealing with the imaging method from chapter 2. This chapter is applicable to a single beam SEM as much as an MBSEM. A list of possible light detectors is given from which silicon photomultipliers are selected as the best candidate for the MBSEM. Combined with the light detector, multiple options for a scintillator were discussed, from which YAG:CE is selected. Organic scintillators are discarded due to their bleaching behavior due to electron beam irradiation. The surface of the scintillator and the coating layer are shown to have a large impact on image quality. For this reason, the scintillators are ion-beam polished and

coated with a Boron layer. Unexpected behavior in the form of scintillator saturation is observed which is then described by a model and connected to the noise model from chapter 2.

Chapter 4 Gives an analysis of all the hardware requirements for a MBSEM. First a measurement of the crosstalk as a function of landing energy and pitch. It is found that a crosstalk of at least 10 % is to be expected in the system. Next, an overview is given for all the parameters that are related to the stage and the light optics. These are then related to the final throughput of the system. Two imaging strategies are described, in one the beam scans in one direction and the stage in the other. In the other strategy, the beams scan like in a regular SEM and are subsequently descanned in the light-optical system. It is found that with a step and scan approach in combination with planned beam shifts, the maximum throughput that can be achieved is around 420 mpix/s.

Chapter 5 Shows results from the final prototype system. Alignments are of great importance in any SEM but even more so in the MBSEM. Therefore a large part of this chapter is dedicated to describing this alignment. This starts with the electron optical alignment of the source and the beam through the column. The grid of beams has to be optimized to show as little as possible distortions to improve system throughput. The scan and descan have to be aligned to the grid axes and the amplitude has to be precisely correct. The beams have to be perfectly aligned to the detector array. On the processing side, a description of how can be compensated for varying dark and gain levels in the detector array. In the end, a final image is shown, consisting of 400 megapixels.

Chapter 6 Describes the valorization of the project and all the challenges and choices that were involved.

# SAMENVATTING

In dit proefschrift worden het ontwerp en de technische overwegingen voor een multi-beam scanning electron microscoop (MBSEM) besproken. Deze microscoop kan het biologisch onderzoek op verschillende manieren ten goede komen. Hij kan nieuwe inzichten verschaffen in de innerlijke werking van een groot aantal biologische systemen die moeilijk te verkrijgen waren met eerder bestaande instrumenten. Een hogere verwerkingscapaciteit geeft bijvoorbeeld de mogelijkheid om statistische analyses van meerdere monsters uit te voeren in plaats van conclusies te trekken uit slechts één monster. Het doel van dit proefschrift was om van een proof of principle te komen tot een definitief systeem waarmee het onderzoek daadwerkelijk kan worden uitgevoerd. Het is verdeeld in 5 hoofdstukken die een stap-voor-stap proces laten zien om te komen tot het uiteindelijke systeem zoals het nu op de markt is.

Hoofdstuk 1 is een inleiding tot het onderwerp met de huidige stand van de techniek op het gebied van high throughput imaging.

Hoofdstuk 2 Beschrijft een nieuwe beeldvormingsmethode in rasterelektronenmicroscopen. Dit hoofdstuk richt zich niet op de multi-beam toepassing maar toont deze in de context van de vaak gebruikte backscatter beeldvorming. Bij deze methode wordt de weefselsectie direct bovenop een dun scintillatorscherm geplaatst (dunner dan 200 $upmu$m) dat is bekleed met een geleidende laag. Het lichtsignaal van de elektronen die door het monster worden gestuurd, wordt opgevangen door een objectief met hoge NA-waarde en het licht wordt afgebeeld op een fotondetector buiten de vacuümkamer. Er is een ruismodel opgesteld om de signaal-ruisverhouding en de contrast-ruisverhouding van deze beeldvormingsmethode te berekenen. Hieruit blijkt dat de beste beelden worden gegenereerd rond een landingsenergie van ongeveer 5keV. Er zijn enkele afhankelijkheden van monsterdikte, kleuring en lichtopvangefficiëntie die ook worden onderzocht. Deze methode verlaagt de resolutie in het beeld enigszins (met een factor 2 bij lage energieën en dikke secties), hetgeen aan het eind van het hoofdstuk wordt aangetoond.

Hoofdstuk 3 Gaat in op de overwegingen waarmee rekening moet worden gehouden bij de beeldvormingsmethode uit hoofdstuk 2. Dit hoofdstuk is zowel van toepassing op een single beam SEM als op een MBSEM. Er wordt een lijst van mogelijke lichtdetectoren gegeven waaruit silicium fotomultipliers worden geselecteerd als de beste kandidaat voor de MBSEM. In combinatie met de licht-

detector zijn meerdere opties voor een scintillator besproken, waaruit YAG:CE is gekozen. Organische scintillatoren worden terzijde geschoven vanwege hun blekende gedrag als gevolg van bestraling met elektronenbundels. Het oppervlak van de scintillator en de coatinglaag blijken een grote invloed te hebben op de beeldkwaliteit. Daarom zijn de scintillatoren met ionenstralen gepolijst en voorzien van een Boron-laag. Onverwacht gedrag in de vorm van verzadiging van de scintillator wordt waargenomen, dat vervolgens door een model wordt beschreven en gekoppeld aan het ruismodel uit hoofdstuk 2.

Hoofdstuk 4 Geeft een analyse van alle hardware vereisten voor een MBSEM. Eerst een meting van de overspraak als functie van landingsenergie en toonhoogte. Het blijkt dat een overspraak van minstens 10 procent te verwachten is in het systeem. Vervolgens wordt een overzicht gegeven van alle parameters die betrekking hebben op het podium en de lichtoptiek. Deze worden vervolgens gerelateerd aan de uiteindelijke verwerkingscapaciteit van het systeem. Er worden twee beeldvormingsstrategieën beschreven: bij de ene scant de bundel in één richting en de tafel in de andere. In de andere strategie scant de bundel zoals in een gewone SEM en wordt vervolgens in het lichtoptisch systeem afgetast. Het blijkt dat met een step and scan-aanpak in combinatie met geplande bundelverschuivingen een maximale verwerkingscapaciteit van ongeveer 420 mpix/s kan worden bereikt.

Hoofdstuk 5 Toont de resultaten van het uiteindelijke prototype. Uitlijningen zijn van groot belang in elke SEM, maar nog meer in de MBSEM. Daarom is een groot deel van dit hoofdstuk gewijd aan de beschrijving van deze uitlijning. Dit begint met de optische uitlijning van de bron en de bundel door de kolom. Het raster van bundels moet worden geoptimaliseerd om zo weinig mogelijk vervormingen te vertonen en zo de doorvoer van het systeem te verbeteren. De scan en descan moeten worden uitgelijnd op de rasterassen en de amplitude moet precies kloppen. De stralen moeten perfect zijn uitgelijnd op de detector array. Aan de verwerkingszijde wordt beschreven hoe kan worden gecompenseerd voor wisselende donker- en versterkingsniveaus in de detector array. Uiteindelijk wordt een eindbeeld getoond van 400 megapixels.

Hoofdstuk 6 Beschrijft de valorisatie van het project en alle uitdagingen en keuzes die daarbij kwamen kijken.

# 1

# INTRODUCTION

In this thesis, the design of a multi-beam scanning electron microscope will be discussed. The research in this thesis was started in succession of multiple other PhD students, most notably Mohammadi-Gheidari [1] and Ren [2]. This thesis is, more so than these works above, focused on high-throughput imaging and less on the electron optics required to do so.

## 1.1. HIGH-THROUGHPUT IMAGING

In electron microscopy, the speed of imaging is fundamentally limited by the signal-to-noise ratio (SNR). An electron microscopy image is only interpretable when the SNR is sufficiently high (and the image has enough contrast). The signal-to-noise ratio of the image is determined by the electron dose per pixel and the detector electronics. The electron dose per pixel in scanning electron microscopy (SEM) at a certain dwell time (or exposure time in the case of transmission electron microscopy (TEM)) is limited by the maximum current in the probe of a certain size[1]. The aberrations of the final lens limit this current. In theory, these aberrations can be corrected by using complex optical elements [3]. This is, however, not an easy endeavor, quite costly, and is therefore not readily available on the market. Also, in a lot of cases, the speed of imaging is not a large issue. For instance, a materials scientist investigating a crack surface wants an answer to a very specific question and does not need to make a 3D view of the whole material in which the crack arose. In biology (the focus of this thesis), a single event is often considered not to be enough proof, but a 3D stack of the

[1] Note that with TEM, we refer to wide-field illumination and not Scanning TEM which pixel-by-pixel illumination like SEM

whole tissue takes too long to acquire; therefore, the work is very tedious to find enough events in areas that are suspected to show them.

There are, however, fields in which low throughput is an issue. The most notable of which are semiconductor inspection and 3D tissue imaging. In semiconductor inspection, a whole wafer or reticle (mask) has to be inspected. A reticle is usually quite small ( 30mm in the lateral dimensions) and has fairly large features [4]. The imaging will take a few days at a 20nm pixel resolution and a 25ns dwell time. A whole 300mm wafer will, however, take ten months at the same dwell time and an 8nm pixel resolution. The wafer can consist of hundreds of layers, of which quite a few might have to be inspected at high resolution.

When 3D imaging of biological tissue is considered, the required time increases rapidly. When a volume of tissue is imaged, it has to be cut into very thin slices. This can be done using a knife (microtome) or a focused ion beam (FIB). The z-resolution is limited by what thickness these sections can have: 40nm for microtomy and 10nm for FIB milling. Assuming a section of 1 $mm^2$, 40nm thickness, and a 4nm pixel size at a dwell time of 1 $\mu$s, the imaging of a square millimeter will take 17 hours. About 25,000 sections of 40nm are required to image a cubic millimeter, which results in an imaging time of about 50 years. A mouse brain is around 400 $mm^2$ and will thus take 20 millennia to image. This goal is, with normal scanning electron microscopy, unattainable.

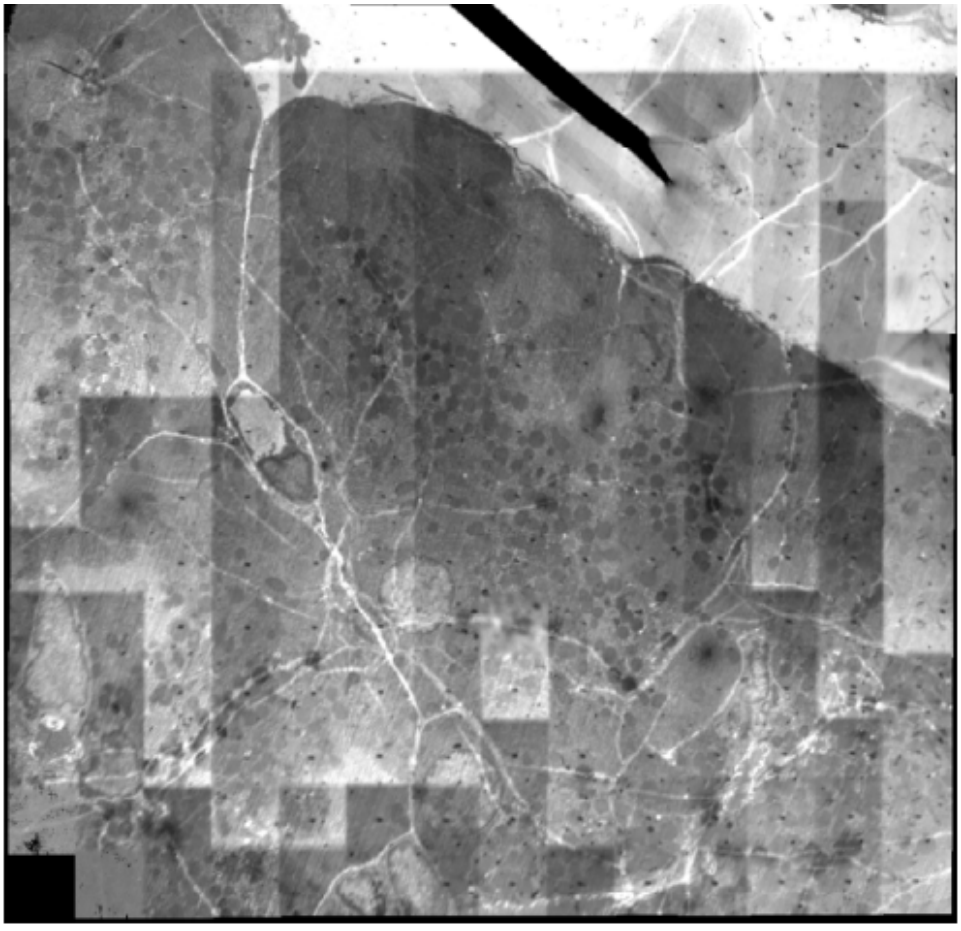

Figure 1.1: Image from Ren [2], showing transmission electron imaging of rat pancreas tissue in the TU Delft multi-beam prototype. The image shows a 14x14 beam image grid, imaged at a 15keV landing energy.

## 1.2. OPTIONS FOR HIGH-THROUGHPUT IMAGING

The main way to gain throughput in electron microscopy is by parallelizing the imaging. This can be done by using multiple beams in the same system. Another way is to use a TEM with a relatively high current density at the sample and a big camera [5]. For wafer and reticle inspection, work is progressing towards building very complex machines with over 100,000 beams scanning in parallel [6], [7]. The semiconductor tool company ASML has shown the first results with a system containing nine beams and is planning to scale up [8]. Other companies in the market, like Applied Materials (in collaboration with the Delft University of

Technology) and KLA Tencor, are working towards similar machines.

These machines, however, will not be useful for 3D imaging of tissue. This is mainly caused by the very specific use case they are built for and the high investment cost, estimated to be in the tens of millions. An exception to this is the MultiSEM released by Zeiss, which, even though still quite expensive, can be used to image biological tissue as well as semiconductor wafers [9].

Other than the MultiSEM, the only other commercially available high-throughput system is the VOXA blade solution. This system is based on the TEMCA developed at the Janelia research campus. It is a retrofit system to an existing TEM, which replaces the standard sample holder with a grid-tape system. This tape contains a row of apertures on which sections can be placed using an ultramicrotome (see figure figure 1.2b). The camera in the TEM is replaced by one with a 50Mpix camera, increasing the imaging area greatly. The amount of current that is used to image causes some blurring in the image, but the resolution is still very good compared to a standard SEM image. The maximum sustained throughput of both these systems seems limited to around 100-200Mpix/s and is limited by various overheads, foremost of which is the stage settling time [10], [11].


(a) (b)

Figure 1.2: Pictures of the Voxa blade system, (a) showing the reel-to-reel system, and (b) a zoom-in of the grid tape [12], [13].

## 1.3. MULTIBEAM SYSTEMS AT THE DELFT UNIVERSITY OF TECHNOLOGY

At the Delft University of Technology (TUD), the development of multi-beam systems started in 2003 with Martijn van Bruggen [14]. From then on, all prototypes were built by adjusting an FEI NovaNanoSEM. The first one was developed for electron beam-induced deposition (EBID) in combination with a multi-beam blanker. This blanker was found to be hard to align with the source, and this idea was discarded. Without the beam blanker, but still intended for EBID,

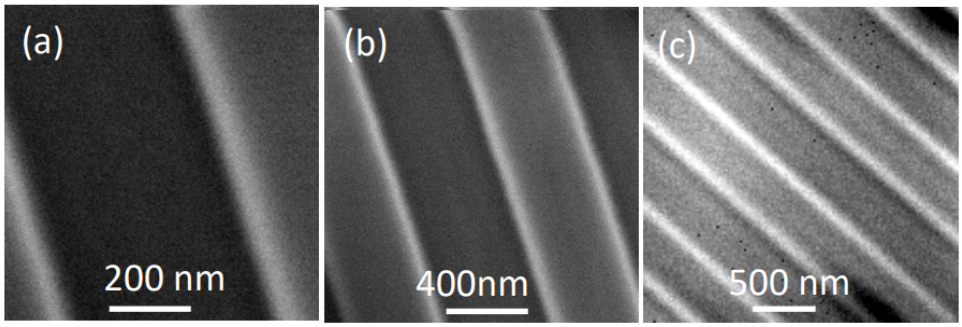


Figure 1.3: Image from Ren [2], showing secondary electron imaging in the TU Delft multi-beam prototype.

Mohammadi-Gheidari [1] added the first version of the transmission imaging as it is described in this thesis. Using this imaging modality, proof was obtained that a similar resolution could be obtained in the MBSEM as in a regular SEM. The last doctoral student to work on this subject before this thesis was Ren [2]. He showed it was possible to do secondary electron imaging in the MBSEM, as can be seen in figure 1.3. More importantly, from the perspective of this work, he furthered the idea of transmission imaging of tissue (figure 1.1). This last imaging method is performed by placing a tissue section directly on top of a scintillator and collecting the signal using an optical microscope underneath the scintillator. This method showed highly promising initial results, and therefore, the goal was set for this PhD thesis to design and build a prototype MBSEM for transmission imaging of thin tissue sections and explore the further development towards a commercial product. This means that several key questions on the novel technique for image formation had to be addressed:

- What are the benefits of this imaging modality, and how does it stack up to other modalities?
- What are the limitations of this imaging modality, and what practical issues might one encounter when using this routinely?
- What are the parameters influencing signal and contrast generation with this imaging modality, and what contrast can we expect with transmission imaging of tissue sections on a scintillator?
- What is an optimized setup in terms of optical path and detector for parallel, high-speed detection of the signal generated in the scintillator by each beamlet?

In addition, integration of the novel detection technique with the MBSEM system leads to system-level questions:

- How can this academic prototype be made into a commercial system?
  - What design choices have to be made in order to simplify the development?
  - What alignments and calibrations have to be automated for users?
- What is the maximum throughput of the entire system, and what parameters can be tuned to optimize throughput?

These and related questions will be addressed in the next five chapters, ultimately leading to a prototype multi-beam transmission electron microscope now known as FAST-EM.

# BIBLIOGRAPHY


[1] A. Mohammadi-Gheidari, *PhD Thesis: 196 Beams in a Scanning Electron Microscope*. 2013, ISBN: 9789461919854.

[2] Y. Ren, *PhD Thesis: Imaging Systems for the Delft Multi- Beam Scanning Electron Microscope 1*. 2017, ISBN: 9789462957114. DOI: 10.4233/uuid.

[3] H. Dohi and P. Kruit, "Design for an aberration corrected scanning electron microscope using miniature electron mirrors", *Ultramicroscopy*, vol. 189, pp. 1–23, 2018.

[4] M. Lercel, C. Smeets, M. van der Kerkhof, A. Chen, T. van Empel, and V. Banine, "Euv reticle defectivity protection options", in *Photomask Technology 2019*, International Society for Optics and Photonics, vol. 11148, 2019, 111480Y.

[5] Z. Zheng, J. S. Lauritzen, E. Perlman, *et al.*, "Resource A Complete Electron Microscopy Volume of the Brain of Adult Drosophila melanogaster A Complete Electron Microscopy Volume of the Brain of Adult Drosophila melanogaster", *Cell*, pp. 1–14, 2018, ISSN: 0092-8674. DOI: 10.1016/j.cell.2018.06.019. [Online]. Available: https://doi.org/10.1016/j.cell.2018.06.019.

[6] W. Ren, X. Liu, X. Hu, *et al.*, "Multi-beam technology for defect inspection of wafer and mask", in *35th European Mask and Lithography Conference (EMLC 2019)*, International Society for Optics and Photonics, vol. 11177, 2019, p. 111770D.

[7] E. Ma, W. Ren, X. Luo, *et al.*, "Multi-beam inspection (mbi) development progress and applications", in *Metrology, Inspection, and Process Control for Microlithography XXXIV*, International Society for Optics and Photonics, vol. 11325, 2020, 113250F.

[8] E. Ma, K. Chou, X. Liu, *et al.*, "Cutting edge multiple beam technology for euv era: Latest development progress and application", in *Metrology, Inspection, and Process Control for Microlithography XXXII*, International Society for Optics and Photonics, vol. 10585, 2018, p. 1 058 535.

[9] J. T. Neumann, T. Garbowski, W. Högele, *et al.*, "High-throughput multibeam SEM: quantitative analysis of imaging capabilities at IMEC-N10 logic node", *Metrology, Inspection, and Process Control for Microlithography XXXI*, vol. 10145, no. March 2017, 101451S, 2017. DOI: 10.1117/12.2257980.

[10] W. Yin, D. Brittain, J. Borseth, *et al.*, "A petascale automated imaging pipeline for mapping neuronal circuits with high-throughput transmission electron microscopy", *Nature Communications*, vol. 11, no. 1, pp. 1–12, 2020.

[11] R. Schalek, D. Lee, N. Kasthuri, *et al.*, "Imaging a 1 mm 3 volume of rat cortex using a multibeam sem", *Microscopy and Microanalysis*, vol. 22, no. S3, pp. 582–583, 2016.

[12] *Luxel's gridtape® tem supports, https://luxel.com/gridtape/ jan-2022*, Jan. 2021. [Online]. Available: https://luxel.com/gridtape/.

[13] *Blade, https://www.voxa.co/solutions/blade, feb-2022*, Mar. 2022. [Online]. Available: https://www.voxa.co/solutions/blade.

[14] M. J. Van Bruggen, *PhD Thesis: Multi-electron beam system for high resolution electron beam induced deposition*. 2008.

# 2

# DETECTION SYSTEM

## 2.1. INTRODUCTION

In the last decade, there has been a major push for large-volume scanning electron microscopy, of which the most striking example is full brain connectomics [1], [2]. This development was made possible by the ability to store the large datasets involved, as well as by the increasing work being done on automatic segmentation of this data [3]–[6]. The throughput speed in SEM imaging is limited by the maximum probe current allowable to obtain a desired resolution. This limitation can be circumvented by employing multiple beams in one SEM. In these Multi-Beam SEMs (MBSEM), the maximum throughput is governed primarily by the number of beams and detector bandwidth. The current per beam is still limited, but the theoretical throughput speed scales linearly with the number of beams. The ZEISS MultiSEM has already been available for some time, which has up to 91 beams (up to 331 beams proven [7]) with secondary electron (SE) detection [8], [9]. Delft University of Technology has, over the past decade, developed an MBSEM with 196 beams [10].

Signal detection in the MBSEM with regular detectors is impossible. In such microscopes, the signal generated by each beam has to be physically separated. In the ZEISS MultiSEM, this is performed by focusing the secondary electrons from the sample, through a separate optical system, onto a detector array. In our MBSEM, with 64 beams, we employ a transmission imaging technique that makes for a relatively straightforward separation of the signals created by the multiple beams [11]. This circumvents the need for extra electron optics and leaves the SEM column unchanged. The imaging is performed with a low energy

Part of this chapter was published in: Zuidema, W., Kruit, P. (2020). Transmission imaging on a scintillator in a scanning electron microscope. Ultramicroscopy, 218, 113055.

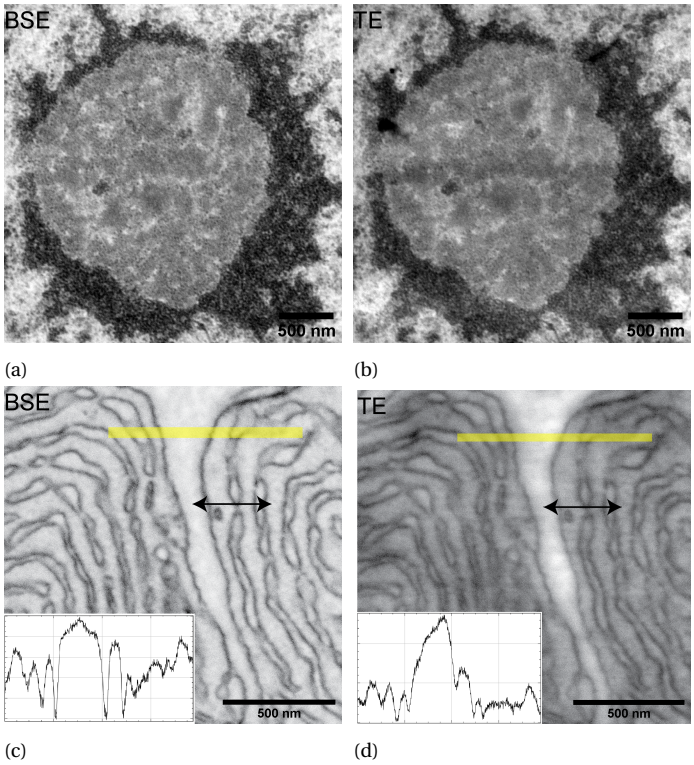


Figure 2.1: SEM image of a nucleolus(a,b) and endoplasmic reticulum and cytoplasm(c,d) in rat pancreas, (a,c) (inverted)backscatter compared to (b,d) transmission imaging. Images a and b were acquired with a landing energy of 4keV, and c and d were acquired at 3.5keV. All images were stretched to full dynamic range and acquired at a 16-bit pixel depth. (a,b) show similar contrast where the images (c,d) show that the contrast in transmission imaging can be greatly different from backscatter imaging, as indicated by the arrow. This is illustrated by the line profile taken along the yellow line (inset in Figures c and d). The peak in the line profile is much higher in the case of transmission imaging.

electron beam (2-10keV) similar to methods using a solid-state detector [12], [13] or a SE-based transmission detector [14]. In our method, we place the tissue section directly on top of a thin scintillator screen (thinner than 200 μm), which is coated with a conductive layer. A high NA objective lens collects the light signal generated by the electrons transmitted through the sample, and the light is imaged onto a photon detector outside of the vacuum chamber. Alternatively, the detector could be placed in a vacuum directly underneath the scintillator. An overview of the detection method is shown in figure 2.2. This method was first developed by A. Boyde [15], who placed a thick section on top of a glass substrate and collected the cathodoluminescence created by the transmitted electrons. By

using a scintillator instead of glass, the light output and, thus, the DQE is greatly increased, and the use of an ultrathin section gives a higher image resolution than a thick section. Compared to other detection methods, the collection efficiency of the detection is very high and is only limited by the backscatter coefficient of the scintillator. It has been shown that this imaging method can be used to image heavy metal stained and embedded biological tissue sections[11]. Results of tissue imaging are shown in figure 2.1, where the transmission imaging is compared to backscatter imaging. The sample is a 70nm thick section of rat pancreas, prepared according to the OTO protocol and embedded in EPON. Figures 2.1a and 2.1b show, at first glance, a large similarity in both contrast and signal-to-noise ratio (SNR) for both imaging modalities.Figures 2.1c and 2.1d show that in some cases, the transmission imaging can give contrast in locations where there is hardly any in backscatter imaging (highlighted by the arrow). In previously published work, we have already drawn some conclusions about the image quality using a semi-analytical method [16]. This paper is dedicated to analyzing the quality of the detection method and determining the optimum imaging conditions. This is done with a more rigorous Monte Carlo simulation method to aid some oversimplifications from the previous work. The outcome is then compared to backscatter detection.

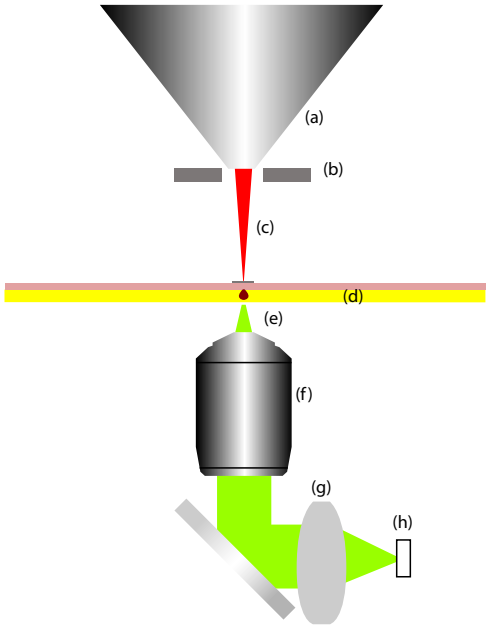


Figure 2.2: An overview of the detection method as described. (a) The SEM pole-piece, (b) backscatter detector, (c) electron beam, (d) ultrathin tissue section on a conductive coating on a scintillator, (e) scintillation light, (f) high NA light microscope objective, (g) light imaging system (can consist of multiple lenses and windows),(h) photon detector.

## 2.2. MODEL

### 2.2.1. PERFORMANCE PARAMETERS

In order to evaluate the optical transmission detection system and to compare it to backscatter imaging, two parameters are considered. These parameters are the Contrast-To-Noise Ratio (CNR) and SNR. The most well-known parameter of these two is SNR. In this article, the SNR that is referred to is the detected SNR at the end of the detection chain ($SNR_{out}$). The CNR and SNR are given by equation (2.2).

$$CNR = \frac{\mu_{1out} - \mu_{2out}}{\sqrt{\sigma_{1out}^2 + \sigma_{2out}^2}} \tag{2.1}$$

$$SNR_1 = \frac{\mu_{1out}}{\sigma_{1out}} \qquad SNR_2 = \frac{\mu_{2out}}{\sigma_{2out}} \tag{2.2}$$

The CNR gives a quantification of how well two features are contrasted against the noise on those features. $\mu_1$ and $\mu_2$ are the expectation values of the signal of the two features; in our case, the amount of detected transmitted or backscat-

tered electrons and $\sigma_1$ and $\sigma_2$ are the standard deviations of these signals. An example in a simulated image of the effect of SNR and CNR is shown in figure 2.3. The image shows two lines with a lower transmission coefficient than the background. The CNR is calculated between the background and the lines. The SNR is the average SNR over the whole image. The images were stretched to full dynamic range, which means maximum digital contrast without clipping. It shows that just a high SNR or CNR will not give a good image. When we consider a low SNR and CNR, the lines are hardly visible. Low SNR but high CNR has very clearly defined lines. But even if the CNR is low and the SNR is high, still the lines are visible. The best-looking image is, however, one in which both the SNR and CNR are high[17].

To calculate the SNR and CNR in a final image, the whole detection system has to be taken into account. For this analysis, a cascading noise model is used as developed by Timischl, Date, and Nemoto [18][17]. The cascade of noise here is as follows. In the imaging system, five conversion steps add noise to the eventual signal (see figure figure 2.4). The first of which is the shot noise on the primary electron beam, which follows Poisson statistics. The second is the generation of the transmission or backscattered electrons in the sample, which follows binomial statistics. The third stage is scintillation, which follows Poisson statistics. The last two stages are the collection of the light by the objective lens and the detection, which follow binomial statistics. The detector, with typically a total gain of $10^6$, was omitted as it adds no noise by itself. Readout noise and detector dark noise are left out of the calculation, as both are considered to be avoidable. The scintillation is, in this work, omitted for backscatter imaging, as various detector setups are possible [19], and the calculation is done for a best-case scenario. The signal and the noise, $\mu_{1out}, \mu_{2out}, \sigma_{1out}, \sigma_{2out}$ from equation (2.2) are calculated as shown in equations (2.3) and (2.4).

$$\mu_{1out} = \mu_{1b}\mu_{1t}\mu_{1s}\mu_c\mu_d \tag{2.3a}$$

$$\mu_{2out} = \mu_{2b}\mu_{2t}\mu_{2s}\mu_c\mu_d \tag{2.3b}$$

$$\sigma_{1out} = \mu_{1out} \times \Big(\frac{\sigma_{1b}^2}{\mu_{1b}^2} + \frac{\sigma_{1t}^2}{\mu_{1b}\mu_{1t}^2} + \frac{\sigma_{1s}^2}{\mu_{1b}\mu_{1t}\mu_{1s}^2} + \frac{\sigma_c^2}{\mu_{1b}\mu_{1t}\mu_{1s}\mu_c^2} + \frac{\sigma_d^2}{\mu_{1b}\mu_{1t}\mu_{1s}\mu_c\mu_d^2}\Big)^{\frac{1}{2}} \tag{2.4a}$$

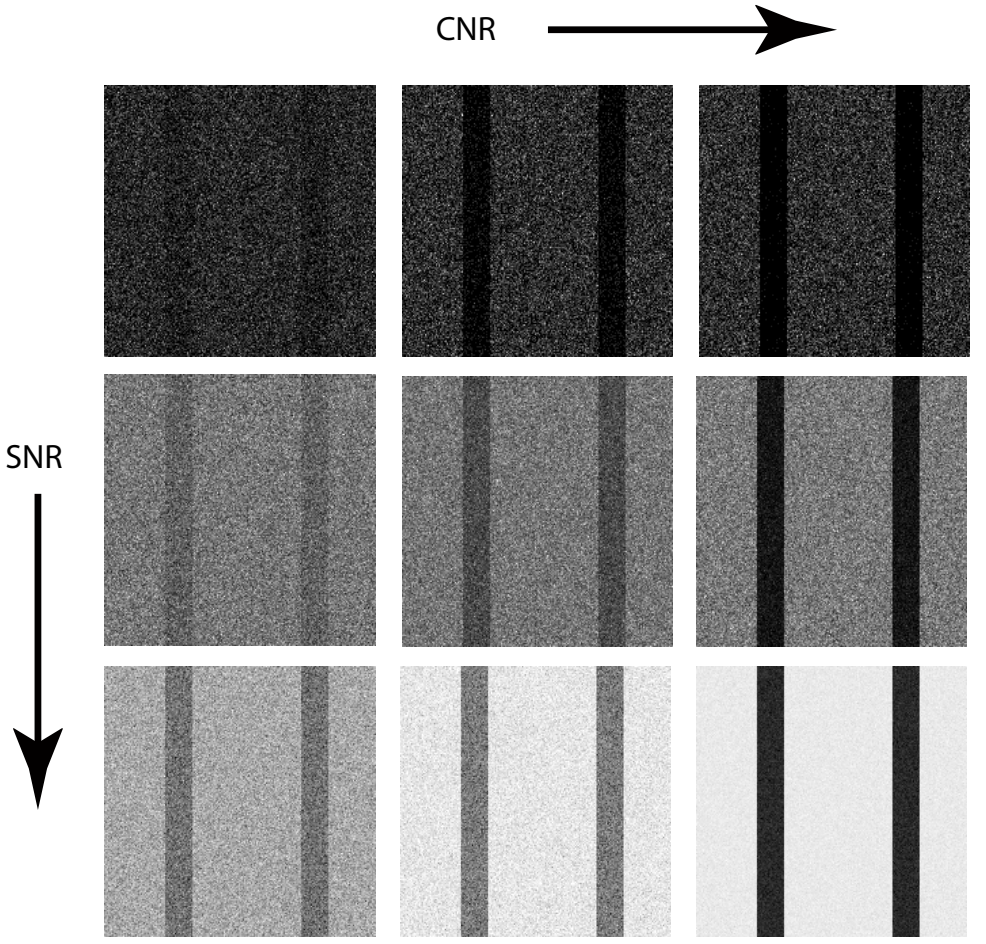


Figure 2.3: From left to right showing the effect of increasing CNR and/or SNR. The image was simulated for transmission imaging with binomial noise. It shows that if there is a high SNR and a high CNR, image quality can be considered best.

$$\sigma_{2out} = \mu_{2out} \times \left(\frac{\sigma_{2b}^2}{\mu_{2b}^2} + \frac{\sigma_{2t}^2}{\mu_{2b}\mu_{2t}^2} + \frac{\sigma_{2s}^2}{\mu_{2b}\mu_{2t}\mu_{2s}^2} + \frac{\sigma_c^2}{\mu_{2b}\mu_{2t}\mu_{2s}\mu_c^2} + \frac{\sigma_d^2}{\mu_{2b}\mu_{2t}\mu_{2s}\mu_c\mu_d^2}\right)^{\frac{1}{2}} \tag{2.4b}$$

Where $\mu_b, \mu_t, \mu_s, \mu_c$ and $\sigma_d$ are the expectation value and $\sigma_b, \sigma_t, \sigma_s, \sigma_c$ and $\sigma_d$ are the standard deviation of the beam, transmitted electrons (or backscattered), scintillation, light collection and the detector efficiency, respectively. Note that due to the scintillator term, which contains the deposited energy, the CNR is in-

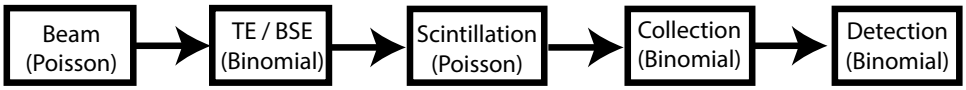


Figure 2.4: The cascading noise model used for the SNR and CNR calculations.



fluenced by the energy loss in the sample. The number in the subscript is the area for which the number holds. For example, in this article, 1 would be resin, and 2 would be a cell membrane. As shown by Timischl [17], the CNR is independent of contrast and brightness settings, whereas the SNR is not.

### 2.2.2. MONTE CARLO MODEL SETUP

Monte Carlo simulations were performed using the Casino simulation software[20]. The model used for this work is based on the imaging of osmium-fixed (stained) tissue embedded in an epoxy resin. In electron microscopy of tissue samples, most commonly, Osmium-Tetroxide is used as a post-fixative after aldehyde fixation. Osmium tetroxide reacts and binds with the unsaturated lipids present in the tissue material, for instance, cell membranes[21]. Furthermore, Osmium is a high atomic number, dense metal, which gives high contrast in all detection methods used in electron microscopy and is thus often seen as a stain as much as a fixative. It must be noted that except for fixation and staining, the osmium present in the tissue also provides a conductive path for the electrons to the substrate, preventing charging. The amount of osmium at any place in the tissue is highly dependent on the composition of the tissue before fixation, and numbers in the literature vary greatly (from 2wt% to 15wt% [22]–[25]). For this model, we will assume that the Osmium completely generates the contrast generated in the biological material, and the comparatively light and low-density native elements give no contrast. The sample provided is built up as follows: An ultra-thin tissue section (50-100 nm), a Boron coating (10nm-130nm), and a YAG:CE substrate. The two different areas of the sample are bare epon, the embedding medium, and an osmium-fixated cell membrane with either 1wt% , 5wt% , or 10wt% of Osmium. The full compositions are listed in table 2.1. In the simulations, the electron beam impinges on one of the materials for energy varied between 1keV and 10 keV. From the Monte Carlo simulation, three parameters are obtained for each energy. Those parameters are the backscatter coefficient, the amount of electrons absorbed in the scintillator, and the average energy these electrons deposit. These numbers are then used to fill in equation (2.2) for a certain current and dwell time.

An example of the full transmission detection chain will now be given. The tissue section has a thickness of 70 nm, 5% staining (see table 2.1) on the membrane, and the scintillator has a 70 nm B coating. The landing energy is chosen to

| Material | Density (g/cm$^3$) | H | C | O | Os |
|---|---|---|---|---|---|
| Epon | 1.22 | 0.080 | 0.63 | 0.29 | 0 |
| Membrane 5% stain | 2.29 | 0.080 | 0.63 | 0.24 | 0.05 |
| Membrane 1% stain | 1.43 | 0.080 | 0.63 | 0.28 | 0.01 |
| Membrane 10% stain | 3.35 | 0.080 | 0.63 | 0.19 | 0.1 |
| | | Y | Al | O | |
| YAG | 4.56 | 0.45 | 0.23 | 0.32 | |

Table 2.1: Table showing the compositions of the materials used in the Monte Carlo simulations, compositions are given in wt %

be 5keV at a current of 1nA and a dwell time of 1 µs. This current and dwell time gives, on average, 6241 electrons($\mu_b$) with a standard deviation of 79 ($\sigma_b$) electrons. The average transmission coefficients are calculated using Monte-Carlo simulations. These are, for the membrane: 0.73 and for the bare resin: 0.90 ($\mu_t$). The standard deviations of the transmitted electrons are 0.44 and 0.3 ($\sigma_t$), respectively, according to the binomial distribution ($\sqrt{\mu_t(1-\mu_t)}$). The average energy deposition of the electrons in the scintillator is also taken from the simulations. The electrons are now converted to light with an estimated efficiency of 20 photons per keV per electron [26], giving an average of 59 photons per electron for the membrane and 73 for the bare resin ($\mu_s$). These have standard deviations of $\sqrt{73}$ and $\sqrt{59}$, respectively, according to the Poisson distribution. The next two terms in the chain are no longer material dependent. The collection efficiency of the imaging system can be considered fairly low due to the limited numerical aperture of the objective lens (0.95) and the reflection losses of the rest of the imaging system. The collection efficiency of the photons in our system is calculated by assuming a homogeneous light source in the YAG:CE. An optical air objective with an NA of 0.95 will now collect approximately 18% of the light, and the other lenses and mirrors lower $\mu_c$ to 0.05 with a standard deviation of 0.21($\sigma_c$). The detector has a limited fill factor and quantum efficiency at the wavelength of the scintillation light. From the supplier datasheet, we find that $\mu_d$ is approximately 0.4 with a standard deviation of 0.49 ( $\sigma_d$). Filling these numbers into equation (2.2) gives a value of 7.4 for the CNR and a value of 49 and 57 for the SNR on the membrane and resin, respectively. Backscatter detection is calculated in the same fashion for the steps that are still valid: electron beam, backscatter generation, and collection efficiency (assumed to be 0.5). The average SNR for backscatter imaging in this case is 12, and a CNR of 2. All these calculations give a single point in, for instance, figure 2.5b.

## 2.3. MONTE CARLO SIMULATION OF THE MODEL SAMPLE



A result of the model is shown in figure 2.5a. It shows the dependence of both CNR and SNR on the landing energy for a 100nm section and a 70nm boron coating layer on top of the scintillator. First, we only consider the 5% staining case. The simulation was run from 1keV to 10keV, but the graph starts at 3.5keV as below that energy, no electrons pass through the membrane anymore. Imaging here can still be performed, but the contrast mechanism will be severely compromised, and a CNR or SNR can no longer be calculated. Because of the difference in transmission coefficient between the membrane and the surrounding resin, the SNR values are slightly different for the two areas. In this graph, the average of the two was taken, as in this model, it is assumed that all other values lie in between the two extremes defined by the membrane and the resin. As the energy increases, more electrons pass through the tissue and create more photons in the scintillator, causing the SNR to rise with energy. At higher energy, this is due to the generation of extra photons by each electron. On the other hand, the CNR drops with increasing energy until it almost reaches zero. This drop is caused by the difference in transmission coefficient between the membrane and the resin becoming smaller at higher energies. As the SNR and the CNR have opposite trends as a function of energy, an optimum energy will exist where both are high. There are different ways to define this optimum; in this article, it will be assumed that the optimum lies where the product of SNR and CNR is maximized. At this maximum, the combination of the two has the highest possible value. For the case shown here, this optimum lies at 4keV (figure 2.5b). The next question that arises from this result is, how does this optimum and the levels of both SNR and CNR change with various levels of staining, coating thickness, scintillator yield, and collection efficiency of the optical system?

#### LEVEL OF STAINING AND SECTION THICKNESS

Depending on the application and specific tissue, the amount of staining can vary greatly. In order to investigate the effect of the level of staining, the content of osmium in the membrane is changed to 1wt% for low staining and 10 wt% for high staining. The effect of the staining level in the transmission imaging is shown in figures 2.5a and 2.5b. The staining level changes both the SNR and CNR levels but clearly has the biggest effect on the CNR. The difference between the staining levels will severely affect the current and dwell time needed to get a good image. The optimum landing energy shifts to a higher energy as the amount of staining increases, from 3.5keV to 4.5keV. Here is where one should watch out, as when the wrong energy is chosen, the effect of extra staining can be undone. In general, the conclusion can be made that extra staining is always beneficial from a pure imaging perspective, as it will enhance the contrast without deteriorating

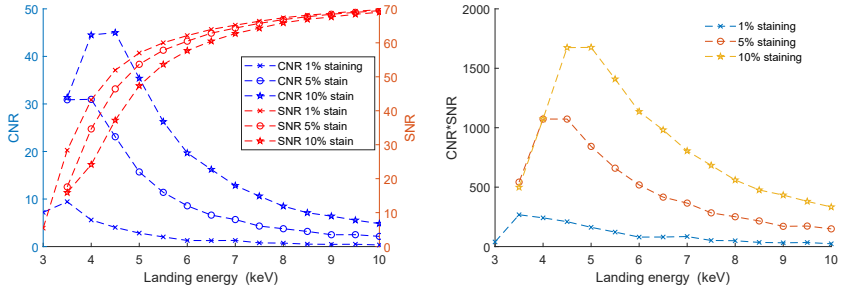


(a) (b)

Figure 2.5: Graphs showing the results of Monte Carlo Simulation, the effect of the level of staining on (a) the SNR and CNR and (b) the product of SNR and CNR. Staining improves the CNR significantly without reducing SNR.

the SNR greatly. There is no maximum to the amount of staining from an imaging perspective as long as electrons can pass even the most densely stained areas of the sample.

Decreasing the section thickness from 100nm to 50nm has a similar effect as the change in staining level (figure omitted). This can be explained by the fact that the transmission of electrons through a material is mostly dependent on mass-thickness, the product of membrane thickness, and its density [27]. This means changing the thickness and composition has a similar effect—the optimum imaging energy changes from 4 to 3.5keV, with the change in thickness as described. Increasing the section thickness will, however, result in a bad blurred membrane edge, as the membranes do not go straight down through the section but will, in general, always be at an angle.

### SCINTILLATOR COATING THICKNESS AND MATERIAL

Because the scintillator is non-conductive, a conductive coating has to be applied to its surface to avoid charging. The coating material and thickness chosen for the previous analysis was 70nm of Boron. Boron was chosen because of its low atomic number and density, causing a low absorption and backscatter coefficient. The thickness of 70nm was experimentally found to be the optimum as it allows for the electron beam to spread out significantly before hitting the scintillator. This ensures that the image is not contaminated with small-scale imperfections in the scintillator or its surface. For reasons with the same considerations, it might be that a different coating thickness or material is preferred. First, we analyze the effect of a different thickness of boron. The results of the calculation are shown in figure 2.6a, for a 5% stained section of 100nm thickness.

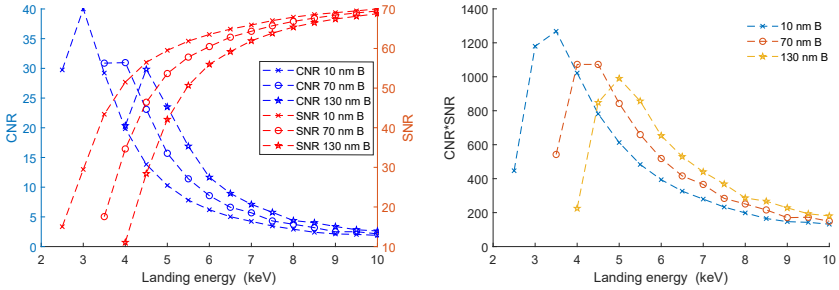


(a) (b)

Figure 2.6: Graphs showing the results of Monte Carlo Simulations, the effect of scintillator coating (Boron) thickness on (a) the SNR and CNR and (b) the product of SNR and CNR. The coating thickness shifts the optimal landing energy for imaging. The CNR is not affected, where the SNR is slightly reduced.

As is to be expected, all the trends in SNR and CNR observed before are the same and independent of coating thickness. An interesting observation is that the variation in coating thickness does not so much change the levels of SNR and CNR but shifts them in energy. This is due to the coating layer acting as an amplifier for the difference in transmission coefficient between the two regions. This effect can also be seen in figure 2.6b, which shows a shift in the optimum energy for imaging.

A change of the material was also investigated, and the result is shown in figure 2.7b. For the change of material, the mass density was kept constant to that of 70nm of B. This translates to a 54 nm Al layer and a 16 nm Mo layer. From the graph, it is clear that the imaging performance is dependent on the mass thickness of the coating and not so much on the material. There is, however, a chance that imperfections influence the imaging in the coating layer, as the electron beam has less distance to be able to spread out before hitting the scintillator surface. If B is not available, any other (conductive) metal can be used as long as the mass thickness is the same.

### DETECTION PARAMETERS

Other efforts in signal detection are the efficiency of the scintillator, the collection efficiency of the objective lens, and the detection efficiency of the detector. The collection efficiency of the objective lens can be increased by increasing the NA. Previous calculations were based on an air objective with an NA of 0.95. It has been shown that a higher NA immersion objective of up to 1.4 can be used in vacuum [28], [29], which gives a method to increase the collection efficiency. The effect of increased collection efficiency is shown in figure 2.8. Clearly, an

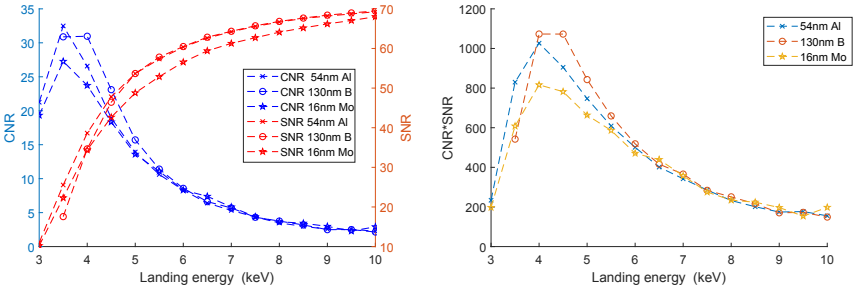


(a) (b)

Figure 2.7: Graphs showing the results of Monte Carlo Simulations, the effect of the coating material, with a fixed mass-thickness, on (a) the SNR and CNR and (b) the product of SNR and CNR. The material that the coating is made of does not affect the imaging as long as the mass-thickness of the coating is the same.

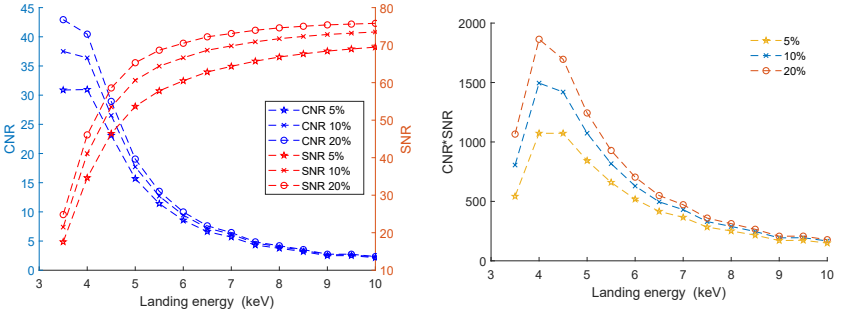


(a) (b)

Figure 2.8: Graphs showing the results of Monte Carlo Simulations, the effect of light objective collection efficiency on (a) the SNR and CNR and (b) the product of SNR and CNR. Increasing the light collection efficiency increases the SNR and SNR slightly.

increase in collection efficiency would be beneficial for the detection system. A doubling of the collection efficiency causes both the SNR and the CNR to rise. The maximum product of these two parameters increases by a factor of 1.5 when the collection efficiency is increased from 5% to 10%. Increasing the scintillator yield from 20 to 40 photons per keV per electron has the same effect as increasing the collection efficiency from 5 % to 20%(graph not shown).

### COMPARISON TO BACKSCATTER IMAGING

The most used imaging modality in SEM imaging of tissue is making use of the backscattered electrons. As the tissue section is flat and has hardly any topogra-

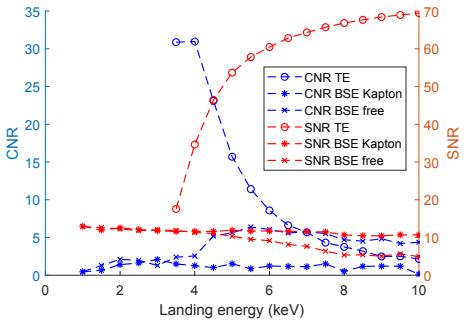


Figure 2.9: Comparison between the CNR and SNR in transmission imaging(circles) and backscatter imaging(crosses). Both the CNR and SNR of transmission imaging are much higher in transmission imaging than backscatter imaging.

phy, secondary electron imaging is generally less optimal. Backscatter imaging does not show the sample topography but the amount of staining in each position in the section. Areas with a higher density or atomic weight will show a higher backscatter signal, making, for instance, stained membranes visible. A free-standing section and a section on a Kapton substrate were simulated for the calculations. For the calculation, a Kapton substrate and a free-standing section were simulated. Kapton was chosen because it is widely used in the atumtome serial sectioning system[30]. The free-standing section is representative of a section on a TEM grid.

The results of simulations for a 5% stained membrane are shown in figure 2.9. As can be expected from expressions relating the backscatter coefficient to the landing energy [31], the backscatter coefficient for the free-standing tissue increases with lower energy, increasing the SNR. For the tissue on kapton, the SNR is fairly constant due to the background of the substrate on the backscatter electrons. This background, however, does not contain any information, and the contrast does not change. The CNR gets slightly higher at higher energies but does not change as much with energy as it does for transmission imaging. If backscatter imaging is compared to the transmission imaging, it stands out that both the CNR and SNR are lower for the 5% stain (figure 2.9. The graph of the product of SNR and CNR was omitted in this comparison as the product in the case of backscatter imaging is too low to be reasonably compared to the transmission imaging case.

#### COMPARISON TO SECONDARY ELECTRON IMAGING.

In many studies, secondary electron (SE) detection is used for imaging of heavy metal stained and resin embedded tissue sections [8], [32]–[34]. Especially in

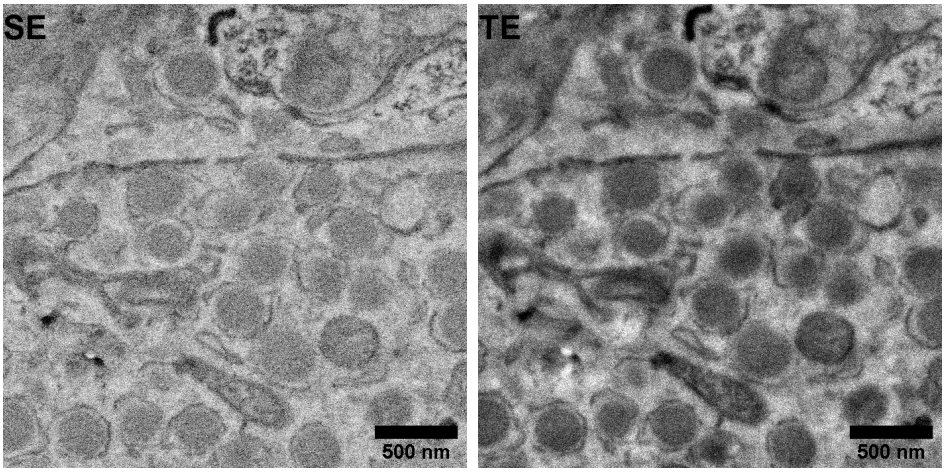


(a) (b)

Figure 2.10: OTO stained 70nm section of rat pancreas imaged at (a)2.5keV landing energy with SE detection and at (b) 3keV landing energy with TE detection. Imaging was performed with a 400pA beam current, and 800ns dwell time. Both image histograms have been stretched to full dynamic range. The TE image clearly shows more contrast and less noise than the SE image.

MBSEM microscopes, SEs can be detected due to their relatively small energy spread. This spread allows for the focusing of the SE electron beams onto a detector[35], [36]. The main disadvantage of this method of detection is that, in general, SEs are mostly generated by topographical features, of which there are none or few in the flat tissue sections. Therefore, it is thought that the image formation contrast in the case of flat tissue samples is a result of so-called SE2 electrons, that is, secondary electrons that are generated by backscattered electrons. This being an indirect process, extra noise is added in the SE generation step. Due to this, the images have less contrast and a lower signal-to-noise than TE and BSE imaging. A comparison is shown in section 2.3. The image shown is that of OTO-stained rat pancreas tissue embedded in EPON, with a 70nm section thickness. The SE image was taken at 2.5keV and the transmission image at 3keV, both with a 400pA beam current and an 800ns dwell time. The detector used for SE detection was an in-lens scintillation detector. The section showed charging effects at lower landing energies than 2.5keV. The TE image shows more contrast and a better SNR than the SE image. Note that the SNR of the SE image is dependent on the detector layout and electronics.

### 2.3.1. ANALYTICAL MODEL

Instead of a Monte Carlo model, an analytical model can also be created. This has as its main benefit that calculation time is much less, but will be less precise than the Monte-Carlo model. For simplicity, we assume that no electrons are absorbed by the sample, which is a decent approximation in a low Z material, as shown by Grillon [37]. So, in order to calculate the number of transmitted electrons, we calculate the electrons that are not back-scattered. To calculate the backscatter coefficient of a thin layer, equation (2.5) is used[31].



$$\eta = \frac{N_A \rho t}{A} \int_{\pi/2}^{\pi} \frac{d\sigma}{d\Omega}(\theta, E) 2\pi \sin\theta d\theta \tag{2.5}$$

Where $N_A$ is Avogadro's number, $\rho$ is the density, t is the layer thickness, A is the atomic mass, and $\frac{d\sigma}{d\Omega}$ the differential cross section for backscattering of electrons on solid targets. For these calculations, the densities of a solid were used, and the average density was calculated using weight fractions. The differential cross sections for a certain material and energy are obtained from ELSEPA [38] in steps of 1 degree. Because the simulated tissue is a multi-element mixture, we use equation (2.6) to calculate the total backscatter coefficient.

$$\eta = \sum_i C_i \eta_i \tag{2.6}$$

Where $C_i$ are the concentrations of the respective elements. At some point, the material does not behave like a thin film anymore but as a bulk material. For a bulk material, the backscatter coefficient is calculated through parametrizations carried out by Hannachi, Rouabah, Champion, *et al.* [39], which is the maximum possible backscatter coefficient. For a smooth transition between the thin film and the bulk values, equation (2.7) was used.

$$\frac{1}{\eta}^4 = \frac{1}{\eta_{thin}}^4 + \frac{1}{\eta_{bulk}}^4 \tag{2.7}$$

Where $\eta_{thin}$ and $\eta_{bulk}$ are the backscatter coefficients of a film of a certain thickness and a bulk sample, respectively. This is only chosen to have a smooth but fairly rapid transition, and the power in this formula is arbitrary.

This layer (section) is placed upon a layer of Boron, used as a conductive coating layer of the scintillator underneath. Both the backscatter coefficients of the EPON-osmium layer and the Boron layer are calculated as described before. The backscatter coefficient of the YAG:CE scintillator was simulated using Casino 2.5.1 [20] and was found to be 0.20 for landing energies between 1kev and 7kev.

The number of transmitted electrons is now given by:

$$N_{transmitted} = N_{beam} \times (1 - \big((1 - \eta_{tissue}) \times (1 - \eta_{coating}) \times (1 - \eta_{scintillator})\big)) \tag{2.8}$$



Where $N_{transmitted}$ and $N_{beam}$ are the number of electrons in transmitted and in the beam, respectively. $\eta_{tissue}$, $\eta_{coating}$ and $\eta_{scintillator}$ are the backscatter coefficients of the EPON-osmium film, the Boron coating, and the scintillator.

The light output of the scintillator is energy-dependent, which means that the energy loss in the tissue gives extra contrast in the eventual image. When electrons lose more energy in the section, less energy is left to create light in the scintillator. In regions with a higher average atomic number, more electrons are backscattered (thus less transmitted), and more energy is lost. For this model, we use a continuous energy loss in a trajectory perpendicular to the surface. equation (2.9a) is Bethe's energy loss function with the low energy adjustments of Joy and Luo [40], which then gives the energy loss through a certain film thickness.

$$S = \frac{dE_m}{dx} = 7.8 \times 10^{10} \frac{1}{E} \sum_i C_i \frac{Z_i \rho_i}{A_i} \ln\left(\frac{1.1666E}{J_i'}\right) \tag{2.9a}$$

$$J_i' = \frac{J_i}{1 + k\frac{J_i}{E}} \tag{2.9b}$$

$$J_i = 11.5Z_i \text{ for } Z_i \leq 12 \tag{2.9c}$$

$$J_i = 9.76Z_i + \frac{58.5}{Z^{0.19}} \text{ for } Z_i \geq 13$$

Where E is the energy of the electrons, $C_i$ is the concentration of the element with the atomic number $Z_i$, density $\rho_i$, atomic weight $A_i$, and $J_i$ is the ionization potential. When the energy loss is such that the electron energy drops below 50eV, the transmission coefficient at that location is considered to be zero.

#### RESULTS

The result for a membrane with 5% (table 2.1) stain is shown in figure 2.11. It can be seen that with increasing energy, the SNR increases as the amount of photons generated in the scintillator increases. The CNR has an opposite trend and increases as the energy is lowered. Below a certain energy, both the SNR and CNR are no longer calculated as the average electron energy has dropped below a threshold value for which no transmission can be expected. From this graph, it is fairly obvious that the lack of absorption of electrons in the tissue section causes a problem. One would not expect the SNR to stay so high at lower energies. When looking at this graph, the conclusion would be to use the lowest possible landing energy, as the CNR only goes up and the SNR hardly drops. In reality, however,

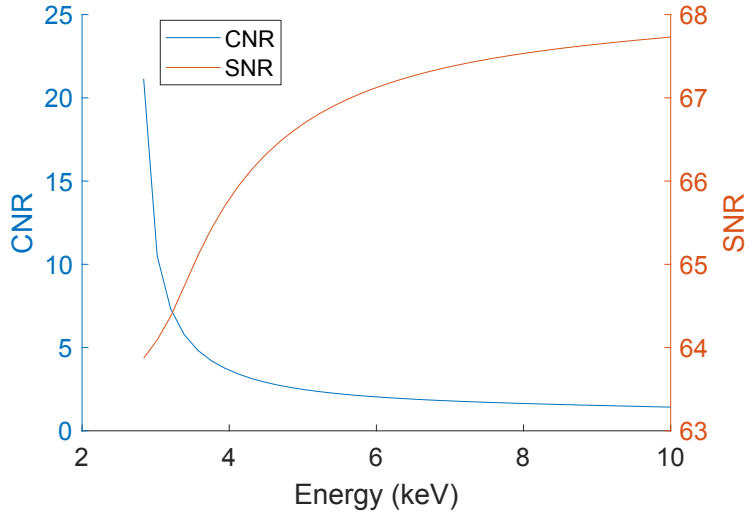


Figure 2.11: SNR and CNR as a function of landing energy for a membrane with 5% staining, as calculated through a semi-analytical model.

the SNR will drop significantly at low energies as the tissue section absorbs more electrons. This absorption happens due to electrons scattering over large angles, which increases their path length through the section, increasing the energy loss.

## 2.4. EXPERIMENTAL SETUP FOR MODEL VERIFICATION

The Monte-Carlo model, as described in the previous section, cannot be easily verified with fixated tissue sections. In a tissue section, the exact composition at two different points is not known, and the sample is extremely heterogeneous, so no two locations will have the same composition. Therefore, another sample was manufactured: a YAG:CE scintillator substrate was half coated with 50nm Al and half with 50nm Cr. For these measurements, a FEI Verios SEM was used, equipped with a Delmic SECOM integrated optical set-up[28], [29]. SECOM is an integrated inverted fluorescent microscope used for correlative light and electron microscopy. In this SECOM platform, the excitation path was removed, and the system was only used for collecting the light generated in the scintillator. This light is collected using a 0.95 NA air objective, positioned directly underneath the scintillator, and focused on a Hamamatsu multi-pixel photon counter. During the experiments, the current was constant at 800pA, and the dwell time was 5$\mu$s. The electron beam was defocused to a spot size larger than 25 µm to blur out all small-scale defects that might be present in the Al or Cr layer. The low dwell time

of 5$\mu$s was chosen in order to avoid possible bandwidth limitations in the detection path of the backscatter detector. Due to the inhomogeneous light output of the scintillator, which is location-dependent on scales larger than a few micrometers, the measurements were performed at random spots on the sample. To find the true SNR and to compensate for an offset (brightness) in the images, the measurements were done at 0.4nA and 0.8nA beam current and adjusted accordingly. At this current and dwell time, the amount of photons arriving at the detector within that dwell time is not lower than 2000. The dark count of the detector at that same time is 2, which can thus be neglected.

To check the model with actual tissue imaging, tissue from a rat pancreas was used. The tissue was prepared according to the OTO protocol [41] and cut to a 100nm section. The tissue was placed on top of a TEM grid, which was then stuck to a Boron-coated CRY18 scintillator with carbon tape. Because of the small space between the TEM grid and the scintillator, the beam can spread out after leaving the tissue, making sure that the image is not obscured by an inhomogeneous coating or scintillator defects. As mentioned before, it is hard to verify CNR results on tissue, but methods are available for estimating SNR in an SEM image. This method is described by Joy [42]. It relies on the fact that if the pixel size in the image is taken small enough (much smaller than the size of the beam), two subsequent lines in the image are very similar. From those, SNR can be calculated by using the formula in equation (2.10), where X and Y are two successive lines in the image. This can now be done for all the lines in an image, giving an SNR. The pixel size was chosen to be 0.5nm, which is significantly smaller than the estimated probe size of about 4nm full-width half maximum. For every landing energy, three different images were taken, and for those, the SNR was calculated. Taking images of the same areas twice is not possible as imaging changes the sample, the transmission yield changes slightly, and the sample tends to deform.

$$SNR = \frac{R_n}{1 - R_n} \text{ where } R_n = \frac{\text{cov}(X, Y)}{\sqrt{\text{var}(Y)\text{var}(Y)}} \tag{2.10}$$

## 2.5. EXPERIMENTAL RESULTS

A representation of the experimental results is shown in figure 2.12. It shows the two regions, Al and Cr, in both backscatter and transmission. The image is scaled to full range, and it shows that in TE imaging, the contrast is higher than in BSE. Because Cr is a heavier metal than Al, we expect it to have a lower transmission coefficient and a higher backscatter coefficient than Al, which we can immediately see in the image. In TE, the noise is hardly visible due to the high contrast-to-noise ratio. This image clearly illustrates the better sensitivity to material changes compared to backscatter imaging.

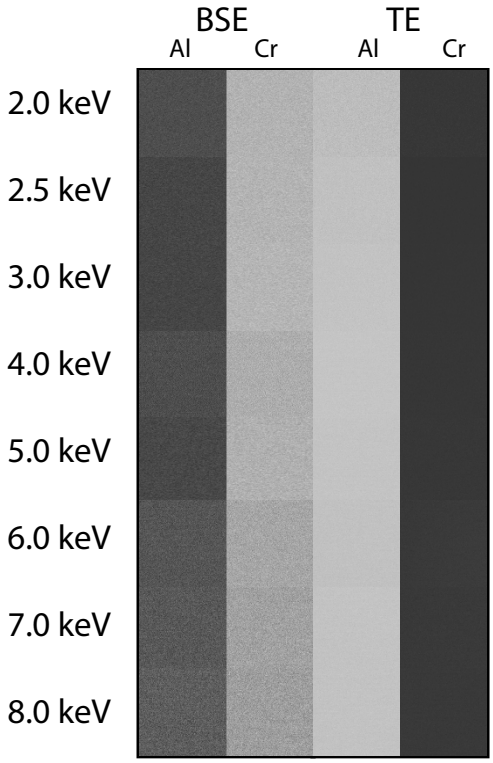


Figure 2.12: Representation of experimental results to measure the CNR and SNR. The sample is a scintillator half-coated with 50nm Al and 50nm Cr. The example shown here are cutouts of the images used to find the CNR and SNR.

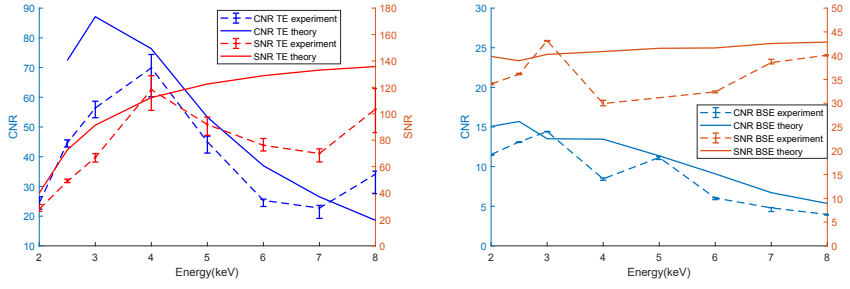


(a) (b)

Figure 2.13: Results of the SNR and CNR measurements on a sample with 50nm Cr and 50nm AL for (a) transmission imaging and (b) backscatter imaging. The same trend and levels are observed in the model and the experiment.

When analyzing the images, we find the results shown in figure 2.13a. Note that the average SNR is shown, as the SNR for the Cr and Al regions are different. First, inspecting the measured CNR and SNR for TE imaging shows that the expected trend is found. As the energy goes down, the CNR becomes larger, but at the same time, fewer electrons reach the scintillator, causing a drop in the SNR. At higher energy, the opposite happens: the SNR rises, and the CNR drops. Because of a lot of unknown factors in the measurement, namely objective lens collection efficiency, scintillator efficiency, small errors in the Monte Carlo simulation, and precise thickness of the Cr and Al films, the absolute values were not compared with the calculation results. The trends are, however, as expected. The product of SNR and CNR for the TE imaging is shown in figure 2.14. The peak lies at the same position in the experiments as it does in calculations. As we have seen, collection efficiency and scintillator yield do not change the best energy for best imaging.

When comparing the imaging to that of backscatter imaging, we have to keep in mind that the scintillator substrate will influence the actual signal. The extra backscattered electrons from the scintillator will give an extra noise floor to the signal. The collection efficiency of the backscatter detector is unknown, especially as this will be an energy-dependent efficiency. Furthermore, we have not developed a full noise model of this detector. From figure 2.12, we can, however, see that the CNR in BSE imaging is much lower than for TE imaging. When looking at figure 2.13b, it is clear that the levels for both CNR and SNR are much lower than in the TE imaging case.

The result from SNR measurements on tissue images is shown in figure 2.15. It can be seen here that the SNR increases with energy. After 7.5keV, the calculation with equation (2.10) fails, as there is not enough detail in the image due to loss of contrast. Even though this method does not calculate the product of SNR and CNR, it is a convenient and quick way to find the optimum imaging energy, which is at the point where the SNR stops rising. Figure 2.16 shows tissue images for three different landing energies compared to both TE and BSE imaging. At first glance, the contrast and SNR look better in the TE images than they do in the BSE images; this is, however, quite heavily dependent on detector specifications. In the BSE case, it is clear that the image quality goes up with lower energy, as the 3keV image seems to be the best. In TE imaging, the difference is subtle, but on close inspection, it can be seen that the image is the best at 5keV. This is the same landing energy as was found from figure 2.15. The drop in CNR at higher energies is not very quick due to the fairly high staining in this tissue section.

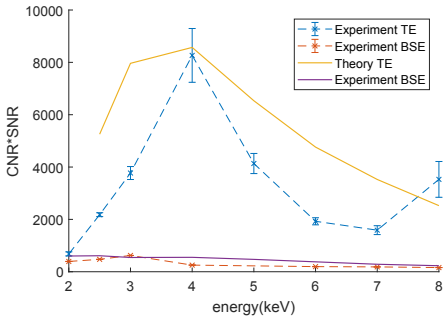


Figure 2.14: The product of SNR and CNR for a 50nm Al and 50nm Cr layer as a function of landing energy. The same trend and levels are observed in the model and the experiment. The peak lies in the same location.

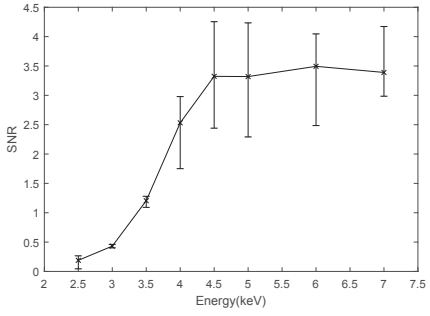


Figure 2.15: Graph showing the measured (average)SNR as a function of landing energy for rat pancreas tissue. Measurements were done with the same current and dwell time. It shows the decreasing SNR at low landing energy.

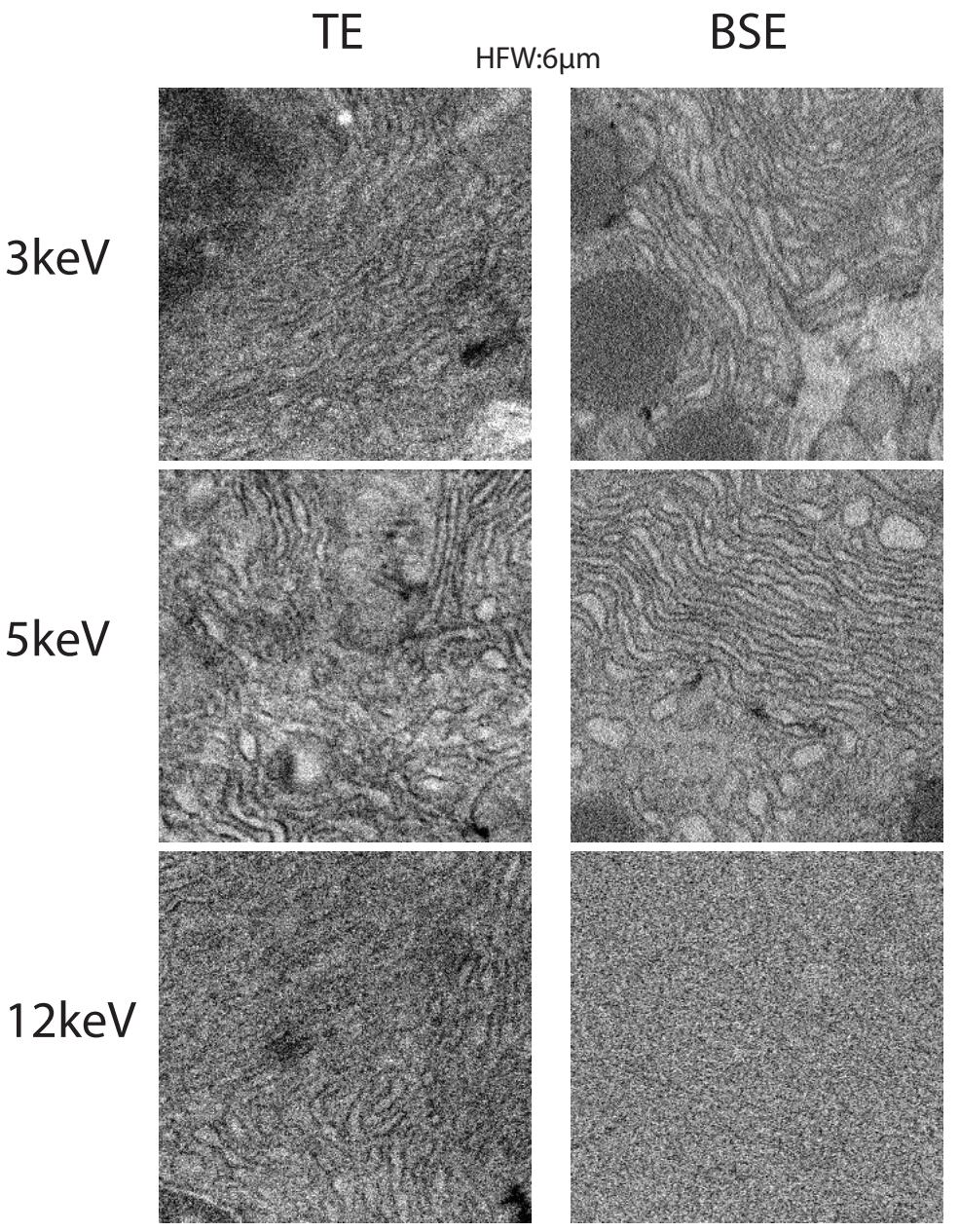


Figure 2.16: Comparison of TE imaging and BSE imaging (inverted contrast) for landing energies of 3keV, 5keV, and 12keV. The horizontal field width(HFW) is 6µm, a dwell time of 5µs, and a beam current of 50pA.

## 2.6. RESOLUTION LOSS



This section will discuss the resolution loss that can be expected with transmission imaging. The cause of this loss of resolution is as follows. As the beam goes from an area with one density to an area with another density, the transmission coefficient changes gradually instead of instantaneously when part of the beam hits the different density area. As the beam moves closer to a higher-density area, more electrons that scatter in the material get caught by the higher-density material and lose more energy there, are absorbed, or are backscattered. This is especially the case for low-energy electrons in transmission mode, as many scattering events occur before the electron is detected. To investigate this effect closely, Monte Carlo simulations were performed. The simulations were performed using Casino 3.2.0.4[43]. A sample was designed where there is a sharp transition between bare EPON and an EPON with a 5wt% Osmium stain. The beam was scanned from the unstained part to the stained part, and the transmission and backscattered electrons were counted. This was performed for a section thickness of 50nm and 100nm, a landing energy of 2.8keV to 10keV, a beam size of 5nm (uniform), and a step size of 1nm. A result is shown in figure 2.17. Here, the profiles were all normalized, and the backscatter profile was inverted for ease of comparison. Here, it can be seen that in the case of transmission imaging, the profile is less steep at the boundary than it is for higher energies. The same effect cannot be seen for backscatter imaging, where the profile becomes slightly steeper at low energies.

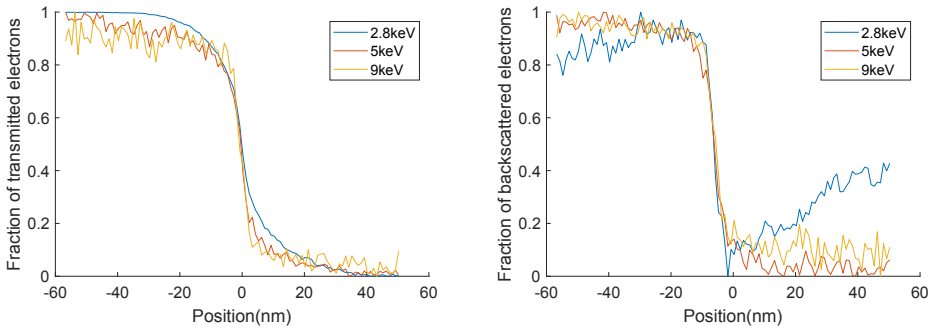


(a) (b)

Figure 2.17: Profiles of a line scan across a boundary between two materials in tissue. Graphs show the normalized (a) Transmitted and (b) backscatterd fraction. The backscatter fraction was inverted for ease of comparison.

Using these calculated data sets, we can now calculate the edge resolution as a function of landing energy for both transmission imaging and backscatter

imaging. The result is shown in figure 2.18. It shows the 25-75 edge resolution as a function of landing energy for a section thickness of 100nm and 50nm. At high energies, both detection methods show a 25-75 edge resolution around 5nm, and until 5 keV, there is no difference between the two methods. There is a transition energy where the edge resolution of both methods grows between 7 and 5 keV. When the landing energy, however, drops below 5 keV, the difference between the two becomes clear. At landing energies below 4keV, the 25-75 edge resolution has doubled for transmission imaging, where it is still around 5nm of backscatter imaging. From figure 2.17, we can see that the difference in edge resolution is mostly situated in the tails; this means that instead of 25-75 edge resolution, we would consider 35-65 (the standard for some companies like Thermo Scientific), there is no change of edge resolution with energy and the resolutions for both detection methods are the same.

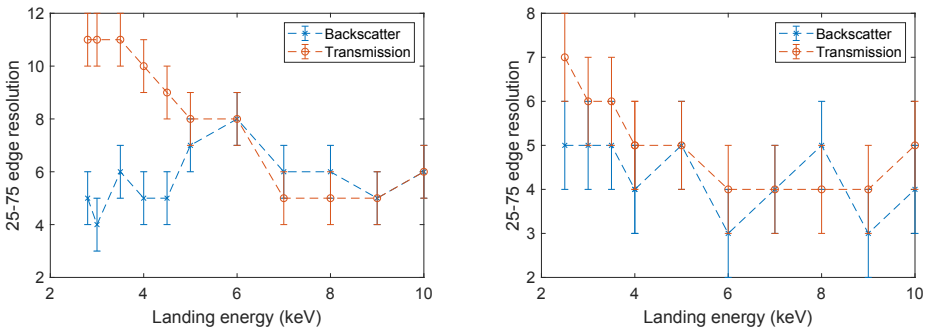


(a) (b)

Figure 2.18: Graphs showing the simulated dependence of 25-75 edge resolution on landing energy for both transmission imaging and backscatter imaging. Shown for a section thickness of (a) 100nm and (b) 50nm. The error bars are the beam step size of 1nm in the simulation.

In tissue images, the difference is hard to quantify due to unknown factors such as actual probe size and local composition and structure. In general, it has been noted that the images at lower energies tend to look slightly 'softer' than those at higher energies and the images taken using backscatter imaging. An image acquired using transmission imaging and one using backscatter imaging is shown in figure 2.19. These images were simultaneously acquired with a pixel size of 4nm and landing energy of 3keV. When looking at the images, the image acquired with transmission detection looks, as was expected, less sharp than the one acquired with backscatter imaging. The backscatter image shows more detail in between the granules and at double membrane structures. The measured edge resolutions were 14 and 9 for transmission imaging and backscatter imag-

ing, respectively. Note here as well that the transmission image looks to have a worse SNR than the backscatter image, which is also as expected from the calculation earlier in this chapter. It is, therefore, better to stick to slightly higher energies to keep a good edge resolution and SNR.



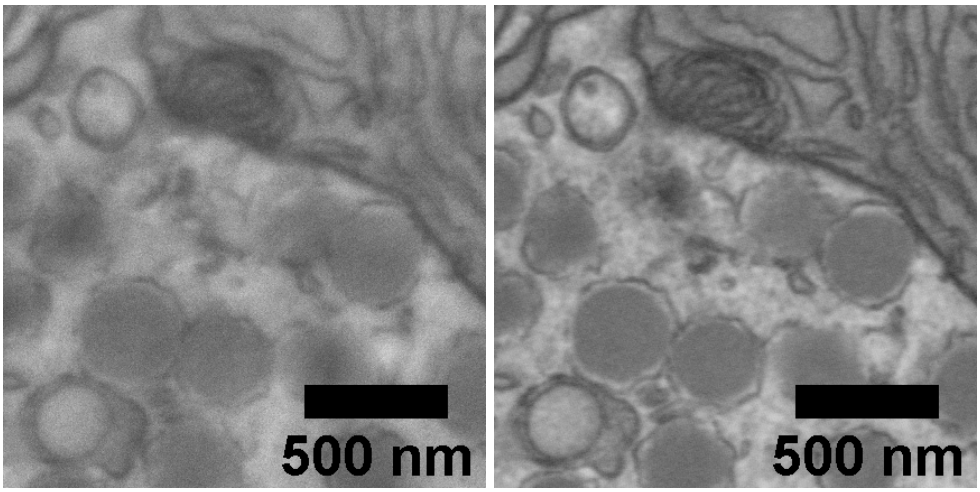


(a) (b)

Figure 2.19: (a) Transmission image and (b) backscatter image taken of Pancreatic tissue sections with a thickness of 70nm at a landing energy of 3keV, a dwell time of 3µs , and a 0.8nA beam current.

## 2.7. SUMMARY AND CONCLUSIONS

In summary, we have made a noise transfer model for transmission imaging in an (MB)SEM in order to calculate the CNR and SNR. The model considers the CNR between a stained membrane and the surrounding unstained embedding resin in both transmission and backscatter imaging. The input variables for the model were calculated using Monte Carlo simulations. The model was verified using both a test sample and stained tissue sections. The effects of changing the staining, section thickness, scintillator coating material, thickness, and detection parameters show that:

- There is a landing energy where the product of the CNR and SNR of the imaging method shows a maximum.
- Staining has a larger effect on the CNR than on the SNR. This also holds for the section thickness. The CNR increases with increased staining and section thickness, where the SNR is fairly constant.

- The thickness of the Boron (or another material) coating on the scintillator shifts the optimum energy for imaging but has little effect on the imaging performance (SNR and CNR).
- Changing the scintillator coating material does not change the imaging performance if the mass thickness is kept constant.
- Increasing the collection efficiency or scintillator quantum efficiency has a beneficial effect on the imaging performance, albeit relatively small compared to staining.
- The transmission imaging presented in this work performs better than backscatter imaging of heavy metal-stained embedded tissue sections.

Concluding, the imaging method discussed in this paper can outperform backscatter imaging and is suitable for use in the MBSEM.

# BIBLIOGRAPHY


[1] K. L. Briggman and D. D. Bock, "Volume electron microscopy for neuronal circuit reconstruction", *Current Opinion in Neurobiology*, vol. 22, no. 1, pp. 154–161, 2012, ISSN: 09594388. DOI: 10.1016/j.conb.2011.10.022. [Online]. Available: http://dx.doi.org/10.1016/j.conb.2011.10.022.

[2] N. Ohno, M. Katoh, Y. Saitoh, S. Saitoh, and S. Ohno, "Three-dimensional volume imaging with electron microscopy toward connectome", *Microscopy (Oxford, England)*, vol. 64, no. 1, pp. 17–26, 2015. DOI: 10.1093/jmicro/dfu112.

[3] M. Joesch, D. Mankus, M. Yamagata, *et al.*, "Reconstruction of genetically identified neurons imaged by serial-section electron microscopy", *eLife*, vol. 5, pp. 1–13, 2016. DOI: 10.7554/elife.15015.

[4] C. Sommer, C. Straehle, U. Kothe, and F. A. Hamprecht, "Ilastik: Interactive learning and segmentation toolkit", *Proceedings - International Symposium on Biomedical Imaging*, pp. 230–233, 2011, ISSN: 19457928. DOI: 10.1109/ISBI.2011.5872394.

[5] V. Kaynig, A. Vazquez-Reina, S. Knowles-Barley, *et al.*, "Large-scale automatic reconstruction of neuronal processes from electron microscopy images", *Medical Image Analysis*, vol. 22, no. 1, pp. 77–88, 2015, ISSN: 13618423. DOI: 10.1016/j.media.2015.02.001. [Online]. Available: http://dx.doi.org/10.1016/j.media.2015.02.001.

[6] K. Lee, J. Zung, P. Li, V. Jain, and H. S. Seung, "Superhuman Accuracy on the SNEMI3D Connectomics Challenge", no. Nips, pp. 1–11, 2017. arXiv: 1706.00120. [Online]. Available: http://arxiv.org/abs/1706.00120.

[7] C. Riedesel, I. Müller, N. Kaufmann, *et al.*, "First demonstration of a 331-beam SEM", vol. 1095931, no. March, p. 114, 2019. DOI: 10.1117/12.2528795.

[8] J. T. Neumann, T. Garbowski, W. Högele, *et al.*, "High-throughput multi-beam SEM: quantitative analysis of imaging capabilities at IMEC-N10 logic node", *Metrology, Inspection, and Process Control for Microlithography XXXI*, vol. 10145, no. March 2017, 101451S, 2017. DOI: 10.1117/12.2257980.

[9] A. L. Eberle, S. Mikula, R. Schalek, J. Lichtman, M. L. K. Tate, and D. Zeidler, "High-resolution, high-throughput imaging with a multibeam scanning electron microscope", *Journal of Microscopy*, vol. 259, no. 2, pp. 114–120, 2015, ISSN: 13652818. DOI: 10.1111/jmi.12224.

[10] C. W. Hagen, P. Kruit, C. W. Hagen, and P. Kruit, "Multibeam scanning electron microscope : Experimental results Multibeam scanning electron microscope : Experimental results", vol. 5, no. 2010, 2016.

[11] Y. Ren and P. Kruit, "Transmission electron imaging in the Delft multibeam scanning electron microscope 1 Transmission electron imaging in the Delft multibeam scanning electron microscope 1", *Journal of Vacuum Science and Technology B*, vol. 34, 2016. DOI: 10.1116/1.4966216. [Online]. Available: http://dx.doi.org/10.1116/1.4966216.

[12] J. Kuipers, P. de Boer, and B. N. G. Giepmans, "Scanning EM of non-heavy metal stained biosamples: Large-field of view, high contrast and highly efficient immunolabeling", *Experimental Cell Research*, vol. 337, no. 2, pp. 202–207, 2015, ISSN: 10902422. DOI: 10.1016/j.yexcr.2015.07.012.

[13] M. Kuwajima, J. M. Mendenhall, L. F. Lindsey, and K. M. Harris, "Automated Transmission-Mode Scanning Electron Microscopy (tSEM) for Large Volume Analysis at Nanoscale Resolution", *PLoS ONE*, vol. 8, no. 3, pp. 1–14, 2013, ISSN: 19326203. DOI: 10.1371/journal.pone.0059573.

[14] U. Golla, B. Schindler, and L. Reimer, "Contrast in the transmission mode of a low-voltage scanning electron microscope", vol. 173, no. November 1993, 1994.

[15] S. R. A. Boyde, "A new method of scanning electron microscopy for imaging biological tissues", *Nature*, vol. 302, no. 7, pp. 522–523, 1983.

[16] W. Zuidema, J. P. Hoogenboom, and P. Kruit, "Improved Image Quality in SEM Imaging of Thin Tissue Sections", *Microscopy and Microanalysis*, vol. 23, no. S1, pp. 564–565, 2017, ISSN: 1431-9276. DOI: 10.1017/s1431927617003506.

[17] F. Timischl, "The Contrast-to-Noise Ratio for Image Quality Evaluation in Scanning Electron Microscopy", *SCANNING*, vol. 37, no. December 2014, pp. 54–62, 2015. DOI: 10.1002/sca.21179.

[18] F. Timischl, M. Date, and S. Nemoto, "A statistical model of signal–noise in scanning electron microscopy", *Scanning*, vol. 34, no. 3, pp. 137–144, 2012.

[19] J. Hejna, "Noise coefficients of backscattered electron detectors for low voltage scanning electron microscopy", *Journal of Microscopy*, vol. 252, no. 1, pp. 35–48, 2013.

[20] D. Drouin, A. R. Couture, D. Joly, X. Tastet, V. Aimez, and R. Gauvin, "CASINO V2.42 - A fast and easy-to-use modeling tool for scanning electron microscopy and microanalysis users", *Scanning*, vol. 29, no. 3, pp. 92–101, 2007. DOI: 10.1002/sca.20000.

[21] H. Schatten and James Pawley, *Biological Low-Voltage Scanning Electron Microscopy*, 1st ed. Springer Science, 2008, ISBN: 9780387729701. DOI: 10.1007/978-0-387-72972-5. [Online]. Available: https://doi.org/10.1007/978-0-387-72972-5.

[22] K. Scott and N. W. M. Ritchie, "Analysis of 3D elemental mapping artefacts in biological specimens using Monte Carlo simulation", *Journal of Microscopy-Oxford*, vol. 233, no. October 2008, pp. 331–339, 2009. DOI: 10.1111/j.1365-2818.2009.03124.x.

[23] P. Hennig and W. Denk, "Point-spread functions for backscattered imaging in the scanning electron microscope", *Journal of Applied Physics*, vol. 102, no. 12, 2007, ISSN: 00218979. DOI: 10.1063/1.2817591.

[24] K. J. Hayworth, D. Peale, M. Januszewski, *et al.*, "GCIB-SEM : A path to 10 nm isotropic imaging of cubic millimeter volumes", vol. im, 2019.

[25] A. A. Sousa, A. A. Azari, G. Zhang, and R. D. Leapman, "Dual-axis electron tomography of biological specimens: Extending the limits of specimen thickness with bright-field STEM imaging", *Journal of Structural Biology*, vol. 174, no. 1, pp. 107–114, 2011. DOI: 10.1016/j.jsb.2010.10.017. [Online]. Available: http://dx.doi.org/10.1016/j.jsb.2010.10.017.

[26] P. Schauer and J. Bok, "Book: Innovation possibilities of scintillation electron detector for SEM", in *IMC 2014*. [Online]. Available: http://www.microscopy.cz/html/1674.html.

[27] H. S. H Drescher, L Reimer, "Backscattering and secondary electron emission of 10-100 keV electrons in scanning electron microscopy", *Z. ANGEW PHYSIK*, vol. 29, no. 6, 1970.

[28] A. Zonnevylle, R. Van Tol, N. Liv, *et al.*, "Integration of a high-na light microscope in a scanning electron microscope", *Journal of Microscopy*, vol. 252, no. 1, pp. 58–70, 2013.

[29] *Secom: Ultrastructure and fluorescence imaging in one clem system*. [Online]. Available: https://www.delmic.com/en/products/clem-solutions/secom.

[30] D. G. C. Hildebrand, J. W. Lichtman, and R. J. Weinberg, "Imaging ATUM ultrathin section libraries with WaferMapper : a multi-scale approach to EM reconstruction of neural circuits", vol. 8, no. June, pp. 1–18, 2014. DOI: 10.3389/fncir.2014.00068.

[31] L. Reimer, *Scanning Electron Microscopy: Physics of Image Formation and Microanalysis*, 2nd ed. Springer, 1998, ISBN: 9783642083723. DOI: 10.1007/978-3-540-38967-5. [Online]. Available: doi.org/10.1007/978-3-540-38967-5.

[32] V. Lešer, M. Milani, F. Tatti, Ž. Pipan Tkalec, J. Štrus, and D. Drobne, "Focused ion beam (fib)/scanning electron microscopy (sem) in tissue structural research", *Protoplasma*, vol. 246, no. 1, pp. 41–48, 2010.

[33] Y. Kubota, J. Sohn, and Y. Kawaguchi, "Large Volume Electron Microscopy and Neural Microcircuit Analysis", vol. 12, no. November, pp. 1–12, 2018. DOI: 10.3389/fncir.2018.00098.

[34] Y. Kubota, J. Sohn, S. Hatada, *et al.*, "A carbon nanotube tape for serial-section electron microscopy of brain ultrastructure", *Nature Communications*, no. 2018, pp. 1–3, ISSN: 2041-1723. DOI: 10.1038/s41467-017-02768-7. [Online]. Available: http://dx.doi.org/10.1038/s41467-017-02768-7.

[35] W. Ren, X. Liu, X. Hu, *et al.*, "Inspection of wafer and mask", no. August 2019, 2020. DOI: 10.1117/12.2536565.

[36] Y. Ren, *PhD Thesis: Imaging Systems for the Delft Multi- Beam Scanning Electron Microscope 1*. 2017, ISBN: 9789462957114. DOI: 10.4233/uuid.

[37] F. Grillon, "Low Voltage Contrast with an SEM Transmission Electron Detector", vol. 161, pp. 157–161, 2006. DOI: 10.1007/s00604-006-0535-8.

[38] F. Salvat, A. Jablonski, and C. J. Powell, "ELSEPA—Dirac partial-wave calculation of elastic scattering of electrons and positrons by atoms, positive ions and molecules.", vol. 165, pp. 157–190, 2005. DOI: 10.1016/j.cpc.2004.09.006.

[39] M. Hannachi, Z. Rouabah, C. Champion, and N. Bouarissa, "Electron backscattering from solid targets: Elastic scattering calculations", *Journal of Electron Spectroscopy and Related Phenomena*, vol. 195, pp. 155–159, 2014, ISSN: 03682048. DOI: 10.1016/j.elspec.2014.07.006. [Online]. Available: http://dx.doi.org/10.1016/j.elspec.2014.07.006.

[40] D. Joy and S. Luo, "An empirical stopping power relationship for lowâenergy electrons", *Scanning*, vol. 11, no. 1 989, pp. 176–180, 1989, ISSN: 01610457. DOI: 10.1002/sca.4950110404. [Online]. Available: http://onlinelibrary.wiley.com/doi/10.1002/sca.4950110404/abstract.

[41] A. M. Seligman, H. L. Wasserkrug, and J. S. Hanker, "A new staining method (OTO) for enhancing contrast of lipid–containing membranes and droplets in osmium tetroxide–fixed tissue with osmiophilic thiocarbohydrazide(TCH).", *The Journal of cell biology*, vol. 30, no. 2, pp. 424–432, 1966, ISSN: 00219525. DOI: 10.1083/jcb.30.2.424.

[42] D. Joy, "SMART – a program to measure SEM resolution and", *Journal of Microscopy*, vol. 2018, no. Pt 1 October, pp. 24–34, 2002. DOI: 10.1093/oxfordjournals.jmicro.a023869.

[43] H. Demers, N. Poirier-Demers, A. R. Couture, *et al.*, "Three-dimensional electron microscopy simulation with the CASINO Monte Carlo software", *Scanning*, vol. 33, no. 3, pp. 135–146, 2011, ISSN: 01610457. DOI: 10.1002/sca.20262.

# 3

# CONSIDERATIONS FOR TRANSMISSION DETECTION

## 3.1. INTRODUCTION

In the previous chapter, the transmission imaging system of the multi-beam SEM was discussed in detail. It discusses the contrast mechanism, the optimal landing energy, and the best coating layer. This chapter will discuss physical design parameters for signal generation and detection and their optimization in a transmission detector for multi-beam SEM. These parameters specifically are:

- - Detector type
- Choice of scintillator material
- Scintillator quality
- Saturation of the scintillator

An important aspect to consider is the final resolution of the imaging system and the potential loss of resolution due to non-optimal layouts or conditions. This chapter will discuss these items, their impact on image formation, issues, and possible solutions.

## 3.2. DETECTOR SELECTION

In this section, various detector options will be discussed. To decide what detector is appropriate, the following assumptions were made. The current of the individual beamlets was assumed not to exceed 1nA, the energy to be lower than

10keV, and the scintillator has an efficiency of 20 photons per electron per keV. The collection efficiency in total is 5% . This translates to a maximum photon rate of 6.24 $\times 10^{10}$ photons/s on the detector. At an emission wavelength of 500nm, this equates to an input power of 25nW. This photon rate can drop with a factor of 1000 depending on the landing energy and sample, and thus, the dynamic range of the detector has to be sufficient to account for this. In general, the scintillator can be adjusted so that its emission wavelength falls in the perfect window for the detector.



The detector also has to be fast enough to deal with the lowest possible dwell times in the system. This dwell time is mostly limited by the available scintillators, which are also used as signal integrator. The decay time of the detector has to be faster or as fast as the decay time of the scintillator, which is 70ns for YAG:CE.

To make sure that the currents coming from the detector are not influenced by outside noise, the current coming from the detector has to be sufficiently high. Therefore we set a lower limit to the internal gain of at least 1000 at a radiant sensitivity of 1A/W.

The detection efficiency of the detector has to be at least 10% to not lose too much signal.

The size of the detector has to be sufficient to create a large field of view. In general, the optical system can, however, be designed to accommodate any size of detector. There is another design requirement, however, which is only applicable for multi-beam imaging. The detector has to have the shape to be placed in an array to detect all the beams in one go.

#### AVALANCHE PHOTODIODES AND PHOTODIODES

On average, approximately every 100 picoseconds, a photon will arrive on the detector. This excludes the use of avalanche photodiodes as they have a recovery time in the order nanoseconds, such that 10's of photons will not be detected, causing the detection efficiency to fall below 10% [1]–[4].

On the other end, a photodiode has no built-in gain. At sensitivities in the order of A/W, this would result in currents in the order of nA coming from the photodiode, which is a signal that is very susceptible to noise and has to be amplified immediately at the detector. This is possible but not off-the-shelf available.

#### CAMERA

The Delmic SECOM platform [5], which is used for this transmission imaging technique, is used as a fluorescence microscope. As such, it comes equipped with a camera for imaging. This camera can now also be used for transmission imaging[6]. The main disadvantage of using a camera is the limited speed. Most

cameras used in fluorescence imaging are optimized for quantum efficiency so that they detect as much of the emitted photons as possible and have little background. This, however, also limits them to 10-20 frames-per-second(fps). Cameras with higher frame rates are available. Rahangdale, Keijzer, and Kruit [7] described a way of using a 10000 fps camera as a detector for multi-beam imaging. Even at this high frame rate, each frame still has to contain one dwell time of the electron beam, limiting the dwell time to a minimum of 100μs. Even higher-speed cameras are available but are not suitable for this application, as they use extreme binning of the camera (32 × 256 pixels), yielding only a few pixels per beam in a multi-beam system. In this case, the dead space between the pixels (used for pixel readout) also becomes an issue, and light is lost as the spots move over them. The cameras can typically only image for 7.2s at a time, after which the (slow) memory has to be emptied, which creates an additional overhead. Furthermore, they are extremely expensive(upward of $100000 [8], not including the further effort required). The advantage of a camera is the spatial information it gives for each frame, removing the need for descanning in a multi-beam system. However, still, the throughput will be severely limited.



#### PMT AND PMT ARRAY

For the detection of the transmitted signal, there is no need to obtain a complete image with spatial information, and a photomultiplier tube (PMT) could be used as well. PMTs have low noise, high gain, high dynamic range, and are relatively cheap (in the order of $1000). For use in multi-beam systems, they are available in arrays. The input power of 25nW, at a typical cathode radiant sensitivity of 100mA/W and a gain of $10^4$, keeps the output current far below the maximum rating of the PMT anode of 100mA at 25μA. An example of tissue imaging with a PMT as the detector is shown in figure 3.1a. For this image, the camera of the SECOM platform was replaced by the PMT, and the tube lens of the microscope was removed to defocus the spot on the detector. If a PMT is used without any descan system, the maximum field of view is governed by the magnification of the microscope objective in the system and the sensitive area of the PMT. A PMT with a sensitive area of 8mm and a 40x objective means that the SEM field of view is 200μm . This field of view size can be adjusted by adopting the optical system and reducing the final magnification at the detector.

#### SIPM

The last photon detector that will be discussed is the Silicon Photomultiplier(SiPM) or Multi-Pixel Photon Counter(MPPC). SiPMs are commonly used in radiation detectors for applications such as Proton Emission Tomography (PET). They are

Typical values taken from www.hamamatsu.com

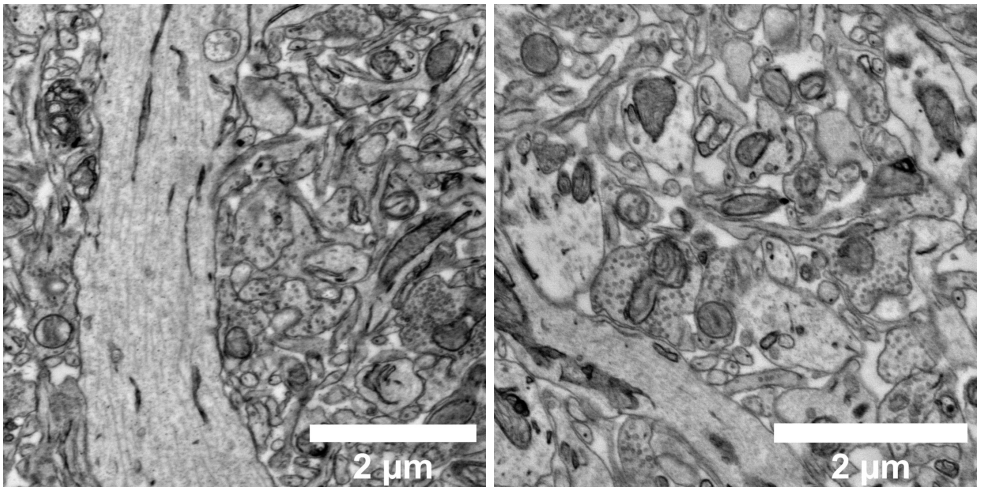


(a) (b)

Figure 3.1: Image of brain tissue obtained with transmission detection with an (a)PMT and a (b) multi-pixel photoncounter as a photon detector. The image was recorded at a landing energy of 4keV, 0.8nA beam current, and a 1µs dwell time.

favorable because of their high timing resolution, high detection efficiency, small form factor, and operation in the neighborhood of high magnetic fields. As the name suggests, SiPMs can replace PMTs in most applications. A schematic of a SiPM is shown in figure 3.2a. A SiPM is an array of passively quenched APDs connected parallel. Any single APD will still have the shortcomings of the single APD, but in this case, while one APD is recovering, another APD can still receive a photon as long as the light beam is spread out enough not to hit the same APD twice. The density of APDs on a single SiPM can be tuned according to the application and ranges from 168 APD/mm$^2$ (75µm APDs) to 10000 APD/mm$^2$(10 µm APDs). As the APD count in a SiPM gives the number of photons that can be detected simultaneously, a higher APD count means a higher dynamic range. There is, however, a trade-off to be made there, as the fill factor of the detector goes down significantly with smaller individual APDs. This is illustrated by figure 3.2b; as the cells become smaller, the circuitry stays roughly the same size. This creates a lower fill factor and, thus, a smaller sensitive area per APD. The fill factor determines the ultimate photon detection efficiency (PDE), which ranges from 50% at a fill factor of 82% (for 75µm APD size) to 10% at a fill factor of 30% (for 10µm APD size). Another adverse effect of having smaller APDs is the increased dark current, which reduces the dynamic range somewhat because low-light applica-

Brandname mainly used by Hamamatsu

tions will fall in the dark current range. This means that for each application, there can be a different ideal size of MPPC with a superior APD density. In our case, and assuming an APD recovery time of 63ns and a photon detection efficiency of 50% (of the SiPM), we need a minimum of 2000 APDs in the SiPM per beamlet. Within the Hamamatsu catalog, the optimum APD size is now 50μm on sensors of 3x3mm [9]. An example of transmission imaging of tissue using a SiPM as a photon detector can be found in figure 3.1b. The setup used here was the same as the one used to obtain figure 3.1a.



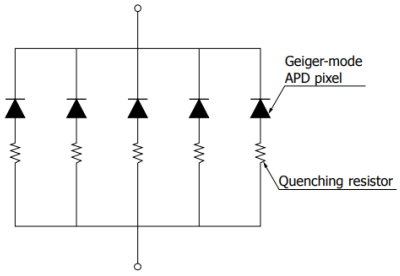


(a)

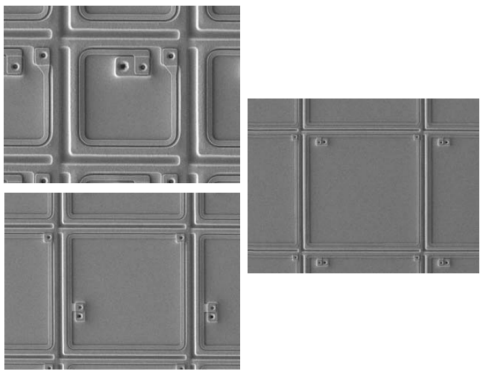

(b)

Figure 3.2: (a) Schematic drawing of a SiPM (b) SEM images of the physical structure of SiPMs. The top left has a 25μm cell size, the bottom left 50 μm , and the right 75 μm .

## 3.3. SCINTILLATOR SELECTION

When employing the detection technique described here, the choice of scintillator can greatly impact the whole system and the image it produces. Important aspects of the scintillator that should be considered are:

- The scintillator should not bleach in the short term, in the order of minutes of exposure to the electron beam. Under typical operating conditions of a max current of 1nA and <10keV, the beam energy is focused on a 4nm diameter spot.
- The emission wavelength should be high enough to be transmitted by the lenses in the objective lens, which sets the lower limit at a wavelength of 500nm.
- The 1/e emission decay time should be lower than the lowest dwell time, which is set at 100ns. Otherwise, streaking artifacts will occur.

| Name | ρ(g/cc) | τ(ns) | Photons/keV | λ(nm) | $ |
|---|---|---|---|---|---|
| YAP:CE | 5.35 | 30[10] | 16.2[10] | 347[10] | $$$ |
| CRY18 | 4.5 | 48[10] | 30[11] | 400[10] | $$$$$ |
| LYSO:CE | 7.2 | 40[12] | 27[12] | 450[13] | $$ |
| YAG:CE | 4.56 | 70[10] | 11[10] | 550 [10] | $$ |
| LuAG:CE | 6.73 | 70[11]-100 [10] | 17[10]-25[12] | 535 [11] | $$$$ |
| EJ-296[14] | 1.02 | 2.5 | 9 | 435 | $\frac{1}{1000}$$ |

Table 3.1: An overview of the possible scintillators for transmission imaging. The numbers shown are taken from various sources. All of the scintillators are inorganic single crystals except for EJ-296, which is an organic scintillator paint. ρ is the density, τ the 1/e decay time and λ is the peak wavelength. The $ column shows the relative price of the scintillators from experience.

- A lower backscatter coefficient is better, as more transmitted electrons are converted to light.

A scintillator that bleaches too quickly might be useless for our detection method, especially if the scintillator is to be used again. A single-time use could still handle a small amount of bleaching. The emission decay time also has effects on the saturation behavior of the scintillator (to be discussed in section 3.5). Table 3.1 shows an overview of the scintillators that will be discussed in this section.

#### BLEACHING BEHAVIOR

The first factor to be discussed is the bleaching behavior of scintillators. Bleaching is here defined as an irreversible drop in light output of the scintillator after electron irradiation. None of the single crystal scintillators showed any bleaching; the one organic scintillator, however, did show significant bleaching after imaging. This scintillator is mostly interesting because of its very low price. As this scintillator comes in paint form, one bottle of 100ml (costing around 150$ can be used to coat thousands of glass substrates with a scintillator. Another advantage of organic scintillators is the very short decay time, which will reduce the saturation of the scintillator(section 3.5). An example of a scintillator after bleaching is shown in figure 3.3. After this bleaching was observed, no further investigations were performed on the bleaching behavior. If the bleaching is slow enough, it might be possible to acquire images at low dwell time and low current. The bleaching does not occur only at the electron beam focus position but spreads out a few 100nm around the beam spot. Therefore, the scintillator has to bleach slower than it typically takes to acquire one image, which is in the order of seconds. Figure 3.3 does suggest that this is possible, as hints of structures in the tissue can be seen in the unbleached part of the scintillator. An option

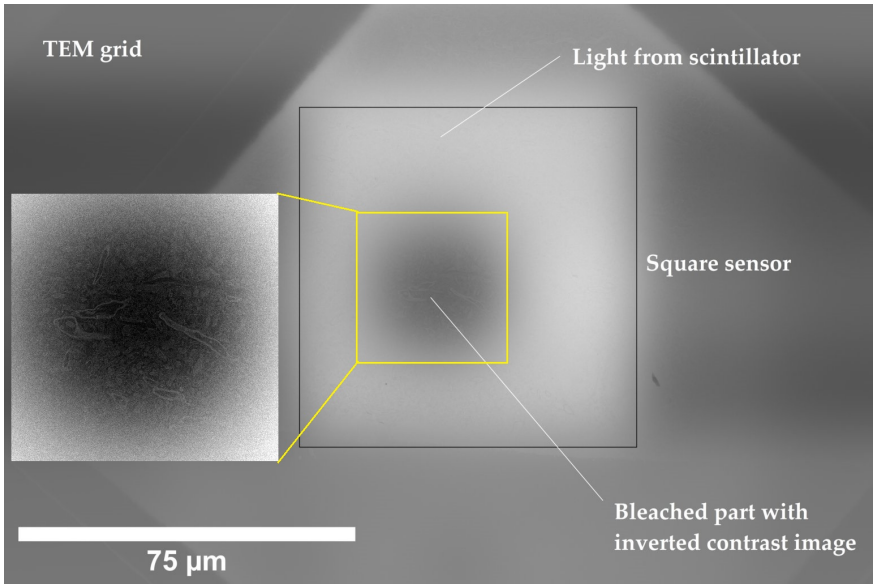


Figure 3.3: Image of brain tissue on a TEM grid mounted on top of organic scintillator paint EJ-296 on a glass substrate with a conductive Boron coating on top. The white square shows the outline of the sensitive area of the MPPC detector. In the center, a bleached area is visible, which was bleached while zooming into that area during earlier imaging. In this area, some tissue structures can be observed in dark-field contrast (see zoomed-in inset).



would be to calibrate for the bleaching behavior and adjust using digital gain per pixel. This can be done by imaging an empty scintillator and adjusting the gain per pixel such that all pixels have the same value. The main limitations to this approach are shot noise and total signal drop. If the drop is too high, the SNR will become very low (see chapter 2).

An interesting observation was that, in the bleached area, an image of the sample with inverted contrast shows up. The contrast in this image becomes better at high energies, which suggests that it is a dark-field contrast mechanism; a possible explanation of this will be given in section 3.5.3.

#### EMISSION WAVELENGTH

The emission wavelength of the scintillator is important for mainly two parts of the detection chain. The first of these is the optical system. All the lenses and mirrors in the system have a coating that is tuned to a specific wavelength range. This means that if a certain scintillator is chosen, most parts can be adjusted to its wavelength. One part of the optical system that can, however, not be changed is the objective lens. When an objective with a high numerical aperture is required that is readily available, apochromat-type objectives are the most obvious

choice. The transmission spectrum of this objective type, together with the emission spectra of the discussed scintillators, is shown in figure 3.4a. It shows that YAG:CE is best tuned for the objective and that when YAP:CE is used, a large part of the light will not pass through the objective. Note that a reflective objective could be used, but then the numerical aperture is typically limited to 0.5. [15], [16]. The second important factor is the efficiency of the detector at the emission band of the scintillator. The efficiency of the detector with the spectra of the scintillators is shown in figure 3.4b. Considering the use of a SiPM detector, YAP:CE emission shows negligible overlap with the detector efficiency curve.In terms of detector efficiency, LYSO:CE would be the optimal scintillator material, as its emission spectrum completely overlaps with the detection range.

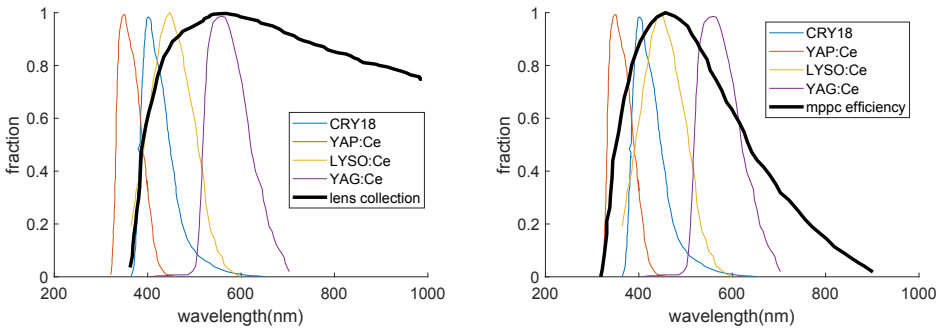


(a) (b)

Figure 3.4: Emission spectra of the scintillators in table 3.1, plotted with (a) the transmission spectrum of a Nikon Plan Apochromat objective and (b) the detection efficiency spectrum of a Hamamatsu SiPM. All spectra have been normalized; that of LUAG:CE has been omitted because it is very similar to that of YAG:CE. Data for CRY18 and YAP(Ce)) taken from Schauer and Bok [10], YAG:CE from Crytur [11] and LYSO:CE from Samuel, Aurélie, Bruno, *et al.* [13].

### DECAY TIME

Another important factor to take into account when selecting a scintillator is the emission decay time($\tau$). The decay time of a scintillator is usually defined as the time it takes after excitation for the emission intensity to drop below 1/e of its peak value.

$$out = I_{peak} \times e^{-\frac{t}{\tau}} \tag{3.1}$$

This is most important when a system uses short dwell times. At, for instance, a dwell time of 50ns and a scintillator lifetime of 70ns(YAG:Ce), 50% of the signal created in one pixel gets carried over to the next and 24% to the one next to that (as per equation (3.1). At a decay time of 40ns(LYSO:Ce), this drops to 29% and

8% , respectively. This effect is called streaking and is seen in SEM images with a short dwell time. To visualize this effect, we can look at the Fourier transform of an image. In a tissue section without any periodic structures, one would expect no clear peaks in the Fourier spectrum at higher spatial frequencies. When there is streaking in the scan direction, this causes a loss of high-frequency information. This shows up as a vertical band in the Fourier transform. An example of this is shown in figure 3.5, where we used the LuAG:Ce scintillator, which has a decay time of 70ns. Figure 3.5a has been acquired at a dwell time of 1000ns and has no clear structure except for a narrow band in the scan direction. Figure 3.5b, however, has a very clear band in the scan direction, which indicates that the dwell time is too close to the decay time of the scintillator. The absolute difference in FFT figure 3.5c clearly shows that higher frequencies are lost. Only at dwell times between 300ns and 400ns, this band starts to disappear from the Fourier transform. Thus, using LuAG:CE would limit the lowest possible dwell time to 300ns if the imaging artifact is unacceptable for the application.



#### BACKSCATTER COEFFICIENT

The last aspect to consider is the backscatter coefficient of the scintillator. If the backscatter coefficient is higher, fewer electrons create light in the scintillator, causing a lower detection efficiency. In general, the backscatter coefficient is determined by the density of the material and the atomic number. For example, the density of LYSO:Ce is 7.2 g/cc, and that of YAG:Ce is 4.56 g/cc. When simulating these materials using CASINO Monte Carlo software with a beam energy of 5keV, we find that LYSO:Ce has a backscatter coefficient of 0.33 and YAG:Ce 0.22. Even though LYSO:CE has a higher light output than YAG:CE, the higher backscatter coefficient will reduce the difference but not as much to altogether remove the benefits of the higher photon yield.

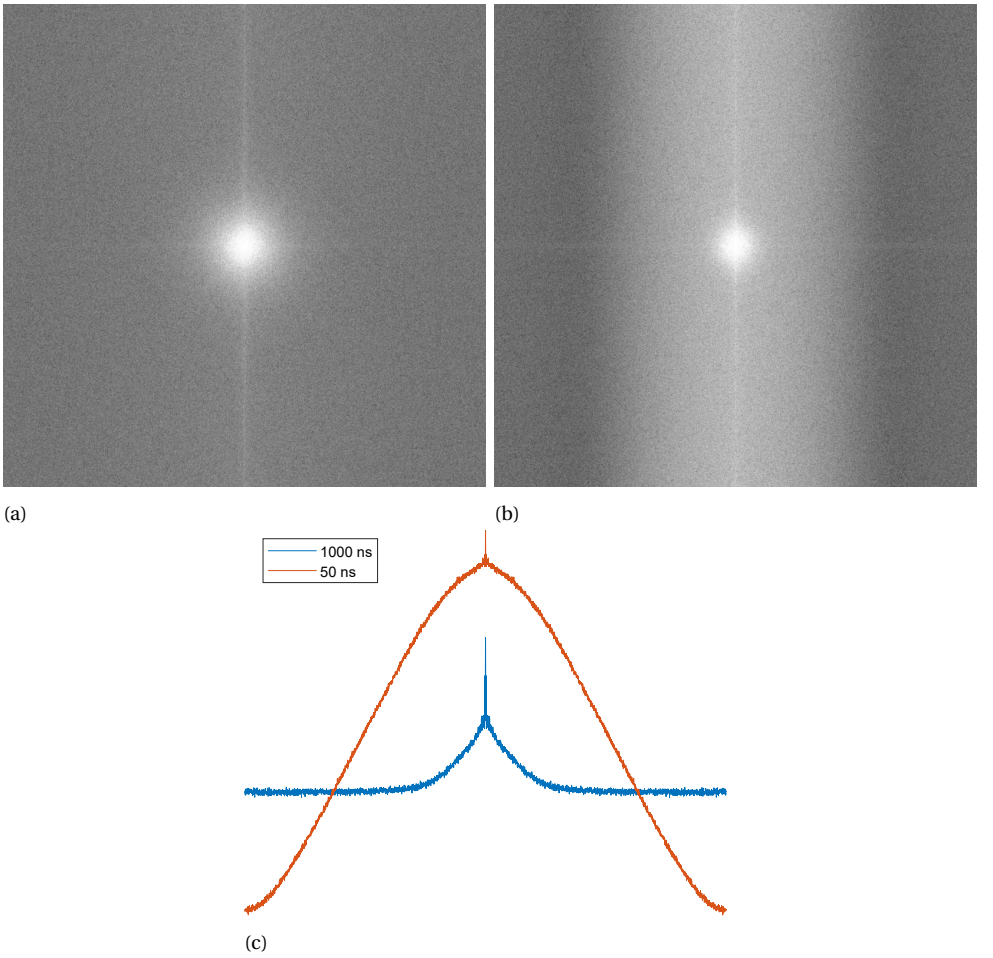


Figure 3.5: Fourier transform of a transmission image acquired at a dwell time of (a) 1000ns and (b) 50ns. The image was taken using a LuAG:Ce scintillator, which has a decay time of 70ns. The contrast and brightness of the FFT have been stretched to show the difference. (c) shows the two spectra integrated along the vertical direction; here, it is clear that higher frequency information is lost in the image.

## 3.4. SCINTILLATOR AND COATING SURFACE QUALITY

As was shown in the previous chapter, the transmission method, as described here, is highly sensitive to any variation in the local density of the sample on top of the scintillator. This also causes any variation in the scintillator surface or coating will be seen in the image. In this section, we will look at the effect of surface quality on the image from the bottom up. The following issues can be encountered:



- Dopant concentration in-homogeneity.
- Scintillator surface defects (scratches).
- Coating defects.

Some of these issues are shown in figure 3.6, which clearly indicates that these issues can cause very bad images when not taken care of.

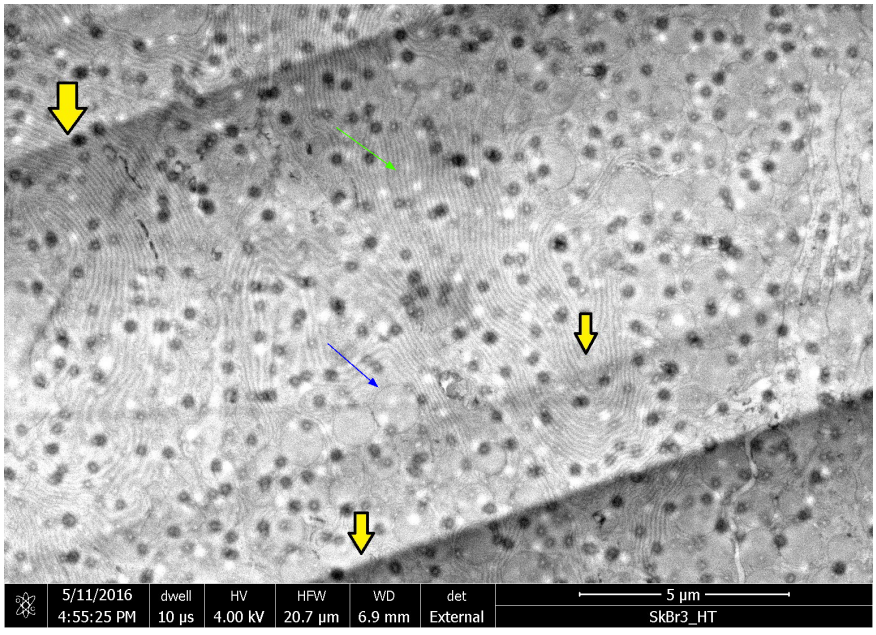


Figure 3.6: Transmission image of OTO stained rat pancreas. The effect of dopant concentration variation is marked by yellow arrows. The black spots are due to defects in the coating layer. The (green) arrow marks some endoplasmic reticulum and the (blue) arrow marks a vesicle that is visible in the image but pushed to the background.

### 3.4.1. SCINTILLATOR SURFACE DEFECTS

When the scintillator substrates are cut from the large crystal, minor surface defects might occur. The primary surface defects are scratches, as shown in figure 3.7. The scratches show up as dark lines by locally increasing the backscatter coefficient, reducing the light output. The visibility of these scratches can be reduced by making sure the beam is not entirely focused when impinging on the scintillator. To get completely rid of the scratches, however, a rigorous polishing of the scintillator has to take place. This can be done mechanically or by broad ion beam milling[17].



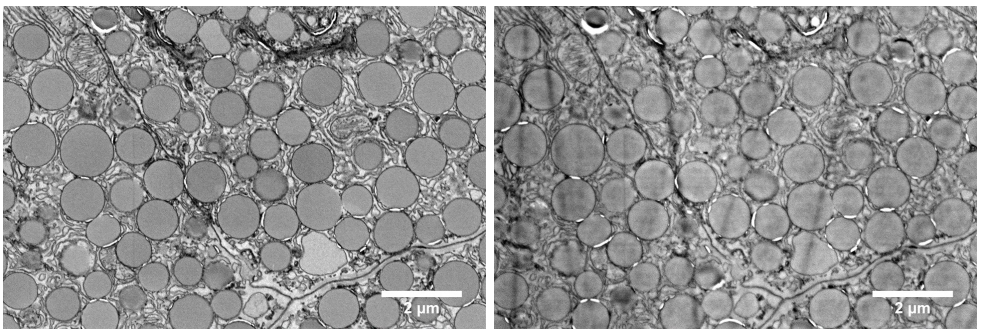


(a) (b)

Figure 3.7: (a)Backscatter and (b)transmission image of rat pancreas. The scratches in the scintillator surface are visible in the transmission image.

### 3.4.2. COATING DEFECTS (GRANULARITY)

When coating the scintillator for conductivity, the main option is to coat it with metals. In the metal coating method, we used sputter and e-beam evaporation, causing the metal to grow in tiny crystals, as shown in figure 3.8. These small crystals have gaps in between them, and this surface roughness will be visible in the transmission imaging. An example of this effect is shown in figure 3.9. To avoid this issue, multiple solutions are available. The first one is to perfect the coating growth to such an extent that granularity is no longer present. This can be done by changing the coating process to atomic layer deposition or optimizing the process parameters in sputter coating or evaporation coating. Another option is to use a coating that does not form this granular structure at all. After trying Aluminium, Molybdenum, Gold, Tungsten, Chromium, Boron, and Carbon, it was found that the latter two do not form a granular structure. Molybdenum was found to be a possible coating, as in some sputter coating parameters, it shows only very low granularity.

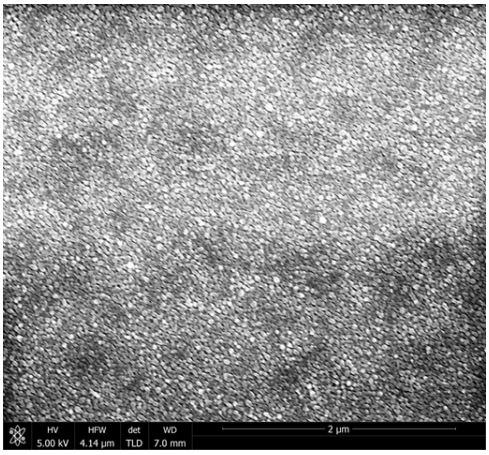


Figure 3.8: SE image of a 20nm thick Aluminum evaporation coating on YAG:CE. The granular structure of the coating is visible

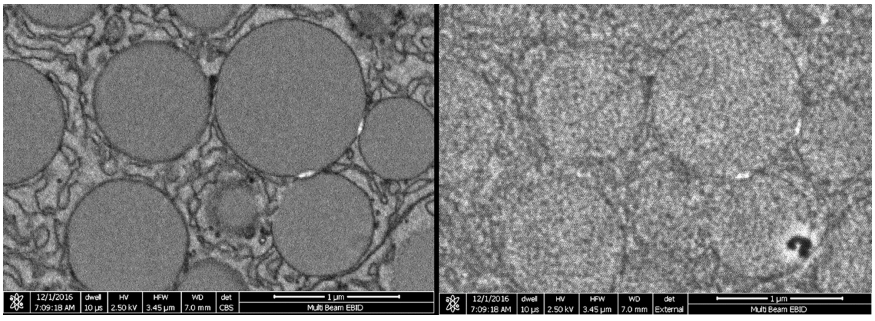


Figure 3.9: (left)Backscatter and (right)transmission image of a 50nm section on the coating shown in figure 3.8. The effect of the coating in the transmission image is visible and obscures image details.

## 3.5. SCINTILLATOR SATURATION

When imaging in transmission mode, an unexpected effect was observed. That is, if the electron beam is focused on the scintillator with a high current, the scintillator tends to saturate, and the light output is no longer linear with the beam current. A direct effect of this is shown in figure 3.10. It shows a transmission image of a TEM grid with holey carbon film stuck to a YAG:Ce scintillator with a 10nm Al coating at a beam current of 200pA. Holey carbon is usually used as a support structure for TEM samples and consists of a thin (<50nm) carbon film with uneven holes. We expect to see less light output when the beam hits the foil than when it hits a hole, as some electrons will be blocked or lose energy in the foil. This is indeed the case at a landing energy of 2.6keV as can be seen in fig-

ure 3.10a. At a slightly higher energy of 4keV however, the contrast is inverted for the same sample (figure 3.10b). This section will describe a saturation mechanism that may cause such a contrast inversion, model it, investigate the imaging consequences, and give a possible solution.



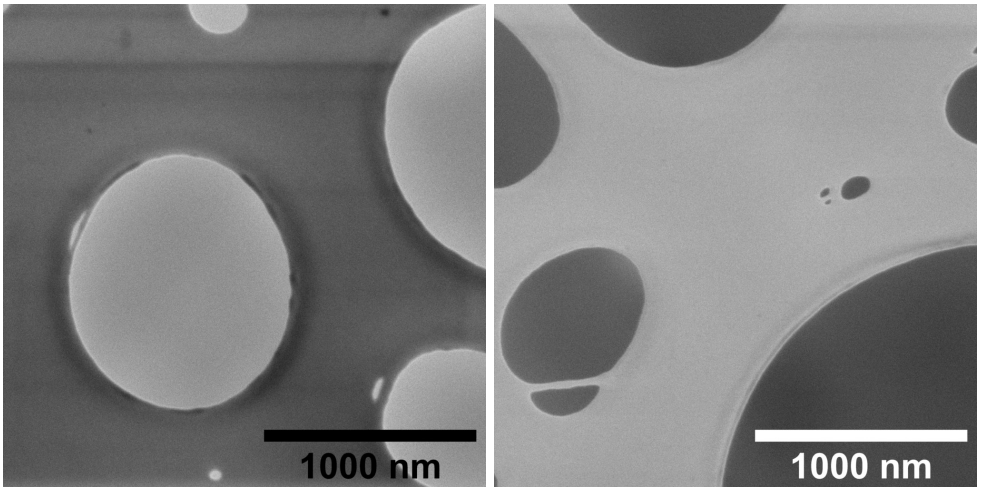


(a) (b)

Figure 3.10: Transmission images of a TEM grid with holey carbon film. Images were taken at a beam current 200pA and landing energy of (a)2.6keV and (b) 4 keV. The scale bar color was inverted for readability.

### MECHANISM

When a beam of electrons hits a scintillator, it can interact with the luminescent centers in this scintillator. The chance of a primary electron interacting with the center is minimal due to its high energy and the resulting low scattering cross-section. The primary beam, however, also creates secondary electrons within the scintillator, and the chance of these electrons interacting with a luminescent center is much greater. This interaction causes the luminescent center to get into an excited state, which relaxes to the ground state within a certain amount of time by releasing a photon. There are other mechanisms by which the center can relax, which will not be discussed here. This relaxation time is not constant, and that is why the scintillator is said to have a decay time. When an electron hits, some centers take more time to decay than others, and the light output from the scintillator takes some time to fade away. While the luminescent center is in an excited state, it cannot be excited again. YAG:Ce, for example, consists of a Yttrium Aluminium Garnet matrix with Ce doping. The luminescent centers are created by the Cerium dopant, which is present in a limited amount. From the

supplier, Crytur, we obtained the number of 1 center per $nm^3$, even though this number is not specified in further documentation. When the electron beam has a low energy and a sufficiently high current, the amount of secondary electrons in its interaction volume can now exceed the amount of free luminescent centers in that volume. This causes saturation of the light output of the scintillator. Note that this is a simple model for scintillator saturation and that, in practice, more complex effects may cause energy migration to the luminescent centers to saturate [18]. However, for our purpose of illustrating the effect of scintillator saturation on imaging performance, the above model provides an intuitive explanation. From this model and the notion that saturation may occur, we can deduct the following hypotheses:



1. Light output of a saturated scintillator increases with beam spread, as this also increases the interaction volume.

2. Saturation is less at higher beam energies as the interaction volume is bigger. An added effect is that the higher energy electrons will have less interaction with the scintillator directly underneath the beam spot. This is because the inelastic scattering cross-section of the scintillator is inversely proportional to the electron energy. The effect is somewhat mitigated by the fact that higher energy electrons will create more photons throughout the volume.

3. Saturation is less for a scintillator with a lower decay time, as more centers are available at any time (at constant beam parameters).

The first statement is the mechanism for the contrast inversion in figure 3.10. At higher energies, the transmission coefficient of the carbon film is very high. The carbon film does make the beam scatter and spread out before it hits the scintillator. This increases the interaction volume in the scintillator underneath the film, as compared to underneath a hole. Another measurement has been performed on tissue directly lying on top of a coated scintillator. The imaging was performed at a landing energy of 4keV, a beam current of 0.4nA, and a dwell time of 16µs . The beam spot size was measured in backscatter mode as the effects that are described in chapter 2 are not present. The average image intensity as a function of beam defocus is shown infigure 3.11. From here, it is found that the light output of the scintillator increases by 20% for a defocus of 250nm, at this energy and current.

Statements 2 and 3 were checked by measuring the light output as a function of beam current for a somewhat de-focussed beam for two scintillators and four different landing energies. The scintillators used here were YAG:Ce and YAP:Ce

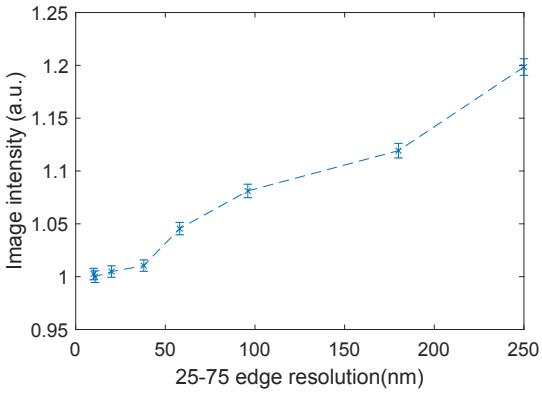


Figure 3.11: Results of a scintillator light output measurement as a function of spot size. The spot size was measured in backscatter imaging on tissue.

with 1/e decay times of 70ns and 40ns, respectively. The results are shown in figure 3.12 and figure 3.13. It shows the light output as a function of beam current, scaled between 0 and 1. The same graphs show a linear fit to the first two measurement points, at 25pA and 50pA, where the output is expected to be linear.

The effect of increasing interaction volume between 3,4, and 5 keV is not very clearly visible in the results. The effect is very small, however, when going from 3 to 15 keV. The blue line stays closer to the linear fit, which means reduced saturation.

The difference between YAP:CE and YAG:CE is also visible, as YAP:Ce shows a slightly later onset of saturation. This can be seen by the fact that the measurement point at 800pA lies slightly further away from the linear fit in YAG than it is down in YAP. The effect is not as large as might be expected, which could be due to variation in dopant concentration between YAG and YAP.

### 3.5.1. MODEL

This section will describe a model for the scintillator saturation. When a beam of electrons impinges on a scintillator, most of the secondary electrons are generated close to the point where the beam hits. Now, we can perform a quick calculation if saturation will occur. From Monte Carlo simulations performed in Casino, we find that a 5keV beam with a beam radius of 10nm loses 50% of its energy in a cylinder of length 35nm and radius 3nm. This gives a total volume of about $1000nm^3$ and thus 1000 luminescent centers. It is assumed here that the coating on top of the scintillator is of a low-density material and thin enough not to lose a significant amount of energy in this layer. With an average lifetime of

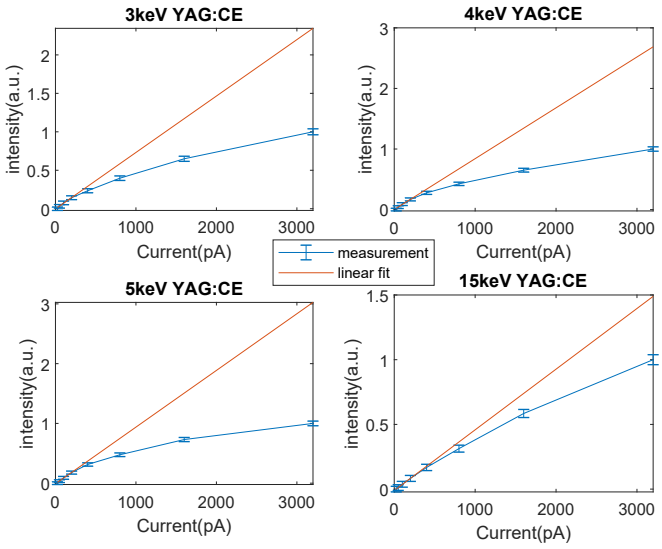


Figure 3.12: Measurement of the scintillation light output of YAG:CE as a function of beam current at four different landing energies. The output is shown in blue lines and scaled between 0 and 1. The red lines show a linear fit to the first three measurement points, where the response is still expected to be linear.

70ns for YAG:CE, this means that $1000 \times \frac{1}{7\times10^{-9}} = 1.4 \times 10^{10}$ secondary electrons can arrive per second in this volume. Let's assume a low number of 10 percent of the primary electron energy is lost due to secondary electron generation with an average energy of 15 eV, and 50 % of that happens in the volume described earlier. This means that every primary electron would generate about 17 secondary electrons, which in turn excite a luminescent center. For the volume considered, this means that this area is saturated already for a beam current of 130pA. Even this is a very conservative number, and the maximum current is most likely even lower. This means that at higher currents, less than 50 % of the electron energy is generating contrast. At the same time, the slope of the curve has reduced significantly, reducing the contrast even further.

This same process will now be more rigorously calculated using Casino. To achieve this, the following is performed. A small beam (3nm) of 5keV impinges on a 10nm Boron coating on top of a YAG:CE scintillator. For this beam, the energy loss per voxel in the scintillator is taken as an output. This energy loss can be due to several factors, including light generation. From high energy x-ray data, it is known that YAG:CE outputs about 20 000 photons/ MeV. That is 0.02 photons per eV of input energy. The light generated by YAG:CE has a wavelength

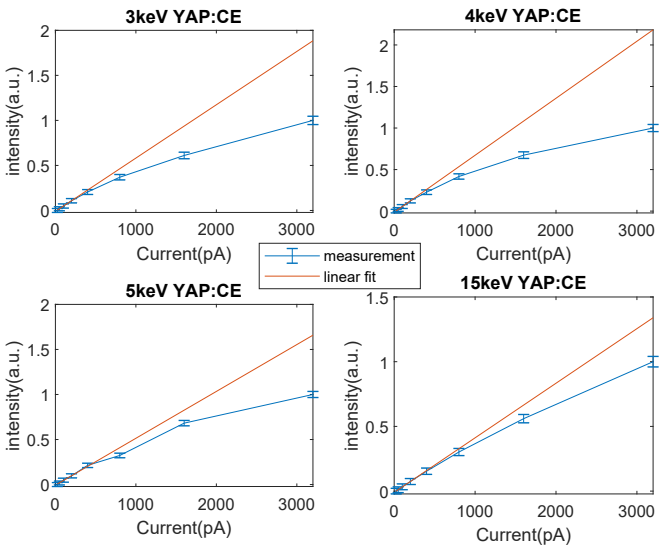


Figure 3.13: Measurement of the scintillation light output of YAP:CE as a function of beam current at four different landing energies. The output is shown in blue lines and scaled between 0 and 1. The red lines show a linear fit to the first two measurement points, where the response is still expected to be linear.

of around 550nm, corresponding to a photon energy of about 2.25 eV. This yields a photon conversion efficiency of 0.02*2.25 = 0.04 or around 4 % . Thus about 4 % of the energy loss is converted into photons.

This calculation is now performed for a 10nm layer of Boron on top of the YAG:CE scintillator and compared to experimentally acquired data. This was done for a 5keV beam and a current ranging from 130pA to 1600pA. The experimental setup was an FEI Verios microscope equipped with a Delmic SECOM system, to which an MPPC sensor was mounted for light detection. The light was collected using a 0.95 NA, 40x objective lens. The spot was slightly defocused on the MPPC sensor to avoid detector saturation.

The experimental results do not give a photon count but a relative signal. To compare the experimental results to the simulated results, the curves are compared as a percentage of the light output where the scintillators are not saturated. This is calculated for the experimental results by using a linear extrapolation of the first three low current data points. So, the results shown are relative to the maximum unsaturated output, either calculated or measured.

figure 3.14a shows that a conversion efficiency of 4% is an underestimation of and a conversion efficiency of 5% fits the experimental results better. This can

also be due to a three times higher luminescent center density or a combination of both. For the next section, a conversion efficiency of 3 % will be assumed. It can still be seen that the saturation behavior is slightly different in the experiments than in the model; the simulation will go to a steady state value as the light output in the experiments still goes up for higher currents. One reason for this could be charging in the material, which leads to the electric-field-driven migration of secondary electrons out of the interaction volume calculated with steady-state Monte Carlo simulations.

Another more likely problem is the numerical error in the Monte-Carlo simulations. They will, at some point, give a zero energy loss in a particular voxel, which might not be the case, even though the energy loss can be minimal. This will cause the scintillator to fully saturate in the simulation.

For this value of the conversion efficiency, the fraction of the unsaturated light output is calculated in the same system for three different landing energies; this is shown in figure 3.14b.

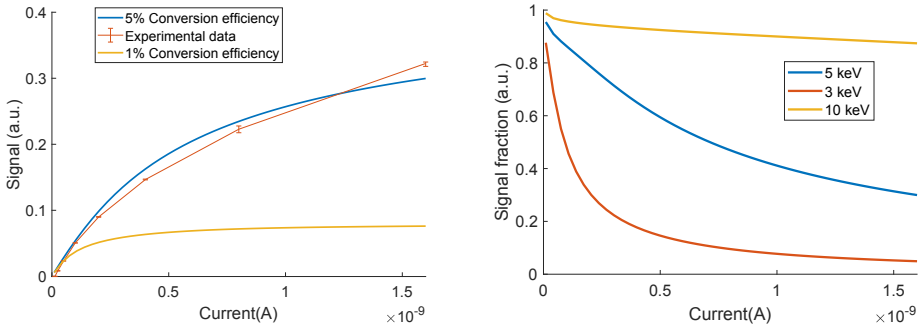


(a) (b)

Figure 3.14: (a) Measurement and model fit of scintillator saturation for a system with a 10nm B layer on top of YAG:CE impinged with a 3nm size 5keV electron beam. It shows the output signal in arbitrary units as a function of beam current. The Figure shows that the best fitting conversion efficiency lies around 5% . Further model results show the effect of landing energy in Figure (b). Saturation is more apparent at lower landing energies.

### 3.5.2. CNR AND SNR WHEN IMAGING WITH A SATURATED SCINTILLATOR

The imaging of tissue on a scintillator will be influenced by the scintillator saturation, as the slope of the light output v.s. the current curve locally is lower at higher currents. This means that the light contrast is lower, which will have an effect on the SNR and CNR. Locally, the curve can, however, still be considered

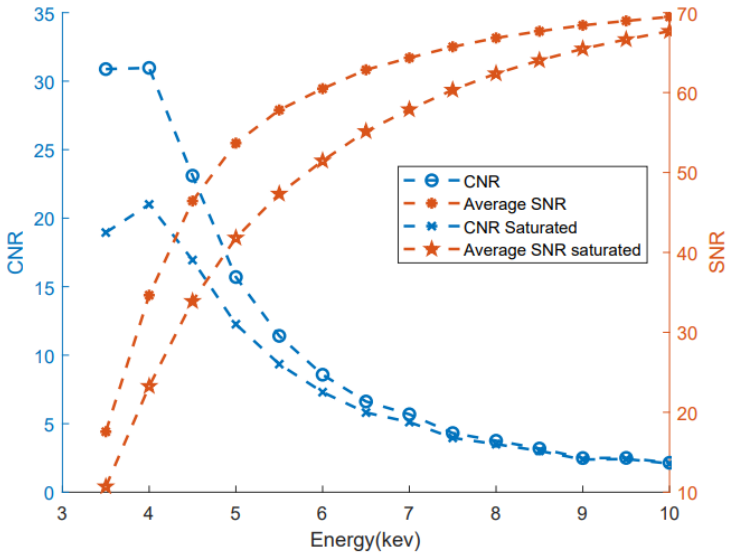


Figure 3.15: Calculation of the SNR and CNR in the case of saturated scintillator, a factor of approximately 1/3 reduces the maximum CNR.

linear. As the transmission coefficient does not change a lot over a tissue section, an estimation can be made by simply reducing the scintillator efficiency by a factor. As can be seen from figure 3.14a, the light output at a current of 1nA is around 50% of what was to be expected for an unsaturated scintillator at 5 keV. At 3 keV, this percentage has reduced to about 10% , and at a landing energy of 10keV, it is around 90% . Using this data and linearly extrapolating it, the graphs from chapter 2 can be recalculated; the result of this is shown in figure 3.15. The SNR and CNR are reduced by a significant factor, especially at low energies.

A secondary effect is not considered here, which is that at low energies, the transmission coefficients of the two features of which the CNR is calculated start to lay further apart. Therefore, at a lower transmission coefficient, the saturation is less, and the light output is increased. This is an opposing contrast mechanism that will further reduce the CRN; this effect is here, however, considered to be small.

### 3.5.3. DARK FIELD IMAGING

The saturation effect does offer the opportunity for dark field imaging. If the scintillator has a low density of light-emitting centers (or a very high current), all of them can be active simultaneously for an incoming beam. Now, the size of the electrons' interaction volume in the scintillator governs the light output.

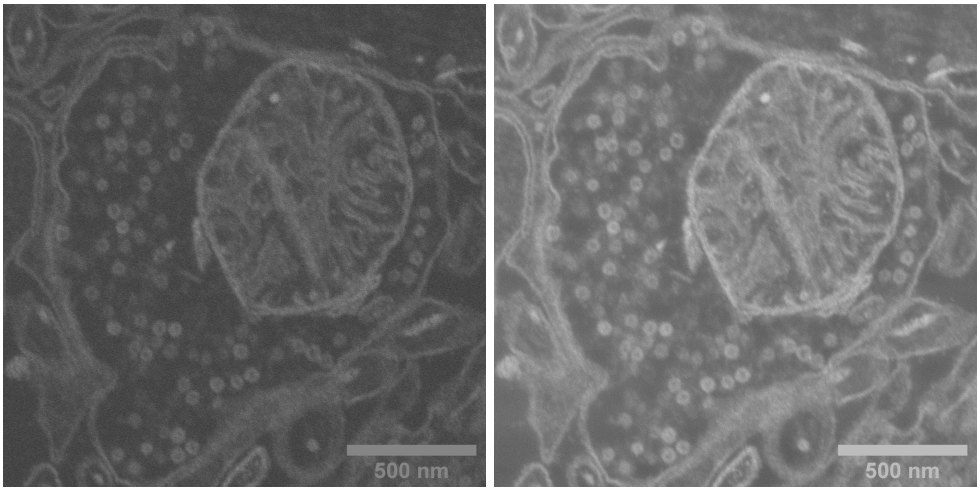


(a) (b)

Figure 3.16: (a) BSE and (b) transmission image of a mouse brain section, imaged at 15keV. The mouse brain section was on a TEM grid, which was stuck to an organic scintillator coated with Aluminum. After bleaching the scintillator with the electron beam, only a few luminescent centers are left, which creates the dark field transmission image.

If a higher-density structure is imaged, the electrons are scattered more in the sample, and thus, the interaction volume in the scintillator gets bigger. Thus, higher-density regions (more scattering) will generate more light in the scintillator than lower-density regions(less scattering), which leads to dark field imaging. This has to be performed at high energies, as the transmission coefficient of the sample is constant at a high value, which is at energies in figure 3.15 where the CNR is low.

This behavior, as was mentioned earlier, was observed in a bleached organic scintillator. In this experiment, the tissue section was on a TEM grid, stuck to the coated organic scintillator. This causes some distance between the sample and the scintillator, which is space for the electrons to spread out below the sample and create a larger interaction volume, enhancing dark field image contrast. An illustration of the possibility for dark-field imaging is shown in figure 3.16.

### 3.5.4. DOPANT CONCENTRATION INHOMOGENEITY

The scintillators used for transmission detection usually have a thickness of around 150-200μm . The scintillator, however, is a bulk crystal that is grown to sizes of about 100mm. During this growth, the Ce dopant has to diffuse to the lattice sites available in the crystal. If this process is not controlled precisely, local deviations in dopant concentration can cause local light output variations[19], [20].

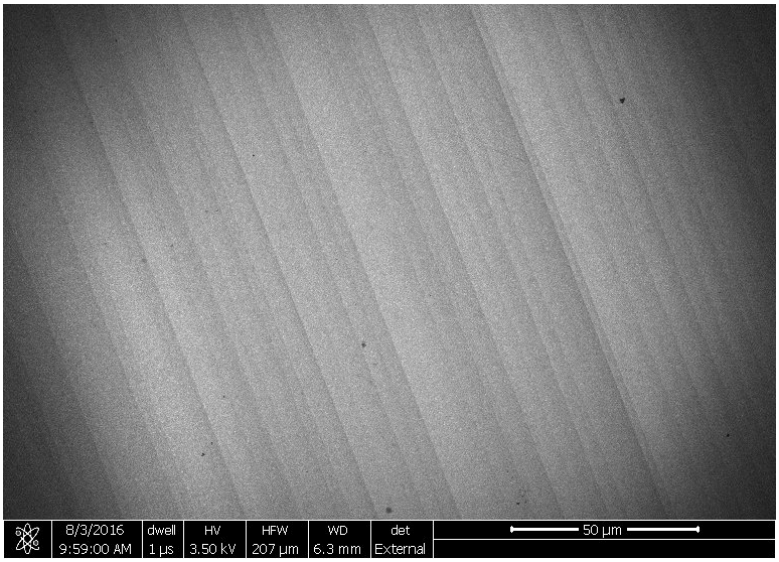


Figure 3.17: Transmission image of YAG:CE without a sample. The visible bands are due to local concentration variation of the Ce dopant.

Especially when the scintillator is saturated and all the centers are exited, this will show up as bands in the images. These bands are marked in figure 3.6 with yellow arrows. These bands are also observed when imaging the scintillator in a fluorescence microscope and extend in the same orientation throughout the scintillator. Figure 3.17 shows the effect on a larger scale, on an empty scintillator. The in-homogeneity is, in general, something that should be taken care of by the scintillator producer, as scintillators without the effect have been seen in some batches.

### 3.5.5. SATURATION REDUCTION

To reduce the saturation effect, a relatively thick coating of a low-density material can be used. When this is applied, the electron beam will scatter in the section and then have room to spread out in the coating material before entering the scintillator. This increases the electron's spot size on the scintillator and, thus, the interaction volume within it. Additionally, the electron beam will also have lost some of its energy. These two effects will cause less saturation.

## 3.6. SUMMARY AND CONCLUSION

### SCINTILLATOR

This chapter has described the considerations that have to be made for transmission detection of sections placed directly on top of scintillators. Here, we summarize the findings, including our decisions for implementation in MBSEM transmission detection. The possible detectors were described, and silicon photomultipliers (SiPM) were found to be the most suitable. The choice of scintillator is dependent on one's budget, but YAG:CE can be considered the optimal choice among scintillator materials here investigated by having a fairly low price and an emission spectrum that matches the detection spectrum of SiPMs. When a higher current is required, one should consider using faster scintillators to offset the saturation. This, however, will limit the minimum dwell time that is possible to 300ns, as otherwise, streaking artifacts will show up in the FFT. These artifacts might, however, not be apparent in the images or only show up for dwell times lower than 100nm as the pixel size is always (at least a factor 2) smaller than the probe size. In any case, the scintillators have to be polished to a very fine degree. Otherwise, scratches are visible in the images. The scintillator coating is limited to materials that do not show granularity after coating; this excludes most metals that are deposited by evaporation or sputter coating. In this work, it was found that only a sputtered Boron layer shows a non-granular layer and sputter-coated Molybdenum can be optimized to show very little to none. It has also been observed that the scintillators tend to saturate at small spot sizes and high currents, which reduces SNR and CNR. This effect does, however, allow dark-field imaging. The saturation effect can be reduced using a low-density, fairly thick coating layer. The thick coating gives room for the beam to spread out before hitting the scintillator.



### DETECTOR

From the analysis of the detectors, we find the following:

- Avalanche photodiodes: The input light power is too high for single avalanche photodiodes (see chapter 3)[1]–[4].
- Photodiodes: The input light power is too low to have a significant output current.
- PMT arrays: the anode current with the given input power is too high. The total input power would yield a total anode current of about 5mA, which is far above the rated specification of 0.1mA. The gain of the PMT could be reduced such that the anode current is lower, but it would operate outside the typical working range.

- Camera: the maximum framerate of the camera limits the dwell time to a minimum of 1µs at a very high cost[8].

The selection for the detector is, therefore, the silicon photomultiplier (SiPM). The SiPM has a high dynamic range and low noise. Chapter 2 shows multiple examples of acquisition with single-cell SiPMs.

Based on these considerations and findings, we conclude that finely polished YAG: CE with a Mo coating in the range of 5-25 nm, with B as a possible alternative, constitutes the optimal choice for signal generation and integration, with SiPMs as the final signal detector.

# BIBLIOGRAPHY


[1] G. E. S. Wolfe and C. M., "Avalanche photo-diodes", *United states patent*, 1976.

[2] S. Cova, M. Ghioni, A. Lacaita, C. Samori, and F. Zappa, "Avalanche photodiodes and quenching circuits for single-photon detection", *Applied Optics*, vol. 35, no. 12, p. 1956, 1996, ISSN: 0003-6935. DOI: 10.1364/ao.35.001956.

[3] D. Renker, "Geiger-mode avalanche photodiodes, history, properties and problems", *Nuclear Instruments and Methods in Physics Research, Section A: Accelerators, Spectrometers, Detectors and Associated Equipment*, vol. 567, no. 1 SPEC. ISS. Pp. 48–56, 2006, ISSN: 01689002. DOI: 10.1016/j.nima.2006.05.060.

[4] X. Sun and F. M. Davidson, "Photon Counting with Silicon Avalanche Photodiodes", *Journal of Lightwave Technology*, vol. 10, no. 8, pp. 1023–1032, 1992, ISSN: 15582213. DOI: 10.1109/50.156841.

[5] N. Liv, A. C. Zonnevylle, A. C. Narvaez, *et al.*, "Simultaneous correlative scanning electron and high-na fluorescence microscopy", *PloS one*, vol. 8, no. 2, e55707, 2013.

[6] Y. Ren and P. Kruit, "Transmission electron imaging in the Delft multibeam scanning electron microscope 1 Transmission electron imaging in the Delft multibeam scanning electron microscope 1", *Journal of Vacuum Science and Technology B*, vol. 34, 2016. DOI: 10.1116/1.4966216. [Online]. Available: http://dx.doi.org/10.1116/1.4966216.

[7] S. Rahangdale, P. Keijzer, and P. Kruit, "MBSEM image acquisition and image processing in LabView FPGA", in *International Conference on Systems, Signals, and Image Processing*, vol. 2016-June, 2016, pp. 5–8, ISBN: 9781467395557. DOI: 10.1109/IWSSIP.2016.7502728.

[8] T. Moynihan, *A Slo-Mo Camera With an Insanely High Frame Rate (And Price Tag)*, 2014. [Online]. Available: https://www.wired.com/2014/07/phantom-v2511-camera/ (visited on 10/01/2019).

[9] K. Sato, Y. Enomoto, and Y. Adachi, *MPPC technical note*, 2018.

[10] P. Schauer and J. Bok, "Book: Innovation possibilities of scintillation electron detector for SEM", in *IMC 2014*. [Online]. Available: http://www.microscopy.cz/html/1674.html.

[11] Crytur, *Scintillation materials*. [Online]. Available: https://www.crytur.cz/materials/ (visited on 09/01/2019).

[12] Shalomeo, *Scintillation Crystal Materials*. [Online]. Available: http://www.shalomeo.com/category/scintillation-crystal-materials-63.html (visited on 09/01/2019).

[13] B. Samuel, B. Aurélie, V. Bruno, *et al.*, "Defects Identification and Effects of Annealing on Lu2(1-x)Y2xSiO5 (LYSO) Single Crystals for Scintillation Application", *materials*, pp. 1224–1237, 2011. DOI: 10.3390/ma4071224.

[14] Eljen, *PLASTIC SCINTILLATOR PAINT EJ-296*, 2016.

[15] Newport. "Reflective objectives". (2021), [Online]. Available: https://www.newport.com/f/reflective-microscope-objectives (visited on 12/21/2021).

[16] Thorlabs. "Reflective objectives". (2021), [Online]. Available: https://www.thorlabs.com/newgrouppage9.cfm?objectgroup_id=6933 (visited on 12/21/2021).

[17] T. Templier, "MagC, magnetic collection of ultrathin sections for volumetric correlative light and electron microscopy", *eLife*, vol. 8, pp. 1–18, 2019, ISSN: 2050084X. DOI: 10.7554/eLife.45696.

[18] J. Krzywinski, A. Andrejczuk, R. Bionta, *et al.*, "Saturation of a ce: Y 3 al 5 o 12 scintillator response to ultra-short pulses of extreme ultraviolet soft x-ray and x-ray laser radiation", *Optical Materials Express*, vol. 7, no. 3, pp. 665–675, 2017.

[19] Z. Xia and A. Meijerink, "Ce3+-Doped garnet phosphors: Composition modification, luminescence properties and applications", *Chemical Society Reviews*, vol. 46, no. 1, pp. 275–299, 2017, ISSN: 14604744. DOI: 10.1039/c6cs00551a.

[20] M. Nikl, A. Yoshikawa, K. Kamada, *et al.*, "Development of LuAG-based scintillator crystals - A review", *Progress in Crystal Growth and Characterization of Materials*, vol. 59, no. 2, pp. 47–72, 2013, ISSN: 09608974. DOI: 10.1016/j.pcrysgrow.2013.02.001. [Online]. Available: http://dx.doi.org/10.1016/j.pcrysgrow.2013.02.001.

# 4

# HARDWARE FOR THE IMAGE ACQUISITION IN MULTI-BEAM STEM

## 4.1. INTRODUCTION

The previous chapters describe a STEM imaging method that can be applied in a multi-beam SEM. The single beam application of the method has different requirements from the multibeam application. This chapter is dedicated to investigating the hardware that is required for multi-beam imaging using the STEM imaging method as described in chapter 2 and chapter 3.

For a future commercial version of our MBSEM concept, the following characteristics were established :

- 8×8 electron beams
- 3.2μm pitch
- 500pA beam current
- 8nm spot size
- 4nm pixel size
- Optical STEM detection

For commercialization, a consortium between TU Delft, Delmic BV, Thermo Fisher Scientific, and Technolution was formed. This specification resulted from mutual discussions between the consortium members

The number of beams and beam current was selected mainly to reduce the effect of coulomb interactions on the probe size. More beamlet current or more beams would cause the beam to become larger than 8nm, as calculated by Stopka and Kruit [1]. The pitch size was selected such that the influence of stage overhead would be minimal while maintaining probe size.

The requirements for the optical stem detection system are as follows:

- A Parallel detector is required to obtain the signal from all 64 beams separately.
- The signal should stay on the detector
- Minimal crosstalk between detector signals
- Minimal throughput loss from ideal
- Homogeneous pixel size (no image distortions)
- The detector has to be readily available on the market (not an experimental detector).

As the beams would normally scan the area set by the pitch, the beam would scan from one detector to the other detector, making regular SEM image formation impossible. The scanning of the electron beam can be counteracted by an opposite scan movement in the light-optical system, which is called de-scanning. In total, three options were considered:

1. A high-speed camera (mainly CMOS) is a detector that acquires a frame for every dwelltime; de-scanning is not required.
2. One detector per beam, with a moving stage. In this case, de-scanning is also not required.
3. One detector per beam and a de-scan system.

The first selection criterion here is the detector, which will be considered in the next section.

## 4.2. DETECTOR SELECTION

Most of the detector selection criteria have been discussed in chapter 3. For the MBSEM, the SiPM detectors are selected. A benefit of SiPMs is that they can be arranged in an array and can thus be used for a square grid of beams. Multiple suppliers sell these arrays, among which are Hamamatsu, Ketek, and SenSL. For

the MBSEM, the C14047-5805 MPPC module was chosen. This module has a detector pitch of 3.2mm, which sets the requirement for an optical magnification of 1000×. The individual sensors of 3 × 3mm size provide an optimal combination of dynamic range and fill factor. The size of the the MPPC array determines the amount of avalanche photodiodes of a specific size that can be in one area. If this number is low, the dynamic range is low, and if this number is high, the dynamic range is higher. If the individual APDs get smaller, the fill factor of the sensor reduces as the circuitry of each APD requires relatively more space. These considerations fix the pitch at the detector to 3.2 mm. The magnification necessary to get to this pitch will ultimately determine the distance (and thus the angle) to be de-scanned.



## 4.3. CROSSTALK

As the light spot in the scintillator has a finite size and the objective lens below the sample is diffraction-limited, there will be some crosstalk on the detector.

In order to determine the exact amount of crosstalk, it is measured with a single beam system. In a multi-beam system, it is very tricky to decouple the effects of beams on the eventual signal detection. The measurements were therefore performed on an FEI Verios system equipped with an integrated light microscope (Delmic SECOM) [2], [3]. The imaging was performed using a NIKON plan apochromat 0.95NA 40x air objective. As a sample, a 200µm YAG:CE disk was used (obtained from Crytur, Brno), coated for conductivity, with 20nm of Al. The spot profile was measured for energies ranging from 1.5 to 30 keV. The images were acquired using an Andor Zyla 4.2 sCMOS camera with a pixel size of 6.5µm, giving an effective pixel size of 162.5nm.

To determine the crosstalk, a window of the size of the pitch was taken around the CL spot in the image, and all the pixel values within this window were added up. This gives the signal which would be collected without crosstalk (red in figure 4.1b). Now, the values of all the windows neighboring this center window and the center window are added up (blue in figure 4.1b). The ratio of these two values gives the amount of crosstalk to be expected in a multi-beam system. This is the amount of crosstalk for a fully surrounded beam from its eight neighboring beams, assuming that all beams have the same current. In a non-periodic sample, the images of the eight neighboring beams will be dissimilar, and they will mostly be visible as background noise, with the exception of high-contrast features.

The result of the measurement is shown in figure 4.2. Note that at a low pitch and high energies, the signal of the neighboring beams on a detector will be higher than the signal of the beam itself. At a pitch of 3.2 µm, the crosstalk is constant at around 7% for landing energies below 15keV. From figure 4.2, it

can be seen that there is, for each pitch size, energy below which the crosstalk is dominated by the diffraction limit (constant with energy) and above which the crosstalk is dominated by the interaction volume(increasing with energy). From a crosstalk perspective, it is best to keep the pitch as high as possible, but above 3µm , it does not have a lot of beneficial effects anymore.



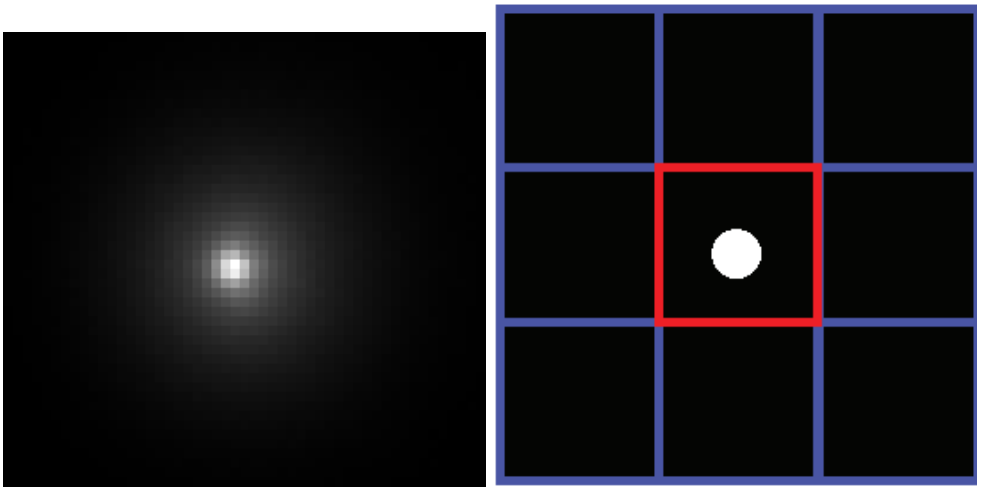

(a) (b)

Figure 4.1: (a) CL spot of a 30keV beam on yag:ce, acquired with a 40x 0.95NA objective lens and a 162.5nm effective pixel size. (b) Illustration of crosstalk calculation: the crosstalk is calculated by dividing the intensity of the total area by the intensity in the red area. Squares show detectors.

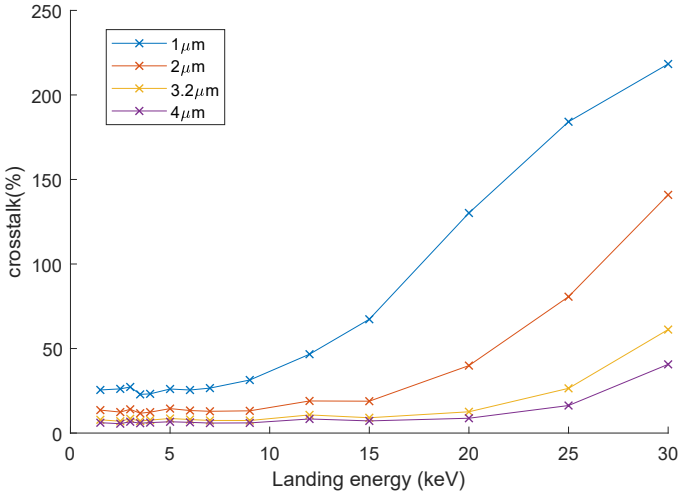


Figure 4.2: Measured crosstalk in a single cell as a function of Landing energy. The graph shows four different pitch settings.



## 4.4. STAGE

The second selection criterion is the sample stage. The requirements for the stage are dependent on the acquisition scheme. The first acquisition scheme that will be assessed is using a scanning stage. Here, there are also two options: the beams are completely stationary, and the stage scans the whole sample, or the beams scan a small part of the pitch, and the stage scans in the direction perpendicular to the beam scan.

The first of these options puts more stringent requirements on the stage, as the movement has to be very precise for the entire sample. In order not to be limited by stage settling times, the stage has to scan long distances at once, after which there should be no drift perpendicular to this scan. This option will not be further assessed as an investigation of the second option will show whether the first is possible. The next section will explain this second concept.

### 4.4.1. STAGE SCAN COMBINED WITH BEAM SCAN

A schematic overview of the acquisition is shown in figure 4.3. The grid is oriented with an angle of $\arcsin n^{-0.5}$, where $n$ is the number of beams with respect to the stage movement. In this case, the beams only scan a distance of $n^{-0.5}$ of the pitch in order to cover the full sample, resulting in only a very small movement on the detector. An eight-by-eight grid is oriented under an angle of 7.18° with

respect to the stage movement direction, and the beams scan 1/8 of the pitch, i.e., 400nm. To find the size of the light spot, we look at the radius of the first minimum in the airy pattern. In this calculation, it is assumed that the light from the scintillator is concentrated within an area smaller than the resolution of the optical microscope. The size of the light spot is given by :

$$r = 0.62 * \frac{\lambda}{\mathrm{NA}}$$

It is assumed that most of the light is contained within a radius that is twice that of the first minimum in the airy pattern. That radius here is 718nm, which at the selected pitch of 3.2 μm allows for the small movement of 882nm without any loss of signal.

Note here that the rotation of the grid is fixed by the magnetic lens action in the microscope, and in fact, the stage movement has to be oriented with respect to the electron beam grid. This does create stringent requirements for the stage, and to make sure that the movement error is only in one axis, the following stage concept is chosen: A rotation stage, a long stroke translation stage with limited precision, and a continuously moving stage. In this way, the direction of the stage move can be adjusted by the rotation stage, and the acquisition can be performed by only moving one axis.

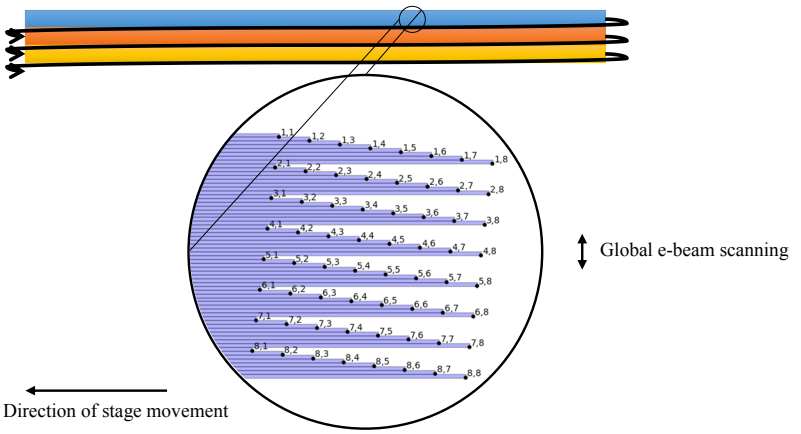


Figure 4.3: Schematic overview of acquisition with a moving stage.The different colored ribbons on top show the long stage moves that are made during the acquisition. After one of those moves (from left to right in this case), the stage is moved in a small step perpendicular. The inset in the circle shows the separate beams and the area that they scan while the stage moves.

#### SIGNAL LOSS AND CROSS-TALK

After stage scan alignment, the light spots created by each beam are aligned with the mppc detector array. To avoid having to correct for beam movement during a scan, the beams have to stay on their respective detector for the duration of acquisition for at least one tissue section but preferably more. The beams could move off the detector by two mechanisms: drift in the electron microscope or by magnetic fields generated by the stage. Drift in the light optical system is not considered here, as that depends on mechanical stability. In the ideal case, the stage is made out of nonmagnetic materials. Standard stages, however, are manufactured with stainless steel bearings, which might have some residual ferromagnetism. This ferromagnetism can lead to the beam moving as the bearings move. To quantify these two mechanisms of signal loss, measurements were performed.



Measurements were performed on the Nova Nanosem 200 in single-beam immersion mode and a Quanta FEG 200 in field-free mode at a landing energy of 5 keV. As a stage, a PILine ultrasonic piezo motor was used. The sample, a tin-ball resolution sample, was directly mounted to the polepiece, and the stage was moved underneath the sample in discrete steps. After every step, an image was recorded. For the drift measurement, the stage was kept in the same position, and an image was recorded every 20s. To analyze the data, a subpixel registration cross-correlation as described by Guizar-Sicairos, Thurman, and Fienup [4] was used. A total movement of approximately 1/4 of the pitch (800nm) can be accepted, which means a beam shift of at most 1/8 of the pitch on top of the scan movement. This is only considering crosstalk, as this movement also has to be compensated for by stitching.

An e-beam drift of 0.026 nm/s was measured, which means that an acquisition of 2.5 hours can take place before the drift is unacceptable. When assuming a dwell time of 1µs and sections of 1 $mm^2$, at least nine sections can be recorded in between realignments.

The result of the measurements on parasitic magnetic fields can be found in figure 4.4. As can be seen, the shift for the field-free system is minimal at 7 nm/mm of stage movement. The shift in the immersion field is, however, unacceptably high at 300 nm/mm of stage movement. Even hysteresis in the magnetization can be observed in the measurement. In the Apreo column, an immersion field will be present to focus the beams on the sample, and thus, stainless steel bearings in the stage are unacceptable. A switch to highly spherical ceramic bearings is therefore required.

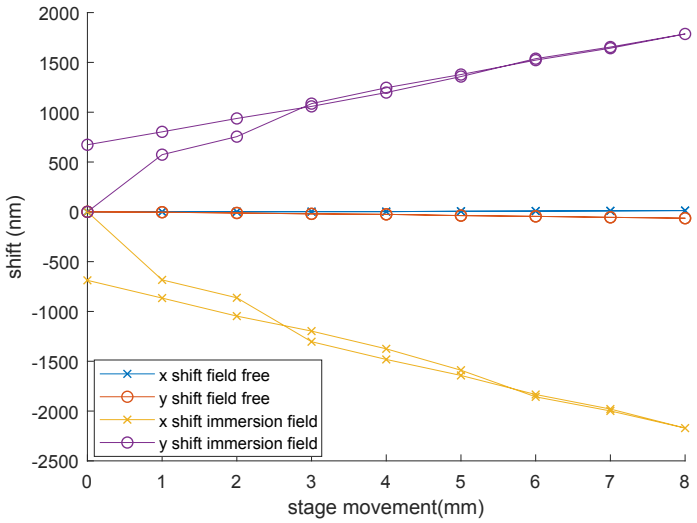


Figure 4.4: Beam drift as a function of stage movement for both immersion and field-free modes.

### THROUGHPUT LOSS

In the moving stage acquisition scheme, two mechanisms mainly influence the loss of throughput. Scan overhead, which is the fraction of a line scan that is not linear enough to use for acquisition, and grid distortions, i.e., any distortion in the grid that would result in extra overhead due to the need for more over-scan between the beams. In other words, any local deviation in pitch will result in the scan area of at least one beam being increased. If one beam is out of position, the beam next to it has to compensate for the distortion by overscanning the distance of the distortion. Because all beams have to be scanned simultaneously, this overhead is governed by the largest distance of any beam to the perfect grid. This is especially important for the moving stage acquisition scheme, as the beams only scan a small part of the pitch. A maximum deviation from the perfect grid of 100nm will cause an extra overhead of 25% .

### SCAN OVERHEAD

The choice of the column, as described at the beginning of this chapter, has a significant influence on the scan overhead. The Apreo column chosen has a magnetic scan system, meaning that the beam is scanned by means of magnetic scan coils. This scan system can be considered as an RL network, which, by definition, attenuates high-frequency components in an alternating current. The scan signal that is required has a sawtooth shape, and frequencies much higher than

the base scan frequency are present. These high frequencies will be filtered out by the self-induction of the scan coils.

In order to measure the scan overhead, we use the Nova Nanosem MBSEM in single-beam mode in combination with the SECOM platform. The main benefit of this measurement is that it is a direct measurement of the scan signal and does not require complex image interpretation. A scan signal is fed into the microscope through the external scan input and generated by a Rigol DG4102 arbitrary waveform generator with a sample rate of 100 Ms/s. To observe the scan, a bare scintillator was used, and the signal was recorded using a CMOS camera with a long exposure time so that only the full beam path was observable. The beam was scanned in the x and y direction with a saw tooth wave with half of a period phase shift between the two scans. This means that the overhead in one direction (the parameter of interest) is shown in the center of the scan in the other direction. The 400nm scan amplitude required is too small to observe using the optical system, but as the scanning system can be modeled as an RL circuit, the response is only dependent on the characteristic R/L time of the circuit and not the amplitude. An example of this is shown in figure 4.5, where the scan amplitude in the x direction is 80 µm and in the y direction 10 µm. As both scan directions have the same frequency, the overhead will be present in both directions. It is assumed that in the middle of the x-scan, the scan has become linear. The time per pixel is calculated from the 1khz scan, which is considered to be without overhead. This method is used to measure the overhead at high frequencies. The overhead, in this case, is defined as shown in equation (4.1).



$$O = \frac{t_{overhead}(s)}{T_{scan}(s)} \tag{4.1}$$

Here, $t_{overhead}$ is the time corresponding to the distance between the yellow lines as (for example) shown in figure 4.5b and $T_{scan}$ is the period of the scan corresponding to its frequency. A script was written to analyze these images. In this script, a linear fit is performed to the first part of the wave, and as soon as the difference between the linear fit and the output wave is bigger than 1 pixel, the scan is assumed to have become non-linear. An example of this analysis is shown infigure 4.6a. In this case, the scan is considered nonlinear between 16.2 ms and 23.3 ms for a total period of 7.1 ms; this translates into a scan overhead of close to 30 % . We can now analyze more frequencies and translate the frequency to a dwell time by assuming 100 pixels per line. The dwell time has to be adjusted, however, because, for a certain frequency, the dwell time will be reduced by a factor $1 - O$ as a smaller part of the scan has to fit 100 pixels. We can now analyze the overhead as a function of the adjusted dwell time, which is shown in figure 4.6b. Below a dwell time of 250ns, the measurement can be considered invalid because

no linear fit was possible to the camera image. A linear relationship between the overhead and scan coil frequency was found: $overhead = 6.128 \times 10^{-6} \times f$ with an $R^2$ of 0.97. The throughput as a function of the selected dwell time can be calculated, as well as the required frequency to achieve this dwell time. figure 4.7a shows that the maximum throughput reachable is around 396 Mpix/s at 100ns dwell time, and it is achieved with a scan coil frequency of 62 kHz.

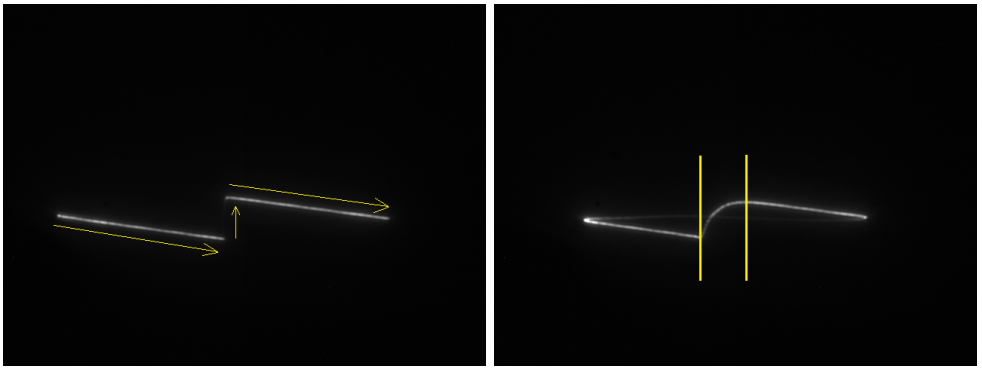

(a) (b)

Figure 4.5: (a) 1khz scan showing no overhead, the arrows showing the direction of the scan over the camera, and (b) 20khz scan showing the overhead at high scan frequencies with yellow lines.

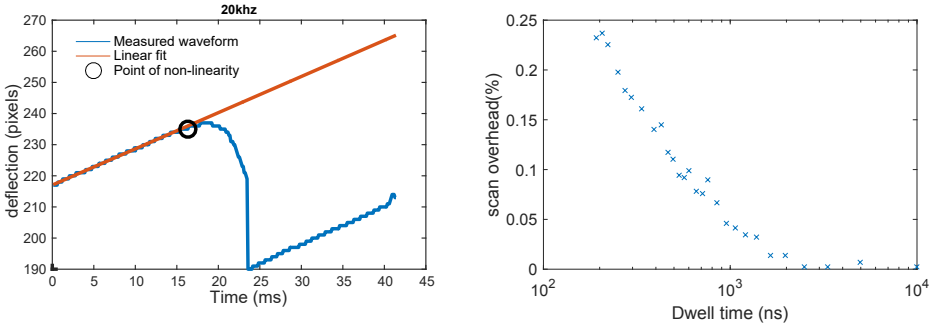


(a) (b)

Figure 4.6: (a)The measurement of a 50 kHz saw tooth wave. Red shows the linear fit, and the black circle shows the point from which the scan is considered non-linear. and (b)The scan overhead as a function of dwell time.

### SCAN COIL OVERHEAD REDUCTION

As this is a direct measurement of the dynamic response of the scan coils, it becomes possible to adjust the input signal such that pre-compensation of the scan

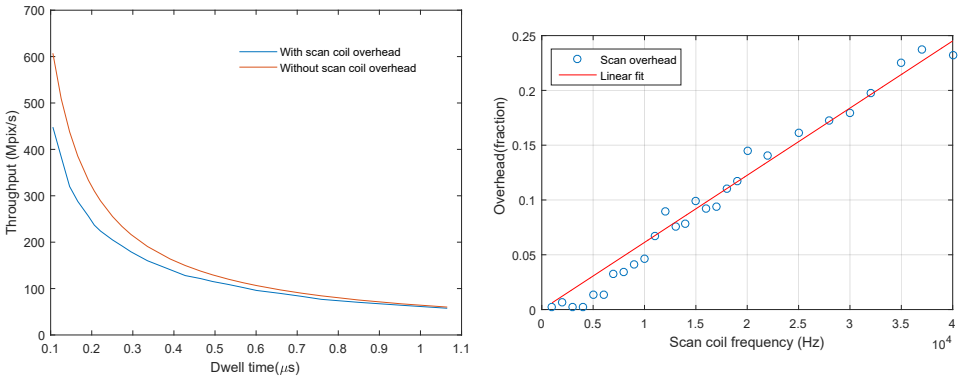


(a) (b)

Figure 4.7: (a) The throughput as a function of required dwell time with and without overhead and (b) overhead as a function of scan coil frequency.

coil self-induction is performed (feed-forward).

In order to predict the compensation, the scan coils are modeled as a simple RL circuit. The general transfer function of such a circuit is shown in equation (4.2). Where $O$ is the output, $I$ is the input, and $\tau$ is the time constant.

$$\frac{O}{I} = \frac{1}{1+\tau s} \tag{4.2}$$

The time constant can be found by changing the y scan of the beam from a saw tooth to a step. This will show the step response of the RL circuit, and the time constant found is 1.5ms. Using these values to simulate the circuit using the 'lsim' function in Matlab, the result is shown in figure 4.9 for 80kHz. This image illustrates that as the overhead approaches 50 % , it is impossible to precisely measure the overhead as 50 percent of the x and y scan is lost, and none of the full scan is visible. The most important conclusion when assessing these images qualitatively is that the model seems to be fitting the data quite well. The 80 kHz scan in both the measurement and the simulation shows a similar slope and amplitude.

Using this model, it can be predicted what kind of signal is needed to precompensate for the scan coil self-induction. The signal to be used will ramp like in a normal sawtooth but then severely undercut the first point and stay fixed there for a while. This input waveform is shown in figure 4.10a for a frequency of 120 kHz. In order to make this type of waveform compensate for even higher frequency self-inductance, only the duration of the lower drop has to be changed. An even lower voltage in the drop would reduce the time to stay there but re-

quires more dynamic range than was available in the experiments performed for this investigation (limited by the arbitrary waveform generator). In the case of the MBSEM and the much smaller scan distance, the dynamic range will be improved. Using the input wave as described, the output as shown in figure 4.10b is obtained from the simulation. It shows that at even high frequencies, this method allows for full compensation of the throughput when considering the simple RL model for the scan coils. Experimentally, this method will not directly translate as the model is oversimplified. The scan rotation has to be set, so more coils need to be used than the one in our simulation, which both have to be adjusted accordingly.



As it is experimentally fairly time-consuming to compensate the scan signal, for proof of concept, an 80 kHz and a 120 kHz scan were compensated. The same strategy as shown in figure 4.10a was attempted but gave an unexpected artifact, which had to be compensated for by changing the wave to what is shown in figure 4.11a. This compensates for the observed artifact and compensates the self-induction. The output wave is shown in figure 4.11, in which an overhead of 25% is measured instead of the 75% expected before compensation. Note that the slope is not completely constant, which will cause a slight but constant image distortion. Not shown in this chapter is an almost completely compensated 80kHz scan (5% overhead). From these numbers, it is assumed that the overhead at 90kHz can be compensated to around 10% . This increases the throughput at 100ns from 396Mpix/s to 576Mpix/s. For dwell times above 120ns, there is very little (<5 % ) overhead caused by the scan coil self-inductance.

Another solution would be to use electrostatic scanning. This would reduce the overhead considerably as the response time is almost instant. Building electrostatic scanning into any microscope for the purpose of the acquisition scheme would be fairly easy, as the beam only has to scan a small distance, requiring small field strengths. For instance, to scan a 5keV beam, 400nm on the sample, with the scanning plates of 1mm in height under the pole piece at a distance 4mm from the sample. Then, according to equation (4.3)($\epsilon$ is the deflection angle, E is the field strength, and K is the energy of the electron), only a field strength of 500V/m would be required. Thus, for a gap of 10mm in between the plates, this is just a potential difference of 5V between the plates[5]. This does require quite some engineering as these systems are not available as is. It will, therefore, not be considered for our prototype.

$$\epsilon = \frac{eh}{k} E_x \tag{4.3}$$

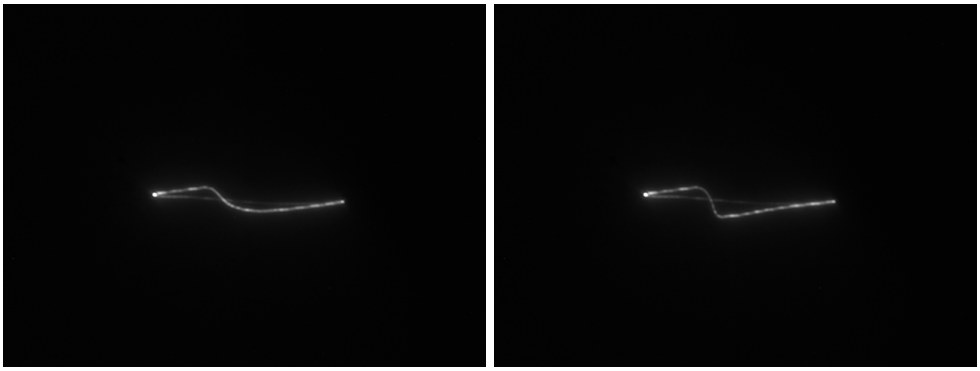

(a) (b)



Figure 4.8: (a) The waveform of figure 4.8a at 40khz, showing clearly the overhead, which is (b) compensated by pre-compensating for scan coil overhead.

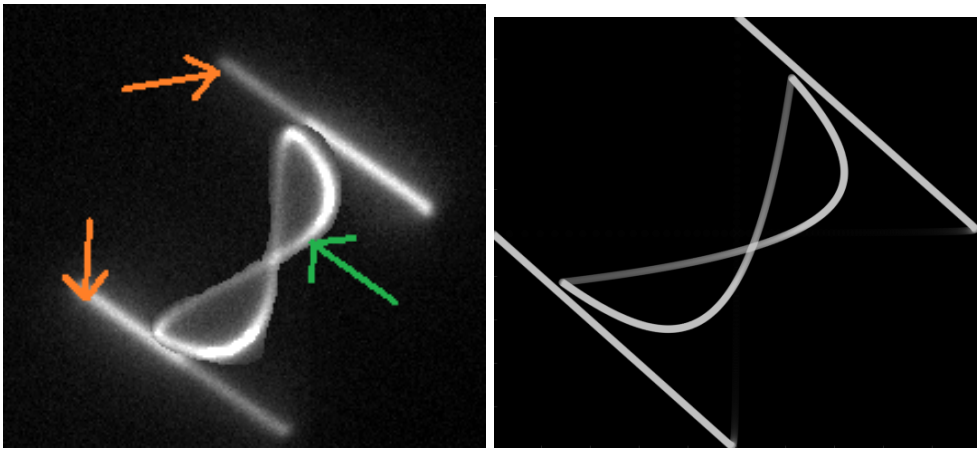

(a) (b)

Figure 4.9: (a)Measurement of a 1khz (orange arrow) scan and an 80 kHz (green arrow) scan merged in the same frame, which fits well to the (b) simulated image of the same scans.

### GRID DISTORTION

As was discussed before, any beam that is not on the perfect grid will increase the length of the scan line to compensate and make neighboring beams overlap. For instance, a beam that is 20nm out of position will cause a $20/250 \approx 10$ % overhead. Measurements on the NovaNanoSEM show large grid distortions of up to 200nm in an 8x8 grid. This can result in large consequences for imaging with a moving stage. This distortion is, however, very much dependent on the excitation of the stigmator and can be reduced by adding a second stigmator to the

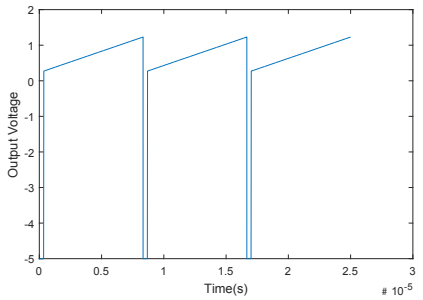


(a)

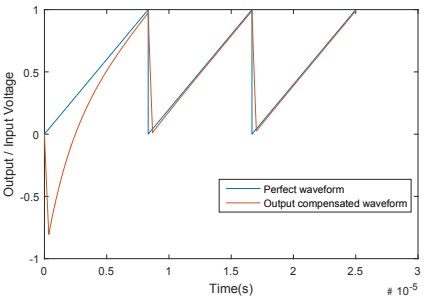


(b)



Figure 4.10: (a)Input of the scan coils, which compensated for the self-induction at a frequency of 120 kHz. (b)Ideal signal and simulated coil output.

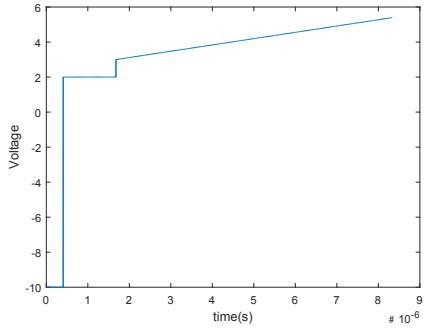


(a)

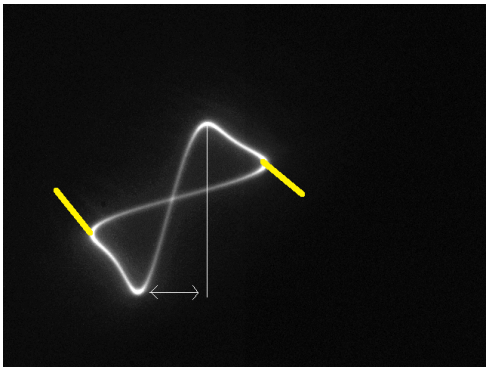

(b)

Figure 4.11: (a)The signal used to compensate a 120 kHz scan and (b) the output when using this signal. The yellow lines show the part of the measurement that is lost in the perpendicular scan; the white arrow shows the scan overhead region, which is 25% of the total scan.

system. One of the stigmators compensates for beam stigmation (in a common crossover) and one for grid stigmation.

### PIXEL HOMOGENEITY

In regular SEM imaging, the pixels are as square as possible throughout the whole image (or homogeneous magnification in x and y). Things that can usually influence the squareness of pixels are drift in the stage and a non-linear beam scan. In the case of the moving stage acquisition scheme, the factor most likely to make the pixels non-square is a stage that does not move at a constant speed. If the frequency at which this speed changes is high (higher than half the line frequency),

this will cause the resolution to deteriorate, whereas a low frequency will cause image distortions (smaller than double the line frequency). After significant development, the peak-to-peak error of the stage was still an order of magnitude larger than the pixel size. The measurement of the stage position error is shown in figure 4.12. It shows that all large errors occur at frequencies much lower than the scan frequency (15 kHz at 1µs dwell time).

Even though the resolution is not degraded by the error in the stage position, severe image distortion is to be expected. Even if the distortion is accepted as an unavoidable artifact, stitching between two full scan ribbons is made difficult by the random nature of the stage speed variation.



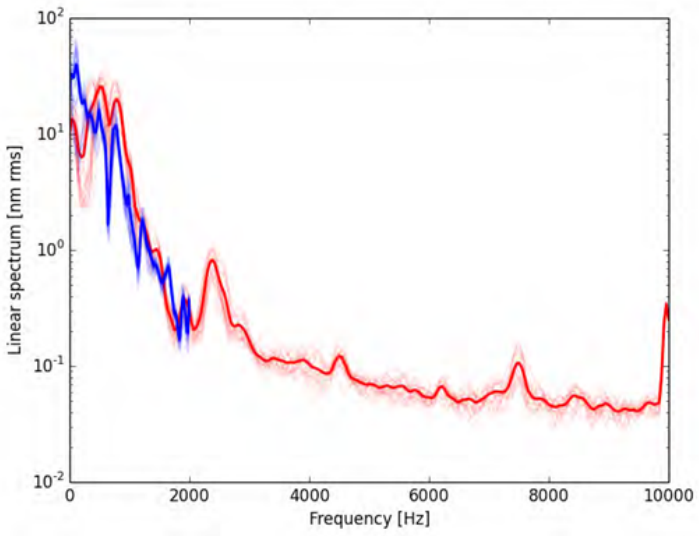


Figure 4.12: Measurement of the stage position error, showing the frequency spectrum of the error.

Due to the low-frequency nature of the position error, the electron beam does cover the whole sample. By measuring the position of the stage at any point in time, the pixels can be put in the right location, and the dwell time will vary from pixel to pixel. This requires that the stage position is known at any moment in time, for instance, by interferometer measurements. By having a signal, electron beam position, and stage position at any moment, an image can always be reconstructed.

#### STATIONARY BEAMS AND STAGE SCAN

In this acquisition scheme, the beams would scan one long row of pixels in x (for instance, a whole section), after which the stage is moved one column in y. These

two columns have to be aligned within 4nm, which is impossible with the stage performance as shown in figure 4.12.

### 4.4.2. BEAM SCAN AND OPTICAL DE-SCAN

In the case of beam scan and optical de-scan, there are two main mechanisms that can reduce throughput, that is, scan coil overhead and stage settling time.

The scan coil overhead was measured in section 4.4.1. Because the amount of pixels in a row is eight times higher in the de-scan case, the maximum frequency is eight times lower at the minimum dwell time. It has been shown that, in this case, the scan coil overhead can be compensated almost completely. The overhead caused by the stage move is due to the inertia of the stage, which causes it to overshoot; this is the so-called settling time of the stage. In the next section, this will be investigated further.

The stage requirements for a beam scan and optical de-scan are less stringent than for a beam scan and stage scan. The main requirement for the stage is that the settling time is low, as this could easily become the leading factor in the ultimate throughput of the system.

#### STAGE OVERHEAD

In order to investigate the impact of the stage overhead, first, the settling time was measured. The settling time is defined as the time the stage takes to be stationary within a pixel size (4nm). This measurement was performed using two methods. The first uses the data from the optical ruler, which has a time resolution of 100μs and a spatial resolution of 100nm. The stage was asked to make a 15μm step. The stage move was performed four times at 5 mm/s, 0.75 mm/s and 0.5 mm/s. An example of the measurement is shown in figure 4.13. From this data, it was found that a slower movement speed is beneficial for the settling time of the stage. The average settling time for the stage was found to be 40ms,51ms, and 78ms for the 0.5mm/s, 0.75mm/s, and 5mm/s stage speeds, respectively. This reduced settling time is caused by the lower inertia of the stage at lower speeds.

Due to the limited resolution of the optical ruler, SEM images were used to verify the result. An image was acquired, and during the acquisition, the stage was moved to a new position; an example of this can be found in figure 4.14. The dwell time was set to 800ns and the horizontal width to 1024 pixels. The line duration now is 0.819ms. By measuring the number of lines before the stage is completely stable, the settling time can be calculated. In this case, the settling time was found to be 82ms, which is significantly higher than was found using the ruler. This is caused by the position error being smaller than the 100nm resolution of the ruler. Note that this measurement was done on a single stage with

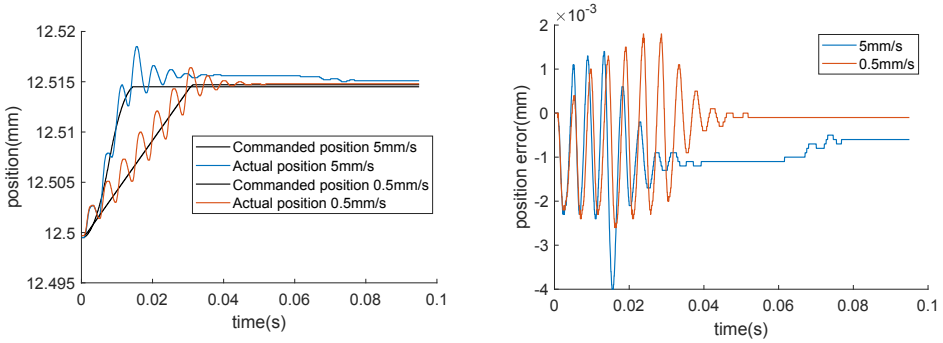


(a) (b)

Figure 4.13: (a) Example of a measurement of the settling time of the stage at two different movement speeds. (b) Position error of the stage during a move, showing clearly the settling time.

no optimization for settling time. It does, however, provide us with a settling time that can be reasonably expected.

Assuming a settling time of 100ms, the throughput loss can be seen in figure 4.15a. The maximum throughput, at 100ns dwell-time, is reduced from 640 Mpix/s to 128 Mpix/s. One method to reduce the effect of the stage overhead is to increase the pitch of the beams so that one field takes longer to acquire and the impact of the stage overhead is less. For this reason, it was decided later on in the project to change the pitch from 2µm to 3.2µm, which could be done without loss in resolution. The effect of this change is shown in figure figure 4.15b, the maximum throughput increases to 250 Mpix/s.

#### STAGE OVERHEAD REDUCTION BY MULTI-FIELD SCANNING

To reduce the effect of the stage settling time, we suggest the following scanning procedure. Instead of moving the stage to a new position every time a full field is imaged, the stage will now only move when 4 or 9 fields are imaged. The other movements are replaced by an electron beam shift, which will then be descanned by the de-scan unit. By this method, there is a decrease in the stage overhead by a factor of at least three and, at most, 8. The settling time of both the de-scan system and the electron beam is much lower than that of the stage, and throughput is thus increased. The effect of the multi-field scanning approach is shown in figure 4.15. The maximum throughput can now be increased from 128Mpix/s to 428Mpix/s and from 250 Mpix/s to 540 Mpix/s at a pitch of 2µm and 3.2µm, respectively.

The amount of fields in the multi-field that is possible is limited by the area in which the resolution is still constant. Thermo Fischer calculated this to be 3×3

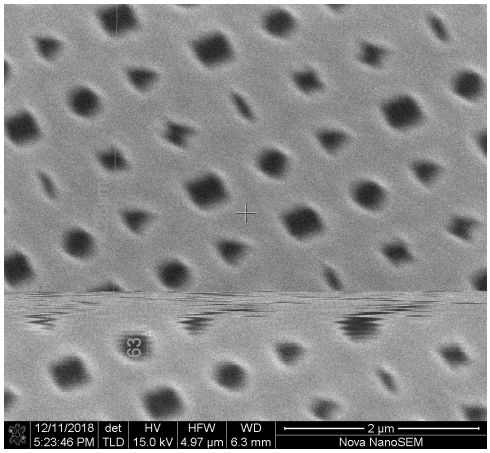


Figure 4.14: Image used for the measurement of stage settling time. Images were acquired with a line time of 0.819ms. The image shows a top part in which there was normal imaging. During the imaging, the stage is moved in one direction, shown by a discontinuity in the image. The move is relatively short, and after the move, the stage has to settle, which is shown by wiggly lines in the image. After settling, normal imaging at the new stage location.

fields.

Another way of reducing the effect of stage settling time is to measure the position of the stage while it is settling. Using a feed-forward system and a good model of the stage, the electron beam position can be actively compensated to account for the stage settling behavior. This can only be done to the extent that the beams do not move off their detector (1/4 of the pitch).

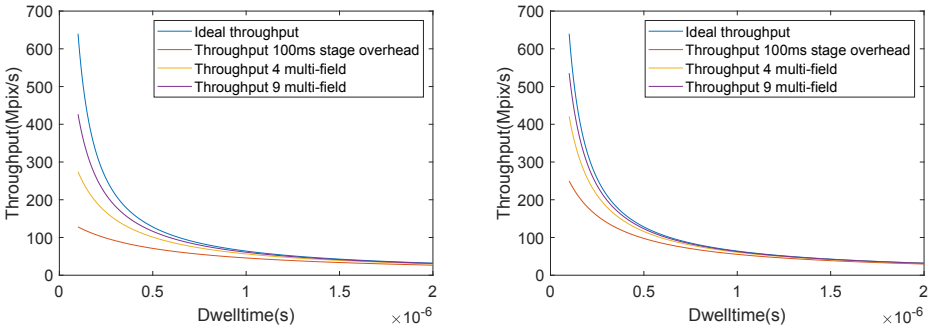


Figure 4.15: (Graph showing the ideal throughput of a multi-beam system and the loss in throughput due to stage settling time. The effect of changing to a multi-field acquisition approach is also displayed for (a) a pitch of 2µm and (b) 3.2µm.

## 4.5. LIGHT OPTICS AND DE-SCAN

This section will describe the requirements for the light optical path and the de-scan and show performance measurements on a de-scan system.

### 4.5.1. OPTICS

#### OPTICAL PATH

In order to image the grid of light spots on the detector, an optical magnification of 3.2/3200 = 1000× is required. This can be achieved by having a two-step magnification system: the first is the 40× magnification that is created by the objective lens and a 200mm tube lens. The second step is a 25× magnification, which can be achieved by, for instance, a combination of an 8mm lens and a 200mm lens.

In order to de-scan the signal, a de-scan element has to be placed in the optical path. This element is a reflective element that de-scans the signal by adjusting the angle of the light beam in the optical path. There are multiple options for this de-scan element, and the selection criteria are listed below.

The following parameters eventually determine the choice of the de-scan system:

- Clear aperture
- Minimum and maximum deflection angle
- Deflection accuracy and repeatability
- Maximum operating frequency at the maximum deflection angle

- Availability and price

The first four parameters are dependent on the location of the de-scan element in the light path (A drawing of the optical system will be shown in chapter 5: figure 5.1b). In this work, we will assume that the de-scan element is in the infinity-corrected light path, as that is where there is a lot of space, and the location is not of importance for the de-scan angle. There will, however, be some light loss due to this location, which will not be considered in this chapter. In order to have a high light collection efficiency, a high NA objective is required. The highest NA air objectives available have an NA of 0.95 and 40x or 60x magnifications. These objectives are aberration-corrected and will thus form a spot on the detector, which is diffraction-limited. From now on, a 40x objective will be assumed. Firstly, it is important to calculate the effective focal length of the objective. This is given by the magnification and the tube lens focal length. In the case of the 40× and a 200mm tube lens, the focal length is 5mm.



The required clear aperture of the de-scanner is at least the same as the beam size when it leaves the objective and, thus, the size of the objective pupil aperture. For a high NA objective, this size is given by 2×f×NA. This gives a minimum required aperture of the de-scanner of 9.5mm. Any aperture smaller than this will cause a significant loss of signal.

The focal length and the beam pitch give the deflection angle required. For a pitch of 2μm the de-scan for small angles is now given by pitch/f = 0.0032/5 = 0.64 mrad. The accuracy of this angle has the same criterion as in the case of the moving stage acquisition, which was calculated to be approximately 1/4 of the pitch (section 4.4.1). Because the translation is linear with the angle, this yields a minimum accuracy of 0.16 mrad.

### 4.5.2. DE-SCAN

First, we will discuss four options for de-scanning the beam and the apparent limitations of these methods. These four options are Electro and acousto optical scanners, deformable mirrors, Polygonal scanners, and galvanometer scanners.

#### ELECTRON AND ACOUSTO OPTICAL SCANNERS

Both electro and acousto optical scanners work by changing the refractive index of a material. The data presented here is taken from Römer and Bechtold [6], who gives a good overview of laser scanners. In electro-optical scanners, an electric field is applied across a material that perturbs the material such that the refractive index changes. By varying this voltage over time, the beam can be scanned. The main limitation is that the maximum deflection angle is inversely proportional to the third power of the aperture size and scales with the square of the applied voltage. The maximum de-scan angles that can be obtained are fairly small,

and for the largest aperture size of 2mm, the maximum deflection is 1mrad. In general, electro-optical scanners are very fast (response time of a few microseconds) but are very limited in aperture size and maximum deflection angle.

In acousto optical scanners, the beam is deflected by an optical grating. This grating is created by inserting acoustic traveling waves of typically 80 MHz to 1 GHz) in the material, which creates periodic pockets of lower and higher density. This periodic structure diffracts the light, and the first-order diffraction spot is the deflected beam. This diffraction process, however, does cause a loss in light of up to 60%. The opening aperture is up to 10 mm, and the maximum deflection angle is 50mrad. The response time is similar to that of electro-optical scanners.

Both the scanners presented here, even though possibilities do exist for use as a de-scan unit, are mostly in use for laser steering applications and other specialized fields. This means they are expensive and hard to obtain.



#### DEFORMABLE MIRROR

Deformable mirrors are usually not used as beam steering devices but as aberration and distortion correctors by locally changing the optical path length. The most common type is built up of a few hundred separately movable sections that are capacitively actuated. These deformable mirrors can be very fast, with response times in the order of a few microseconds. The total stroke of the aperture of deformable mirrors is, however, limited. Recently, a new design was released that does suit our application[7]. The total stroke is 5.5μm, and the aperture size is 10.35mm, which yields a total deflection angle of 1.1mrad. These specifications leave deformable mirrors as an open option for the de-scan system in the MBSEM.

#### POLYGONAL MIRROR

A polygonal mirror scanner is a spinning wheel with a faceted surface. For a scan of 0.4mrad, the mirror has to have $2\pi/0.4 \times 10^{-3} = 15708$ facets. By moving the mirror further down the optical path, the de-scan angle can be increased, but the number of facets will always be in the order of hundreds. Each facet has to have a length of at least 20mm, which, in this case, would create a mirror wheel with a radius of 50m. Calculating the other way around, we can say that a wheel with a radius of 5cm is still acceptable in the optical setup; the deflection angle, in this case, is 0.4rad. In order to use polygonal scanners, the optical setup has to be changed to accommodate this. Perhaps the biggest problem with polygonal scanners is that the signal cannot be used in the time that the beam moves from one facet to the other facet; this causes an overhead of 50% . Note that another less common method would be a refractive wheel, which would have the same issues.

#### GALVANOMETER SCANNERS

The last option that will be discussed here is that of galvanometer scanners. These scanners are the most common in scanning microscopes, the most famous of which is the confocal laser scanning microscope. In a galvanometer, the mirror is connected to a rotor. This rotor has either a magnet connected and coils around it or the other way around. By running a current through the coils, the mirror is rotated. The aperture of a galvanometer scanner can be of any size, but heavier, larger mirrors will change the behavior of the system. This scanner usually has a resolution that is in the order of 10 micro radians, and the full deflection at high frequencies is around 1mrad [8]. The main drawback is that the inertia of the whole assembly limits the maximum operating frequency. For example, the galvanometer scanner that will be used in the rest of this work is limited to a maximum frequency of 1kHz (sine), which would limit the minimum dwell time to 2 μs. We will, however, show in this chapter that this maximum frequency can be stretched to a large degree.



### 4.5.3. GALVANOMETER PERFORMANCE

The Thorlabs GVS212(/M) large beam diameter dual axis scanning galvo system is available at TU Delft. This galvo system has a small angle (0.4°) bandwidth of 1kHz. As each beam will scan its pitch, 3.2μm , and the pixels are 4nm in size, this bandwidth limits the dwell time to 1μs and the throughput of the system to 64 Mpix/s. Here, it will be investigated whether this frequency can be increased and to what extent this can be done. Note that for regular SEM scanning, a sawtooth waveform has to be used as input. For a dwell time of 100ns and a pitch of 3.2μm, the frequency of the waveform is 12.5kHz.

#### EXPERIMENTAL SETUP

In the multi-beam SEM, the beams should be de-scanned in the detector plane over the full pitch of the detectors, 3.2 mm. With the magnification as is, this means that the mirrors, which will be placed in-between the objective lens and the tube lens, have to move 0.4mrad (0.02 °) over the full scan range. The galvo's were set to a sensitivity of 1 °/V which means that an input of a 23mV peak-to-peak waveform is needed for a full de-scan. In this investigation, the input for the galvo mirrors was generated by a high bandwidth arbitrary waveform generator. The actual position and the required position can be measured through a readback that is provided by the driver circuit of the galvo mirrors. The input was chosen such that the output was always 0.1 °, as 0.02° gives a very small amplitude on the oscilloscope.

#### RESULTS

#### DYNAMIC RESPONSE

In a regular SEM system, the beam is scanned with a sawtooth waveform. This means that the beam scans from left to right and, when it arrives at the end of this line, jumps back to the beginning with a small displacement downward. When inputting a 1.5kHz sawtooth waveform into the galvo, the higher frequency components all get filtered out, and the output is a sine wave. This is shown in figure 4.16a. In this figure, something else can also be seen; that is, the amplitude of the output waveform is severely reduced by the system, and thus, the input has to be adjusted to compensate. At 5kHz, the output waveform is severely deteriorated and unusable for a de-scan(figure 4.16b).
As the high-frequency components seem to be filtered out, it might be beneficial to change to a bidirectional "serpentine" scan mode. In this case, the scan does not continue at the beginning of the next line after finishing the previous one but starts at the end of the next line. In this method, the high-frequency components associated with the sharp drop in the sawtooth are lost, and the input waveform becomes a triangle waveform. Another benefit is that, when using serpentine scanning, the maximum frequency is halved. When inputting a triangle waveform that is needed for serpentine scanning, the output at 1kHz is immediately a sine waveform. As the high frequencies are filtered out anyway, a sine waveform can be used as an input to start with. The sine waveform is at most only 6% different from a triangle waveform, which is easily within the 25% we have calculated to be acceptable as a position error. For the next measurements, a sine waveform was used as the input signal for the mirrors. A triangle waveform was fit to the output signal, and the maximum error between the two was calculated. The result is shown in figure 4.17. It shows that in the case of bi-directional scanning, the minimum dwelltime is 106ns when accepting a 25% de-scan error. Note that a de-scan error of 25% does not mean an overhead of 25% . In order to reduce the maximum error to below 10% at high frequencies, a small overhead might be enough.

#### AMPLITUDE ATTENUATION

As noted in the previous section and shown in figure 4.16a, the amplitude of the output is severely attenuated compared to the input. Thus, for every dwell time, the amplitude of the input signal to the galvo mirror has to be adjusted. Figure 4.18a shows the attenuation of the amplitude. For the lowest possible dwell time with an acceptable error (106ns), the peak-to-peak voltage of the input waveform has to be increased by a factor of 100 to get the correct amplitude. In this case, the angle that is required for the de-scan is 3.5V peak-to-peak. As this can be calibrated very precisely and the voltages are not extreme, this should give no issues for the de-scan with galvanometer mirrors.

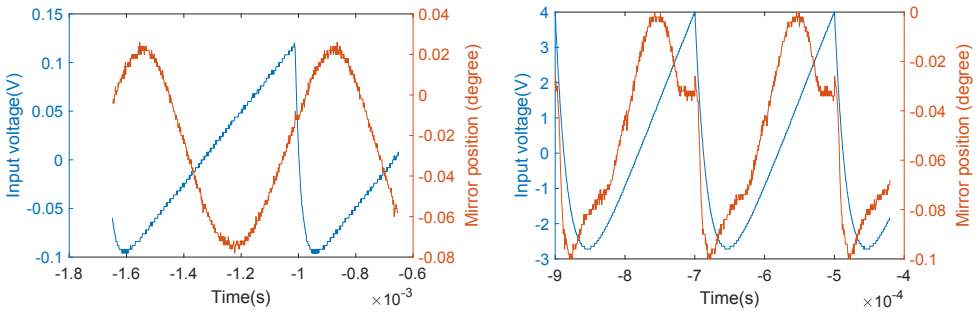


(a) (b)

Figure 4.16: The mirror position sensor output for the input of a sawtooth waveform with a frequency of (a) 1.5kHz and (b) 5 kHz. Blue lines show the input voltage to the system, and the red lines show the measured mirror position. The 7V voltage sweep in (b) was supposed to lead to a 7 ° change in mirror position. Thus, it can be seen that the output amplitude is considerably reduced.

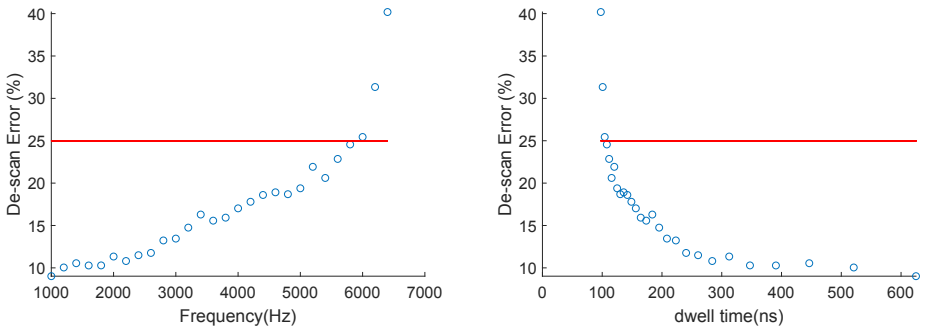


(a) (b)

Figure 4.17: Graphs showing the maximum de-scan error of the galvanometer mirrors as a function of (a) frequency and (b) dwell time.

### PHASE SHIFT

Due to the galvo mirror system being a mass-spring system, a phase shift between the input and the output will occur at higher frequencies. The phase shift is calculated from fits to the input and output signals of the mirrors. In figure 4.18b, the phase shift is shown as a function of the scan frequency. At a very long dwell time, the phase shift is zero, which is not shown in the graph. This phase shift can also be easily calibrated, as it is fixed for this particular system.

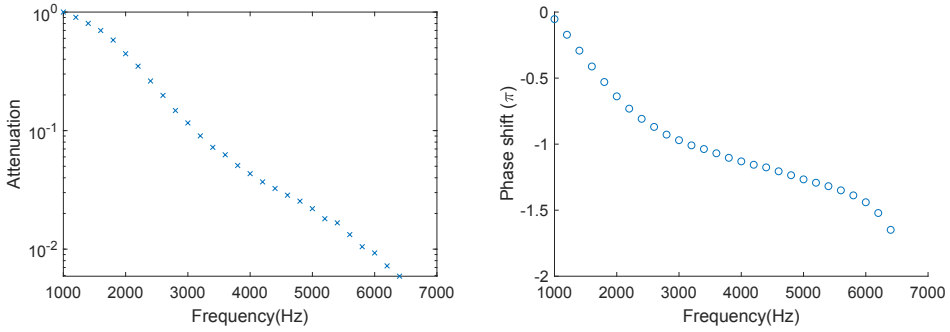


(a) (b)

Figure 4.18: The (a) amplitude attenuation and (b) phase shift of the Thorlabs galvanometer mirrors.

### 4.5.4. SCAN PATTERN

In traditional SEM imaging, a sawtooth wave is used for both the x and y direction of the scan, which provides a uniform cover of the beam over the surface it scans. The dynamic response shown in the previous sections, however, forces the use of a bi-directional scan for scan frequencies higher than 1kHz(2 µs dwell time). A benefit of the bidirectional scan is that one period now contains two lines in the image, and the maximum needed frequency is halved (10kHz vs. 20kHz). When the bidirectional scan is introduced in the x direction, and the y direction is still kept as a ramp, the coverage of the scan is no longer uniform, as illustrated in figure 4.19. At the left and right edges of the image, this will cause half of the sample not to be scanned and the other half to be scanned twice. This will show up in the image as a fairly clear, though hard-to-quantify artifact. To understand the full impact on the image, a simulation of the scan is performed on a previously acquired SEM image; the result is shown in figure 4.20. For the simulation, an image with a pixel resolution of 0.5nm was used. The image was resampled with a beam of 8nm FW50 in both unidirectional scanning and bidirectional scanning. The image shows the effect very clearly; at the vertical edges of the image, two pixels get merged in the vertical direction only, creating a more pixelated look. The way to mitigate this effect is to change the vertical beam scan from a continuous ramp to a stepped ramp, thus creating the scan pattern in figure 4.19.

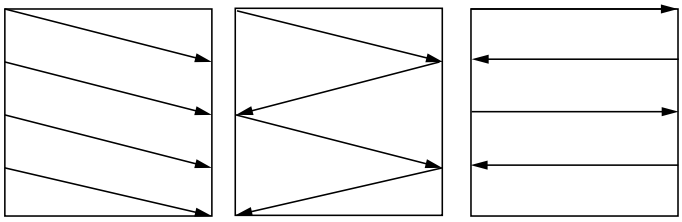

Figure 4.19: The various scan patterns to be considered. (left)Unidirectional scan as is regularly used in SEM imaging (middle) bidirectional scan with a ramp in the y-direction, showing nonuniform sample coverage (right) bidirectional scan with a stepped ramp in the y-direction and uniform sample coverage.



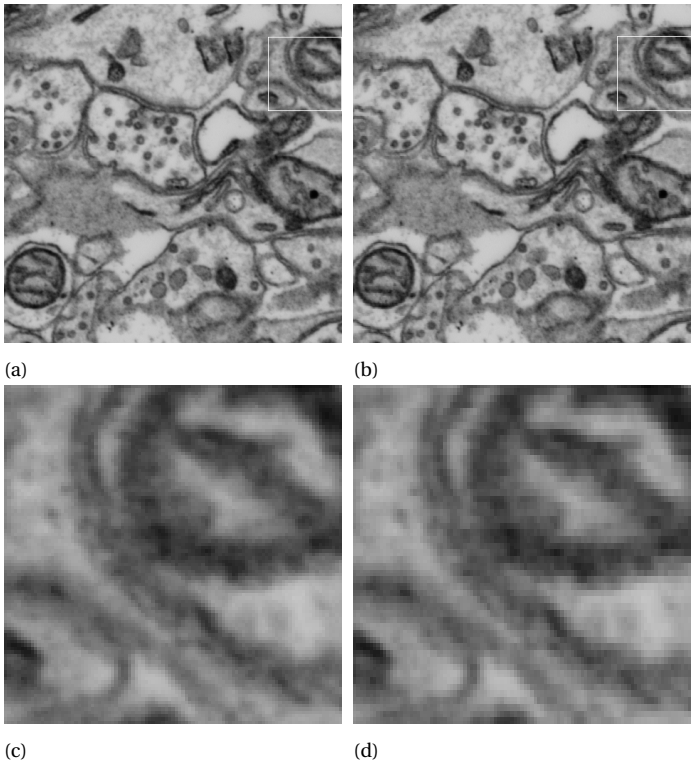


Figure 4.20: (a,c) Simulation of unidirectional and (b,d) bidirectional imaging, illustrating the pixelation effect due to inhomogeneous surface coverage of the bidirectional scan. (c,d) show the boxed areas at the vertical edge of the images in (a,b), where the pixelation effect is immediately evident. The horizontal field width of the images is 2μ.

## 4.6. SUMMARY AND CONCLUSIONS

In this chapter, two different acquisition strategies were discussed for the MB-SEM. Both strategies take care of the fact that the beams will not be stationary on the detector when the full pitch is scanned.

The first strategy discussed has the beams scan 1/8 of the pitch and the stage moving continuously in the direction perpendicular to the scan direction. The main advantages of this strategy are that there is hardly any stage overhead and no separate de-scanning of the signal is required. Disadvantages are that it requires a very stable stage and a high scan frequency. From measurements, it was found that by pre-compensating the scan signal, the overhead generated by the scan coils can be reduced or completely removed. The stage developed for this purpose showed, however, a too-large position error, causing pixels to be non-square, which is a problem that has to be solved for this strategy to be viable.



The second strategy is a step-and-scan approach where the signal is de-scanned by a galvanometer mirror. This strategy has the advantage that the stage does not have to be very precise, and the scan frequency is relatively low. The main disadvantage is the throughput reduction due to stage settling times and the limited maximum frequency of galvanometer scanners. This chapter discussed methods for reducing the effect of the stage settling time by scanning multiple fields. With this method, some stage moves are replaced by beam movements. It is also shown that by accepting a de-scan error and switching to bidirectional scanning, the galvanometer mirrors can be pushed to the required frequency.

Table 4.1 shows an overview of the throughput at various dwell times for all the acquisition strategies presented in this chapter. From this table, it is clear that a moving stage acquisition, with compensation for scan coil overhead, is the strategy with the highest throughput. If a stage suitable for this approach is not available, a multi-field step and scan approach is a good alternative. The stage that was developed for the Apreo Multi-Beam was not performing as expected,

| Dwell Time | MS | MS AS | SS | SS MF4 | SS MF9 |
|---|---|---|---|---|---|
| 2µs | 32 | 32 | 26 | 30 | 31 |
| 1µs | 60 | 64 | 45 | 56 | 60 |
| 500ns | 113 | 128 | 70 | 100 | 115 |
| 200ns | 244 | 320 | 106 | 191 | 255 |
| 100ns | 396 | 576 | 128 | 274 | 426 |

Table 4.1: An overview of the throughput speed (in Mpix/s) for various dwell times in the acquisition methods described in this chapter. MS = Moving stage, MS AS= Moving stage with compensation for scan coil self induction, SS = Step and Scan, SS MF4 = Step and Scan 4 multi-fields, SS MF9 = Step and Scan 9 multi-fields

and the latter strategy has thus been chosen.

## ACKNOWLEDGMENTS

For help with the work with the de-scan galvo's, we would like to acknowledge Eoin Horgan for the work he did during his master thesis research.

# BIBLIOGRAPHY


[1] J. Stopka and P. Kruit, "Statistical coulomb interactions in multi-beam sem", *International Journal of Modern Physics A*, vol. 34, no. 36, p. 1 942 021, 2019.

[2] A. Zonnevylle, R. Van Tol, N. Liv, *et al.*, "Integration of a high-na light microscope in a scanning electron microscope", *Journal of Microscopy*, vol. 252, no. 1, pp. 58–70, 2013.

[3] N. Liv, A. C. Zonnevylle, A. C. Narvaez, *et al.*, "Simultaneous correlative scanning electron and high-na fluorescence microscopy", *PloS one*, vol. 8, no. 2, e55707, 2013.

[4] M. Guizar-Sicairos, S. T. Thurman, and J. R. Fienup, "Efficient subpixel image registration algorithms", *Optics letters*, vol. 33, no. 2, pp. 156–158, 2008.

[5] L. Reimer, *Scanning Electron Microscopy: Physics of Image Formation and Microanalysis*, 2nd ed. Springer, 1998, ISBN: 9783642083723. DOI: 10.1007/978-3-540-38967-5. [Online]. Available: doi.org/10.1007/978-3-540-38967-5.

[6] G. R. Römer and P. Bechtold, "Electro-optic and acousto-optic laser beam scanners", *Physics Procedia*, vol. 56, no. C, pp. 29–39, 2014, ISSN: 18753892. DOI: 10.1016/j.phpro.2014.08.092.

[7] Boston Micromachines, *Mid actuator count deformable mirrors*. [Online]. Available: http://www.bostonmicromachines.com/mid-actuator-count.html (visited on 09/12/2019).

[8] Thorlabs, *Large Beam Diameter Dual-Axis Scanning Galvo Systems*. [Online]. Available: https://www.thorlabs.com/newgrouppage9.cfm?objectgroup%7B%5C_%7Did=6057 (visited on 12/08/2021).

# 5

# MULTI-BEAM IMAGING IN THE FAST-EM PROTOTYPE

## 5.1. INTRODUCTION

The previous chapters focused on a method for transmission imaging that is suitable for a Multi-Beam SEM (MBSEM) and the requirements for optimized high-resolution, high-throughput signal generation and detection using this method, including MBSEM detector design considerations. This last chapter will discuss some considerations to build up a full MBSEM system. This chapter will thus discuss the final realization of a prototype for a commercially available MBSEM with the following specifications:

- MBSEM based on the Thermo Fisher Apreo SEM [1]
- 8×8 electron beams
- 3.2μm pitch on the sample
- 150pA beam current.
- 2 stigmators, one for beam stigmation and one for beam grid stigmation.
- Option to focus and stigmate the electron optical system using one beam from the grid (single beam mode).
- 4nm pixel size
- 1000× light-optical magnification
- Galvo mirror descan system [2]
- 8x8 Hamamatsu MPPC array with 3600 APDs per cell

- Scan engine and MPPC readout hardware designed and manufactured by Technolution.

The final configuration (not discussed in this chapter) will have a 1000pA beam current. To avoid Coulomb interactions deteriorating the resolution, an extra common crossover is added, as was shown by Stopka [3]. This chapter will go through the relevant parts of the system that were not discussed in the previous chapters.

## 5.2. ELECTRON OPTICAL AND LIGHT OPTICAL SYSTEM

A drawing of the electron optical system is shown in figure 5.1a. As can be seen, the optical system is fairly simple. It consists of a regular FEG source, a multi-beam generator (E1, E2, E3, ALA), a collimator lens (ACC), and a set of 3 final lenses. The electrodes above the aperture lens array (ALA), E1, E2, and E3, can shape the field above the ALA such that there is no field curvature in the accelerator lens (ACC). This is done by making sure that the lenses towards the edge of the ALA are weaker than the central lenses. The ACC collimates the beams and creates a common crossover in the coma-free plane of the final set of lenses. These lenses now focus the beams on the sample. The strength of the deceleration lens is determined by the desired landing energy, and the ratio between the HR and UHR lens strength determines the geometrical spot size and pitch on the sample. Those two lenses are thus also used to make small adjustments to the pitch to make sure that it is as close to 3.2 μm as possible (which also calibrates the pixel size).

The virtual source images are created by an aperture lens array, which consists of apertures with a diameter of 10μm and a pitch of 22μm . The thickness of the membrane is 10μm . The thickness of the membrane does not influence the lens effect, but a thicker membrane does increase the chance of contamination as there is more space for the material to be deposited (figure 5.2a). An even thinner membrane can be used for the lens array, but that is more fragile, and there is a chance of breaking it while handling. An SEM image of nine of the apertures is shown in figure 5.2b.

### 5.2.1. MICROSCOPE SETUP

The setup consists of a Thermo Scientific Apreo SEM in which the source has been changed to one made according to the design by Mohammadi-Gheidari [4]. Some improvements to the source were made in terms of manufacturability and serviceability, as well as making the source more resistant to the high electric field strengths present. To the standard SEM, an extra stigmator was added to allow for both pattern and probe stigmation correction (described later in this

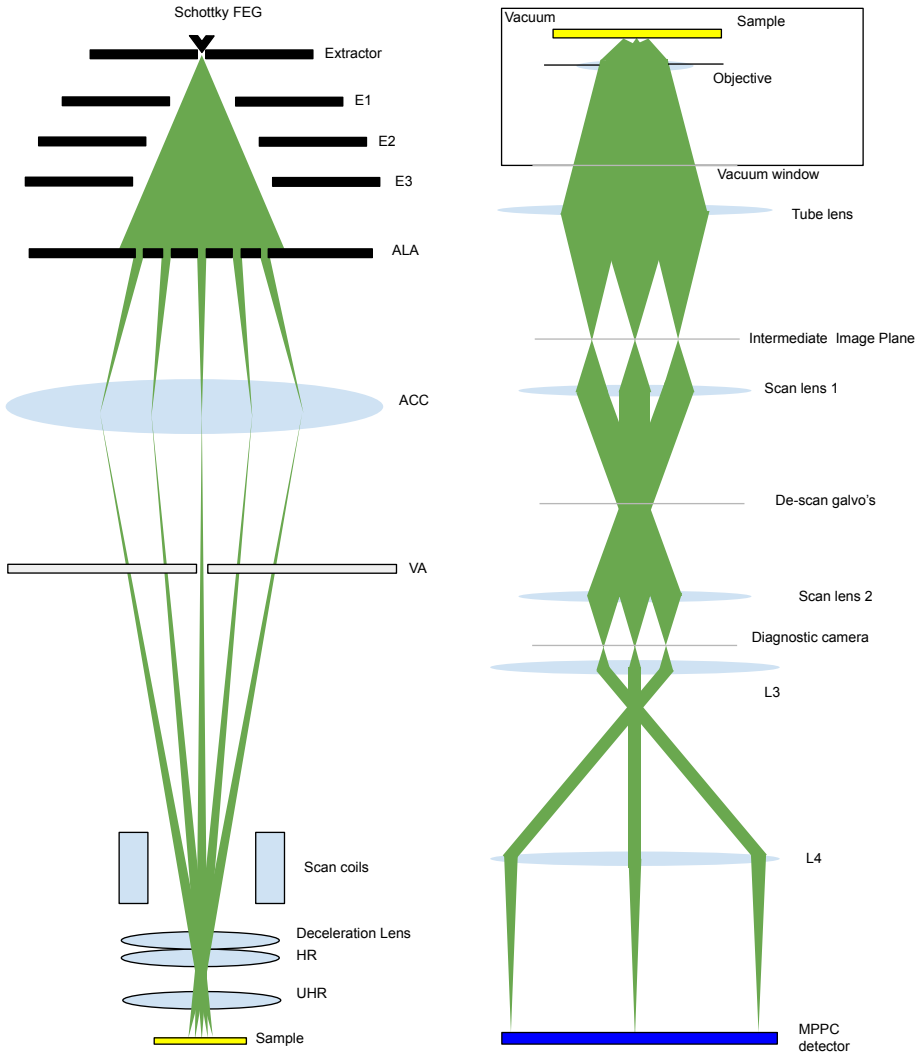


(a) (b)

Figure 5.1: (b) Schematic drawing of the electron optical system in the MBSEM prototype, not to scale. The drawing shows the on-axis beam and four off-axis beams. The source unit consists of E1, E2, and E3, the aperture lens array (ALA), and the accelerator lens (ACC). The accelerator lens is a three-electrode Einzel lens, of which the last (A3) is set to determine the position of the common crossover. The variable aperture(VA) can be used to select a single beam out of the grid. The final lens is a 3-lens compound lens. (b) A schematic drawing of the light optical detection system, not to scale. The drawing shows the on-axis beam and two off-axis beams. The beam-splitter to the diagnostic camera is omitted and drawn in line with the rest of the optical path. Note that the optical system is kept as telecentric as possible, such that the magnification is independent of the defocus.

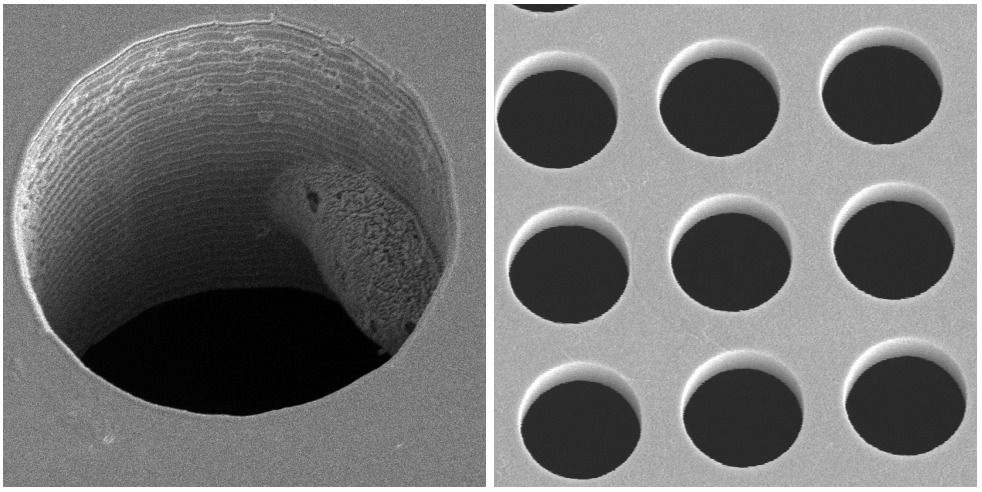

(a) (b)



Figure 5.2: Tilted SEM images of 10μm apertures. (a) A contaminated aperture from the prototype MBSEM. The membrane was 100μm thick, but the aperture had the same diameter. (b)Shows the apertures as they are installed in the apreo MBSEM with a membrane thickness of 10μm .

chapter). In the SEM chamber, an X, Y, and Z stage was placed mounted to a vacuum chamber door. This (prototype) stage had a range to image one scintillator of 15x15mm, which can contain as many as 200 ultrathin sections. In later versions of FAST-EM, the range of this stage was adjusted to be able to cover $3 \times 3$ scintillators. The Z-stage is just for focusing the light-optical objective(Nikon Plan Apo 40X/0.95[5]) that is mounted underneath the scintillator. figure 5.1b shows a schematic drawing of the light optics used in the detection system. The light coming from the objective is guided outside the chamber via a folding mirror and through a vacuum window. The light is now focussed into an intermediate image plane by the tube lens (250mm focal length). To ensure that the light fits onto the de-scan mirrors (chapter 4) that are in the light path (with a diameter of 10mm), the pupil of the objective is imaged and de-magnified onto the de-scan mirrors. This is done by placing a 75mm lens with its focal point in the intermediate image plane behind the tube lens. This de-magnifies the image of the pupil by a factor of 75/250 = 0.3 to a spot of 2.85mm on the de-scan mirrors. With another 75 mm lens, another intermediate image plane is created. Before this image plane, there is a 90-10 beam-splitter, behind which is the diagnostic camera. On this camera, to which 10% of the light is guided, the images of the beam spots can be monitored (see an example in figure 5.3). The other 90% of the light goes to a magnification stage consisting of an 8mm and a 160mm lens, creating a 20x magnification of the intermediate image. This image is projected

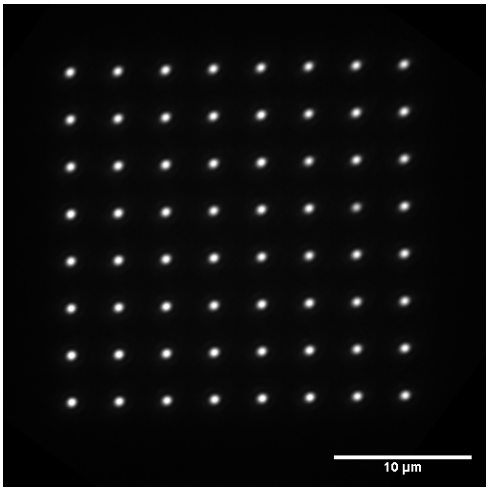


Figure 5.3: Image of the 8x8 beam grid on the diagnostic camera. The diagnostic camera allows for constant monitoring of the beam grid and the execution of alignments. Not due to uncompensated distortions in the electron optical system, the grid does not seem perfectly square.



onto a Multi-pixel photon counter (MPPC) array, for which the hardware was designed by Technolution B.V. The optical system is telecentric in this plane, such that the magnification is independent of any defocus of L4. The depth of focus in the image plane is more than 200mm; thus, the exact location of the detector is of less importance. The MPPC array [6] consists of an 8x8 square grid with MPPC's of 3mm and a pitch of 3.2mm. This detector is placed on a rotational stage such that the detector grid can be rotationally aligned to the beams. For translational alignment, the 8mm lens is mounted on an x-y stage. These MPPCs are read out in parallel, and there is an analog output available for the cell in location (4,4). The signal processing of the MPPC array is done by means of a set of analog amplifiers and an FPGA. A sync signal is provided to make synchronize the signal processing to the scan.

The de-scan angle required when a pitch of 3.2µm is scanned by the galvo mirrors is determined by the demagnification of the objective pupil and the focal length of the objective. The focal length of this objective is calculated using the magnification (40x) at the specified tube lens focal length (200mm): 200/40 = 5. This gives a total angle to be descanned in the 3.2e-3/5 × 1/0.3 = 2.1mrad. Note this is an optical angle, which is twice the mechanical angle of the mirrors. This is only a very small part of the range of the galvo mirrors (698mrad). The rest of the range can be used for alignment of the beam spots with the detector during acquisition or multifield imaging (see previous chapter).

The light collection of the total optical system is limited by the collection ef-

ficiency of the objective, the limited reflectivity of the mirrors, and the transmissivity of the lenses. The collection efficiency of the objective is calculated by assuming a homogeneous light source in the YAG:CE. An optical air objective with an NA of 0.95 will now collect approximately 18% of the light that goes down, which is 9% of the total light. Note that when an air objective is used, of the light that goes down, only 58% of the light leaves the scintillator at the bottom due to total internal reflection (the refractive index of YAG:CE is around 1.8). The mirrors all have a protected silver surface, which yields a reflectivity of around 97% , and the lenses reflect about 0.2% of the light (if the correct anti-reflective coating is chosen). This yields a total transmission of the system of: 0.09 (Objective) * $0.998^5$ (lenses)* $0.97^5$ (mirrors)* 0.9 (beam splitter) = 0.07.

### 5.2.2. DETECTOR

The detection system uses a sampling rate of 40Mhz, independent of the dwell time. The scintillator used in the system (YAG:CE) has a 1/e decay time of 70ns, which is a lot slower than the sampling time of the detection system (25ns). The detection system integrates the signal over those 25ns, making sure no information is lost. The readout of the detector is synchronized with the scan engine through a TTL signal.

### 5.2.3. TEST SAMPLES

To test the system, two types of samples were used: A test sample consisting of a pattern etched in a tungsten layer on top of a scintillator that was coated with a thin aluminum conductive layer. This sample was made through e-beam lithography. The second sample is a tissue section on top of a scintillator with in between a thin conductive Boron layer. The first type of sample is mainly used because its structure can be very predictable, and it can be used to measure the resolution of the system. A way to characterize the beam spot in an SEM is to use a knife edge measurement. Depending on the imaging mode (the electrons that are detected, in this case, the transmitted electrons), this has some challenges. For this measurement, the tungsten test sample is used. The beam scans over the tungsten, and if the edge is (close to) 90 degrees, the beam profile can be measured in transmission mode. Classically, the pattern used for this is fairly thick, around 200nm, in order to stop all the electrons from transmitting when the beam hits the tungsten. This, however, creates a problem as illustrated in figure 5.4. This figure shows the results of a Monte-Carlo simulation using Casino [7] 3.3. For the simulation, a 20nm and 200nm thick tungsten layer was used. The landing energy was set to 5keV, and the spot is a 2.5nm top-hat spot profile (this is not a good approximation of a beam spot but does serve to show the effect of pattern thickness). As the beam scans from the tungsten to the area without

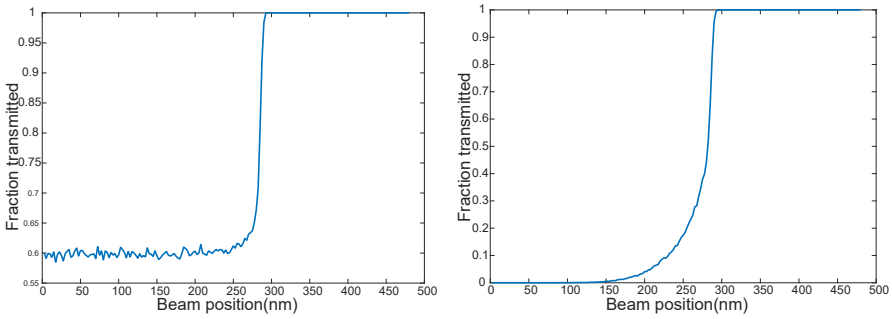


(a) . (b)

Figure 5.4: Monte Carlo simulations performed using Casino 3.3 [7], showing the transmitted electron for a (a) 20nm knife edge and a (b) 200nm knife edge. The simulation was performed with an electron energy of 5keV and a spot size of 2.5nm. Note that despite the fact that on the 20nm knife edge, 60% of electrons are still transmitted through the edge, the edge appears considerably sharper than the 200nm knife edge.



tungsten, more and more electrons can pass through the side of the edge. This causes a non-sharp edge in the image that is acquired (similar to the resolution loss that is shown in chapter 2), with a long tail. A way to mitigate this issue is to make the side wall as low as possible and rely on the high contrast that the transmission imaging yields. Therefore, the test sample used in this sample has a thickness of the tungsten pattern of only 20nm. In the example shown, the 20nm thick layer yields a 25-75 resolution of 5nm, and the 200nm thick sample has a 25nm resolution, while the beam does not change in size. Note that an even thinner pattern would be beneficial; a 5nm layer will yield a resolution measurement of the beam size. These samples are, however, hard to make, and at this thickness, the sharpness of the knife edge becomes more important.

## 5.3. ALIGNMENT AND CALIBRATION

### 5.3.1. LIGHT OPTICAL ALIGNMENT

The light optical alignment of the system consists of two different parts. For both alignments, the first step is to get the sample in focus with the objective lens. During the build of the optical system, the lenses were placed such that the diagnostic camera and the MPPC detector were both in the correct image plane. Therefore, when the light is in focus on the diagnostic camera, it is also in focus on the detector. During this focusing process, the magnification of the optical system is also set by placing a camera in the MPPC plane and a calibration sample on the sample stage.

#### LIGHT OPTICS TO ELECTRON OPTICS ALIGNMENT

The first part of the alignment is to align the light-collecting objective to the electron beams. The electron beam and the light objective have to be aligned to each other such that the light from the scintillator falls within the usable field of view of the objective (around 300μm in diameter). This field of view is reduced by the multifield acquisition scheme: for a 3x3 multifield, a 77μm field of view is required section 4.4.2. Because the stage still has magnetic bearings (discussed in the previous chapter), this will also cause the beams to move with every stage move. This movement of the beams will cause a misalignment with the detector and a misalignment between two separate fields within the megafield. This can be easily accommodated by using a beam-shift offset on the e-beam scan, but it does make the alignment more strict. It is, therefore, important to align the electron beams to the objective within about 50μm . The alignment is performed by changing the optical path and putting the diagnostic camera directly in the image plane of the tube lens. This is required because the exact angle of the galvo/mirrors is unknown, and this variable has to be excluded. As a sample, a bare scintillator is used, and the e-beam is switched to spot mode. By moving the spot around on the sample, the edges of the usable field of view of the objective can be found. At these edges, the intensity of the light on the camera drops, and the grid looks distorted (see figure 5.5a. The location where the objective is aligned with the e-beam is in the middle of these edges. From this image, the direction and distance for the objective to be moved are calculated, as is shown in figure 5.5b. In this example, the light optical objective has to be moved 58μm in the x-direction and 55μm in the y direction to be aligned to the electron microscope. If the adjustment mechanism of the objective is designed well, this method can align the two optical systems well within 10μm .

#### BEAM SCAN DIRECTION ALIGNMENT

The second alignment that is performed is the alignment of the beam-scan direction. The scan of the e-beams has to be aligned with the axes of the beam grid. This is done by choosing line scan mode in the SEM and observing the generated image on the diagnostic camera. When the scan direction is not aligned to the beam grid, an image like figure 5.6a is created. The lines that are created by scanning the beams are not aligned to the pattern axes. This is adjusted using the SEM scan rotation setting until the lines are aligned to the pattern axes as shown in figure 5.6b. This alignment is precise to about 1 degree and needs further adjusting when the image is created (discussed in a later section).

#### BEAM SPOTS TO DETECTOR ALIGNMENT

The third alignment is the fine alignment of the beam spots with the detector, which entails both translation and rotation. This is to make sure that every beam

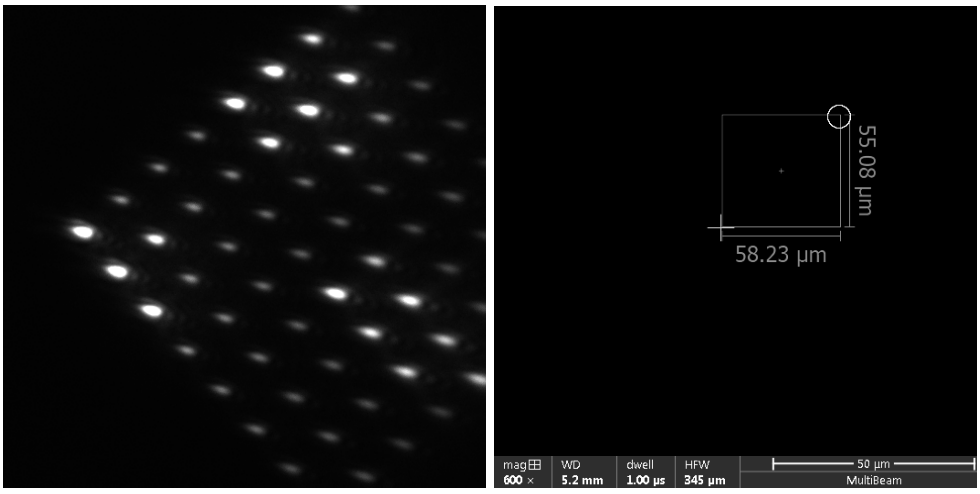


(a) (b)



Figure 5.5: (a) An image taken with the diagnostic camera for a beam grid that is on the edge of the objective field of view (FOV). The image quality is greatly reduced compared to figure 5.3. (b) An image illustrating the process of aligning the optical objective to the electron column. The circle marks the middle of the light objective FOV, and the cross marks the center of the e-beam scan (the center of the electron column if properly aligned).

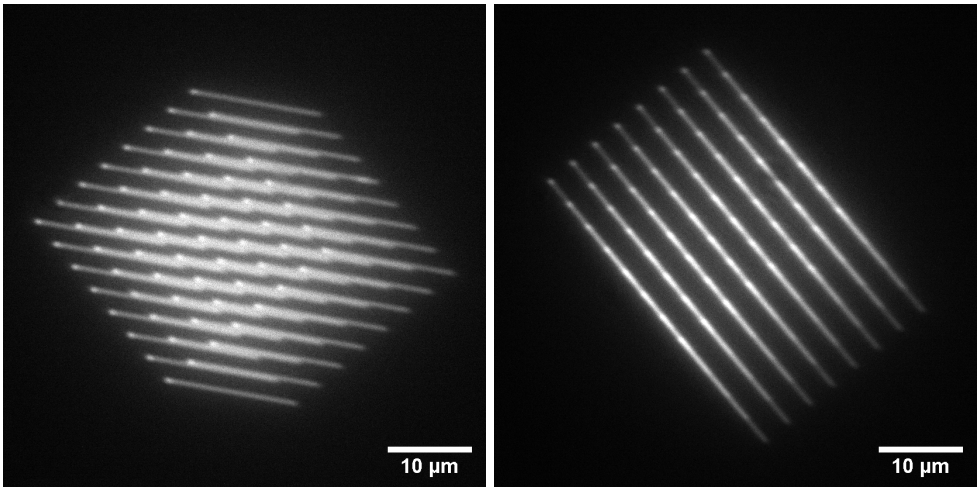


(a) (b)

Figure 5.6: (a) Diagnostic camera image of the beam grid scanning in a line that is not aligned to the pattern axes,(b) Using the SEM scan setting, this can be adjusted such that the line scan is aligned with the grid pattern.

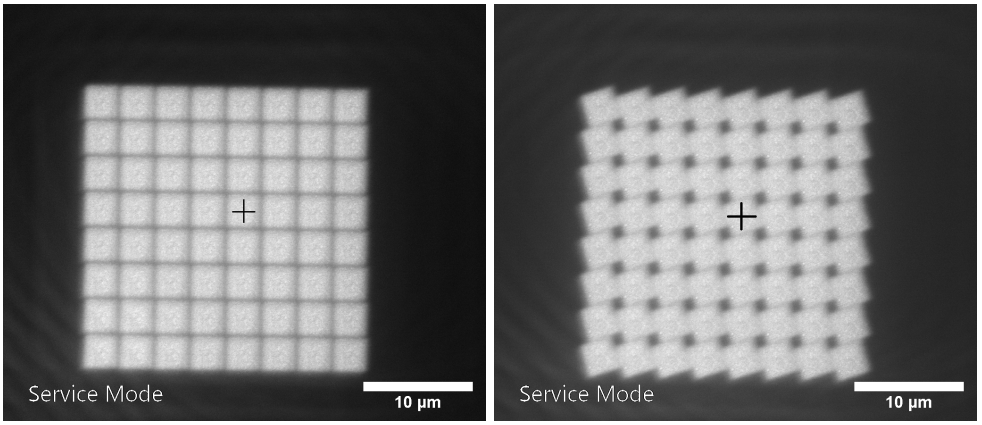


(a) (b)

Figure 5.7: (a) An image created by scanning the beam grid over the scintillator but only using a single cell from the detector array. This is used to align the beam grid to the detector array. (b) It shows the same image but with a detector that is rotated incorrectly. In the prototype, this rotation is adjusted manually until all the squares are aligned to the grid, as in Figure (a). The black plus sign indicates the position of the detector cell with respect to the beam grid.



spot is exactly centered on each MPPC in the array. This alignment is performed by using the single-cell output of the detector and feeding this into the external detector input of the SEM. When scanning the electron beams across one detector, this creates an image of all the beams on one detector (and 8×8=64 the same area of the sample). An example of this can be seen in figure 5.7a. The first rough alignment is done by the translation stage on which lens L3 is mounted. After this first alignment, L3 is fixed, and further (fine)translations are performed by using the SEM's beam shift function. The detector rotational alignment is performed by rotating the detector such that all the squares in the image are aligned with the scan direction. When the detector is not rotated correctly, the image looks like what is shown in figure 5.7b.

#### DESCAN ALIGNMENT

The last optical alignment is that of the descan. As was shown in the previous chapter, both the amplitude and phase shift of the descan are dependent on the scan frequency. Thus, this is dependent on the selected dwell time. So, for a number of dwell times, these settings can be calibrated and tabulated. This is done by externally providing (through an arbitrary waveform generator) a known sawtooth wave on the e-beam scan and the same wave on the descan galvos. The amplitude of the e-beam scan is that required to scan exactly one pitch. For the descan, the amplitude and phase shift is adjusted such that the beam spots in

the diagnostic camera are stationary.

### 5.3.2. ELECTRON OPTICAL ALIGNMENT

After the light optical alignment has been dealt with, we can focus on the electron optical alignment. Not all these alignments have to be performed every time the system is used. Some only have to be done after the first startup, and others have to be performed once in a few months.

#### SOURCE TO COLUMN ALIGNMENT BY GUNSHIFT.

Because the exact location of the electron gun is not fixed to within more than a few 100 μm , the grid of beams has to be shifted regularly so as not to be blocked by pumping apertures further down in the electron optical path. In earlier columns, this had to be done mechanically (such as the Nova NanoSEM mentioned in earlier chapters); in the Apreo SEM, it is performed purely electronically. Gun shift is adjusted in the crossover mode of the SEM, which uses the gun shift and tilt coils to scan the beam over the variable aperture. The other lens settings in crossover mode have the same setting as in normal imaging modes. Therefore, during the scan over the variable aperture, the detector will only detect a signal when the beams can pass all the way through the column. This position can then be determined relative to the center of the crossover scan (by the gun tilt and shift coils), and a DC offset is added to the shift coils. By going from negative to positive gun shift in both x and y successively, the beam first appears in crossover mode and then disappears again (as it moves over the pumping aperture above the variable aperture). The middle setting of the gun shift between the beam appearing and disappearing is the correct setting of the gun shift. This setting has to be done for all the landing energies that will be used and only has to be performed after the source has been installed.



#### LENS ALIGNMENT

Lens alignment in a regular SEM is performed by adjusting a shift of the beams before the final lens. This is done by wobbling (rapidly changing the lens excitation in a sine pattern) the lens while rapidly acquiring an image and moving the beam shift until the image stays stationary during this wobbling. In the multibeam SEM, this method does not work for three reasons. The first reason is that there is no central beam in a square pattern with an even number of beams, so there is no single beam that will be stationary during the lens wobbling. The main reason, however, is that the final lens is not a single lens but a combination of three lenses (to get the desired demagnification). A third minor (and probably manageable) reason is that the alignment method using regular lens alignment has its pivot point somewhere within this compound lens. To align the electron

optical system, the beam energy is wobbled instead of the lens strength; during this, the image of the pattern is observed on the diagnostic camera. If this pattern is only rotating around its center point and not translating, the electron optical system is well aligned. The rotation will always occur due to the use of magnetic lenses. The alignment is adjusted by changing the gun tilt during the wobbling of the beam energy. This setting can be tabulated for different beam energies. Due to drifts in the system, it has to be adjusted from time to time. Usually, this is prompted by a resolution degradation in the image.

#### STIGMATOR ALIGNMENT

Setting the stigmator is done to make sure the beams have no astigmatism; this works best when the beams go through the center of the stigmator. The beams are centered in the stigmator using a DC offset on the stigmator coils. In a regular SEM, the stigmator alignment is performed in the same way as the lens alignment but by wobbling the stigmator instead of the final lens. The alignment is adjusted by adjusting the shift component on the stigmator quadrupoles. Again, because of the lack of a central beam, this does not work for our multi-beam SEM. Therefore, the stigmator is wobbled while observing the image of the beam grid on the diagnostic camera. The stigmator is aligned when the grid deforms around the center of the pattern, and no translation of the pattern is observed.

#### A3 AND E2 SETTING

The excitation of A3 in the accelerator lens (collimator) is used to determine the longitudinal(z) position of the common crossover in the final lens. This position should be in the coma-free plane of the final lens. When this position is not correct, stigmation of the outer beams will be observed in the image. To set it correctly, first, the column alignments have to be performed as described above. Otherwise, these will also influence the result. The setting is adjusted by adjusting the value of A3 from low to high and acquiring an image with all beams (after refocusing the beams with the final lens). Because the pitch also slightly varies while this is done, the easiest way to get the images is to scan all beams over the single-cell detector. Now, the resolution of each image is analyzed using the program image.exe provided by Thermo Fisher. The program detects edges and determines the 35-65 (or something else if specified) edge resolution. The results of such a measurement are shown in figure 5.8.

It shows both the standard deviation of the measured resolution and the average resolution. Both have to be minimized, which gives a single optimized setting. Note that in this case, the minimum resolution is impacted by the highest available scan resolution (smallest possible pixel size). In this case, A3 excitation of 3250V was selected. After A3 is set, E2 still has some effect on the stigmation of

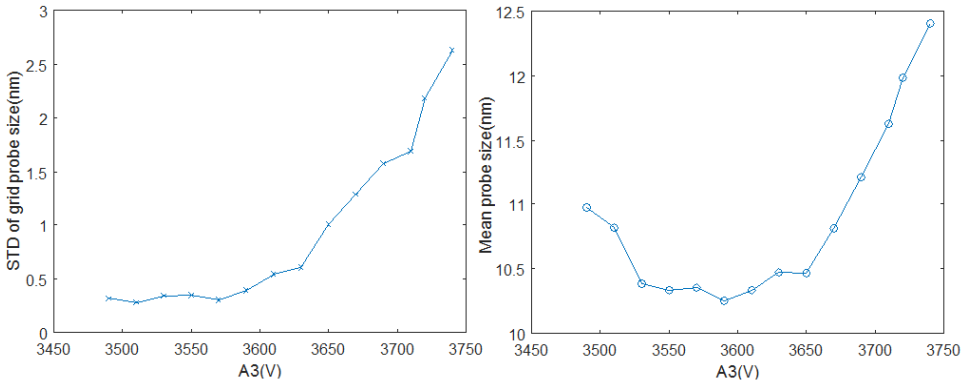


Figure 5.8: Plots showing (left) the standard deviation of the spot size and the (right) mean probe size as a function of A3 voltage. This is used to optimize the setting of A3 (in general, the ACC lens), which determines the location of the common crossover shown in figure 5.1a.



the outer beams. E2 is adjusted in the same fashion as A3 to further reduce the standard deviation of the resolution.

### MAGNIFICATION (PITCH) CALIBRATION

The ratio between the geometrical spot size and beam pitch is set by the multi-beam source unit. Therefore, for a certain pitch, there is a minimal attainable spot size. The spot size has to be in the regime where it is governed by the aberrations and geometrical spot size, not off-axis aberrations. The aperture angle, the beam size in the accelerator lens, and the pitch in the accelerator lens are determined by the design of the multi-beam source, which was copied from earlier prototypes [4]. The balance between the contributions from aberrations and the source image can then only be set by the magnification. Given the aberration coefficients of the system, this led to a magnification giving a pitch of 3.2 μm . The pitch in this system is adjusted by changing the ratio of two lenses in the final lens. For instance, to increase the pitch, the HR lens excitation is increased, and the immersion lens excitation is reduced. To set the pitch roughly, the light optical system can be used, but since it only has limited resolution and its magnification is also not known very accurately, another step is required. This is again done by scanning all the beams over the single detector. In this case, all beams scan the same area of the sample. As the scan amplitude (magnification) is well calibrated in the SEM, the distance between the same features scanned by different beams (see figure 5.9) is the pitch of the beam grid.

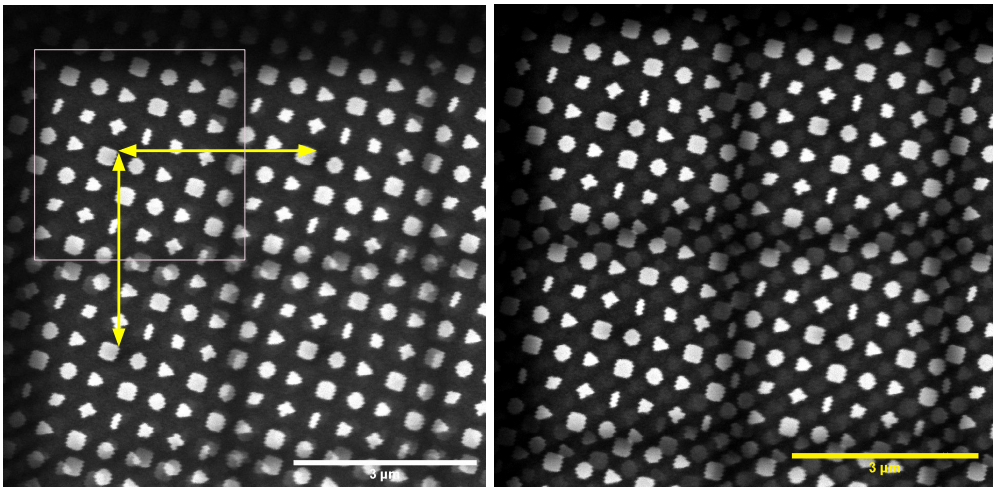

(a) (b)

Figure 5.9: 4 images created of the same structure by four different beams in the beam grid. This image is used to calibrate the beam pitch, measured by the distance between two of the same features scanned by different beams (the yellow arrows in (a). This pitch can be increased by increasing the HR lens excitation and reducing the immersion lens excitation.

#### SCAN AMPLITUDE CALIBRATION

To get a proper image, we want each beam to scan exactly the distance of 4nm for each pixel (3.2µm / 800) in the image. In our acquisition system, the scan amplitude is set in the unit V/pixel. A rough estimate of this scan amplitude can be set by observing the (line)scan on the diagnostic camera. If the scan amplitude is too small (figure 5.10a), a spot where the beams do not reach can be seen, and when the amplitude is too large (figure 5.10b), a spot where the scan of two neighboring beams overlap will be slightly brighter. Amplitude is set correctly; the lines will look (mostly) continuous. The final acquisition amplitude, however, has to be set using an acquired image. The easiest way to do this is to scan 900 pixels instead of 800 and make sure that the overlap area for two neighboring beams is exactly 100 pixels (barring some issues with the grid distortions, discussed in the next section).

#### GRID DISTORTION CORRECTION

Setting the regular SEM stigmator to remove the stigmation from all the beams at the same time has the added effect that it will also distort the beam grid (see figure 5.11). This effect is less if the stigmator is at exactly a common crossover of the beams, but due to finite sizes and lens aberrations, this position is, in practice, not present. Therefore, the system needs two stigmators, one for the beams

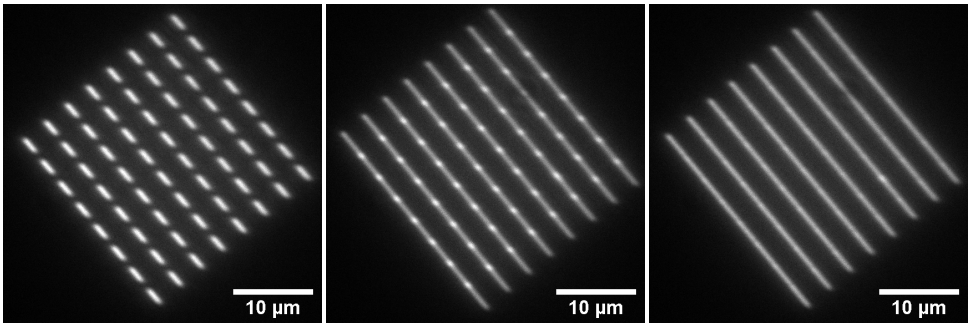


(a) (b) (c)

Figure 5.10: Diagnostic camera images showing a line scan where (a) the scan amplitude is too small, (b) too large, and (c) correct.



and one for the pattern. To find the best settings for the pattern stigmators and other parameters, the images created by every beam are stitched using ImageJ. An example of such an image is shown in figure 5.11 (this is the image used for figures 5.12a and 5.12b). When there are no distortions and the scan amplitude and rotation are set correctly, the images should stitch to a 6400×6400 pixel image. In practice, this is, however, not the case, and the number of pixels required to move every 800×800 is calculated. These are represented as arrows in figure 5.12. These representations make it clear what kind of adjustments have to be made to reduce distortions in the image, but also how to compensate for other errors in the acquisition. The distortions shown in figures 5.12a and 5.12b are very high. The top right beam is 420+396=816 nm out of place compared to the bottom left beam. In figure 5.12a, we can, however, see that this is a clear shear distortion, which the pattern stigmator can reduce. When this was performed, the distortions in figure 5.12c are left. This is actually not a distortion but a slight error of 0.4 degrees in the scan rotation (which can directly be calculated from this data). After the scan rotation was adjusted, the distortion shown in figure 5.12d is left. Again, this is not an actual distortion but an error in the scan amplitude (in this case, the scan amplitude was set too high). After setting the scan amplitude correctly, a slight stretch distortion (the pitch in x was bigger than the pitch in y) was observed and adjusted for by the pattern stigmator (not shown in the figure). The leftover distortions shown in figure 5.12b do not show a clear pattern and are harder to compensate for. They can be a result of column misalignment or problems in the column, such as the charging of apertures. Overall, the distortions have been greatly reduced.

The leftover distortions will cause that, even if exactly 3.2µm is scanned, the images of the various beams never align. For this, a field correction is ap-

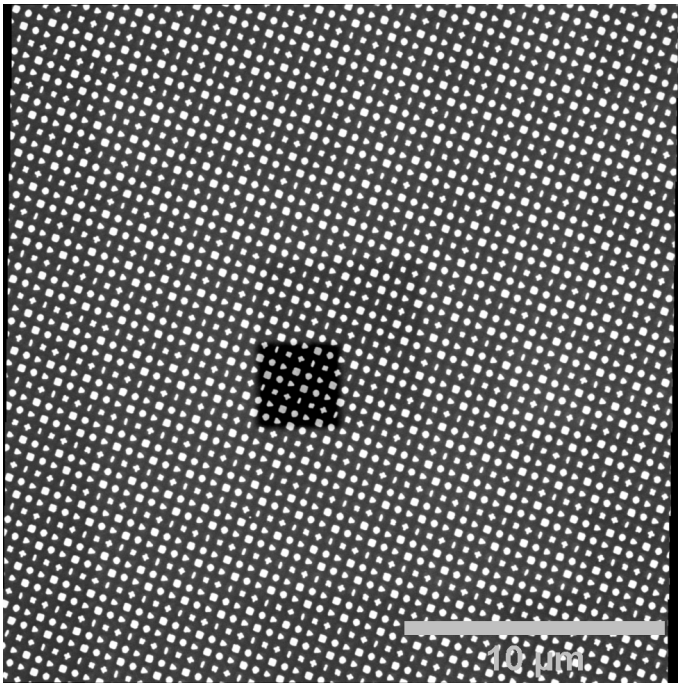


Figure 5.11: An image created for measuring the distortions in the multi-beam pattern as well as scan rotation and scan gain. The image was acquired at a dwell time of 3.2 µs and a landing energy of 5keV. The sample is a 20nm tungsten layer with holes of various shapes on top of a chromium layer on a YAG(CE) scintillator. The stitched image shows the shear distortion from figure 5.12a as black bands at the top left and bottom right of the image.

plied during acquisition, such that stitching of the cells afterward is not required. First, an image is acquired where all beams scan 100 pixels more than is required (a nominal 100-pixel overlap between neighboring beams). When a cross-correlation is now calculated between the neighboring beams, using the grid stitching algorithm provided in Fiji [8] [9], the shift is never exactly 800 pixels. The shift that is left is the distortion in the grid. The maximum extra shift (or maximum distortion) is the overscan that will be used for the final acquisition. During the acquisition, the images are shifted such that they match up correctly, using the data found using the cross-correlation. For example, each beam scans 840 pixels instead of 800 pixels, and let's say the second beam is moved 3 pixels (12nm) to the right with respect to the first beam (top leftmost beam). This means that out of the 840 pixels scanned, the first three are discarded during acquisition, so no post-processing is necessary. An imaging result using this calibration is shown in figures 5.14b and 5.14d. The images show a full 8×8 multi-beam field and a zoomed-in area. The grid distortion compensation makes sure

that there are no edges visible in the acquisitions. In the case shown in figure 5.12, the maximum overscan is 25 pixels, which creates an extra scan overhead of around 6% .

### 5.3.3. RESOLUTION

Now that the system has been completely aligned, we can measure the beam resolution. A resolution map of the image created for the last settings (figure 5.12e) is shown in figure 5.13. The average resolution found is 6.9nm 35-65 (13.8 FW50) and a standard deviation of 0.9nm at 5 keV. This will, however, be dependent on the total current in the system, as at higher currents, coulomb interactions will be contributing more to the resolution. This can be mitigated by adding crossovers in the system [10], [11].

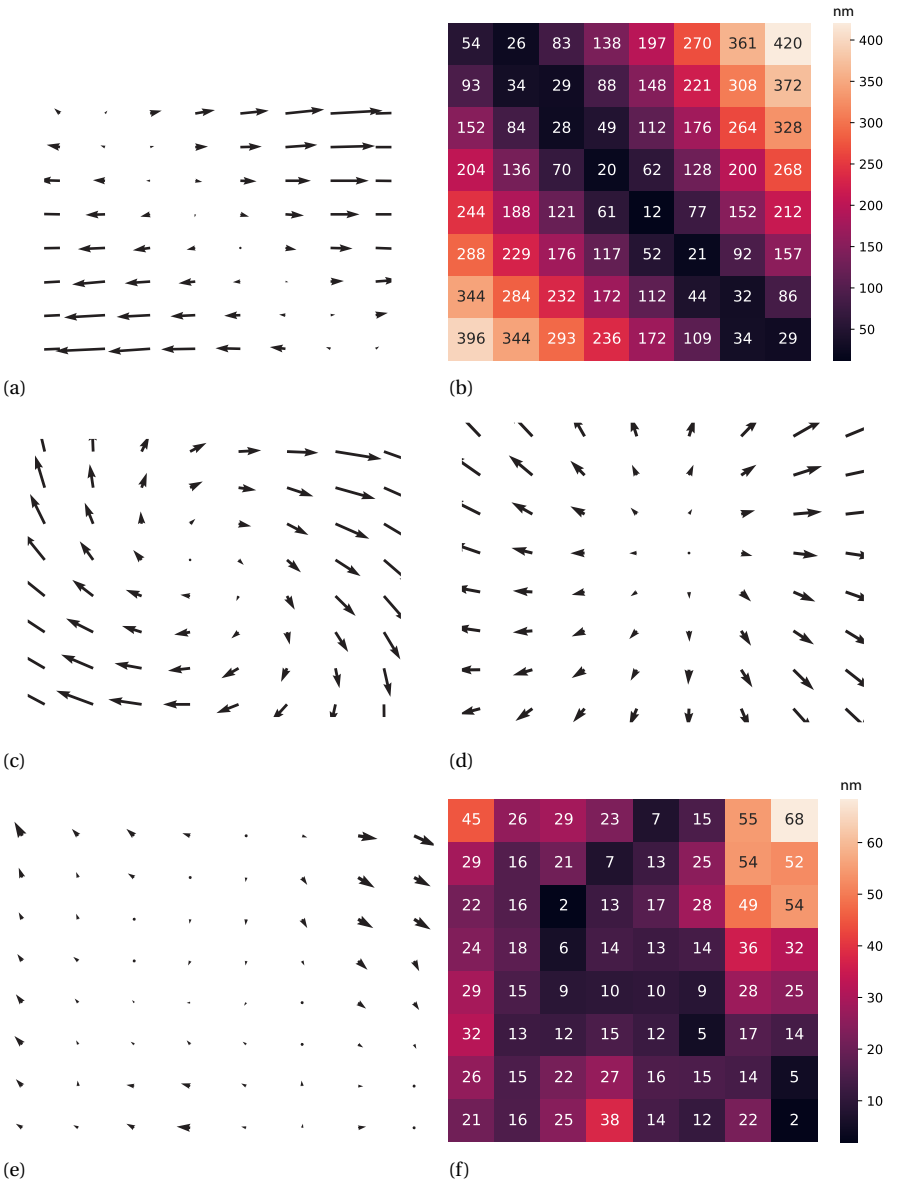


Figure 5.12: Figures showing the process of distortion correction in the MBSEM. The values are calculated using the image offsets that are required in order to stitch the images into the nominal image size of 6400x6400 pixels. The starting values when only probe focusing and stigmation have been performed are shown in figures (a) and (b). The distortions are very large and clearly show a shear component, which has to be compensated for with the pattern stigmator. When this is finished, there is a rotation visible (c); this is compensated by scan rotation. Now, the pattern of arrows shows (d) a scan amplitude that is too small. (e,f) after going through the complete process of compensation, only relatively small distortions are left without a clear pattern. Note that figures (b) and (f) give the length of the distortion vector, which can be relative to any other point in the grid.

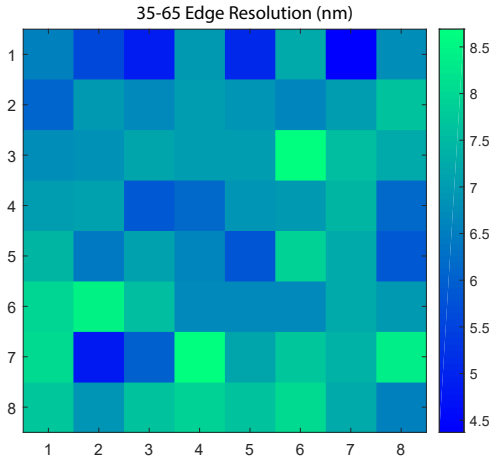


Figure 5.13: Resolution map of the images created for the distortion maps in figure 5.12e. It shows a good overall resolution, but the knife edge and some vibrations in the stage still limit the measurement. The average resolution found is 6.9nm 35-65 (13.8nm FW50) with a standard deviation of 0.9nm, showing good uniformity.



## 5.4. IMAGING

### 5.4.1. DARK LEVEL AND GAIN CALIBRATION

After the alignments that were discussed in the previous section are performed, we are almost ready to start imaging. The last step that has to be performed before every acquisition is the dark level and sensor gain calibration. The overvoltage sets the overall gain of the MPPC array. This overvoltage is the same for every MPPC in the array, but the gain curves of each MPPC differ slightly. The same holds for the exact dark current coming from each MPPC. Therefore, the dark offset and gain are digitally adjusted during acquisition. Before every acquisition, these values are calculated. The dark level is determined by acquiring multi-beam images with the electron beam off (dark image). The value for each cell is now the dark value. Another image is acquired on a bare area of the scintillator with the beam on (light image). The following formula calculates the digital gain per cell ($G_i$):

$$G_i = \frac{L_i - D_i}{< L_{1-64} > - < D_{1-64} >} \tag{5.1}$$

Where $L_i$ is the average value in the light image per cell, $D_i$ is the dark offsets per cell calculated earlier, $L_{1-64} >$ is the average light image value of all the cells, and $D_{1-64} >$ is the average dark image value of all the cells. A result of this compensation can be seen in figure 5.14. It shows an image that is not compensated for dark level and gain variations, and it shows an image that has been compensated. This method has two complications that can make it difficult to do it correctly.

The first one is that the area where the light image is created should have as little detail as possible (the scintillator should be as bare as possible). If this is not the case, the gain value can become lower (or sometimes higher) than it should be. The second complication is a possible change in light-optical alignment between the creation of the light images and the final image. Both of those effects can still be seen in figure 5.14b: the bottom row is a little bit lighter than the rest of the image due to a slight change in alignment. In the top row, there is one beam for which the gain value is incorrect, causing it to also be light. Nevertheless, the image looks much more uniform than the uncompensated version.

### 5.4.2. MEGA-FIELD IMAGING

The next and final step is to create many fields like the one shown in figure 5.14b and stitch these together. After a single field is acquired, the stage is moved 24µm such that there is a 1.6µm overlap between the fields. After the fields are acquired, they are stitched together using Fiji [8] [9]. For a proof of concept, this is performed for a 10×10 mega-field. This result is shown in figure 5.15. The time to acquire this image was 2-3 times faster than a regular SEM. The main bottlenecks are the acquisition hardware in the prototype, which was not designed for fast mega-field acquisition, and the stage, which was not designed for a short settling time. Note that the mega-field seems somewhat rotated. This is due to the stage movement not being perfectly aligned to the beam grid axis.

For this mega-field, the stitching of the fields was still quite time-consuming (it takes the same amount of time as the acquisition). In the final product, the acquisition makes use of an interferometer. For every field in the mega-field, the stage position is exactly known, and the image can be placed at the correct position without calculations. Due to the same interferometer, the stage can be optimized for settling time instead of accuracy.

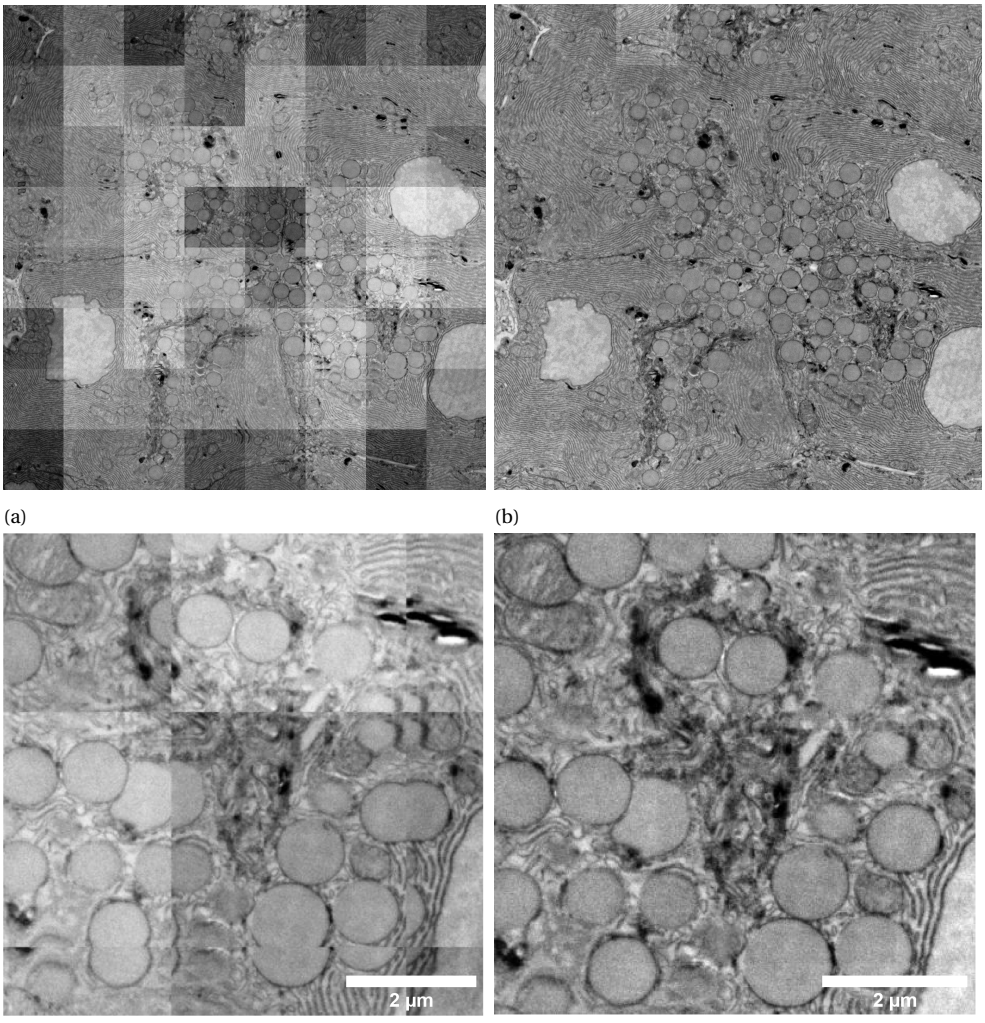


(a) (b)

(c) (d)

Figure 5.14: Multi-beam acquisitions showing the effect of the dark level, gain, and the grid distortion compensation. The images were acquired of an 80nm thick rat pancreas section stained by the OTO protocol. The dwell time was 3.2 $\mu s$ and a landing energy of 5keV. (a) is a bare image with no compensation, and (b) has been on the fly compensated for dark level and gain variations as well as grid distortions? Small variations are still visible in the bottom row, and one beam image in the top row. Figure (c) shows a zoomed-in area of a few beams without all compensations, and (d) shows the effect of the compensations. It cannot be observed that the image was created using different beams.

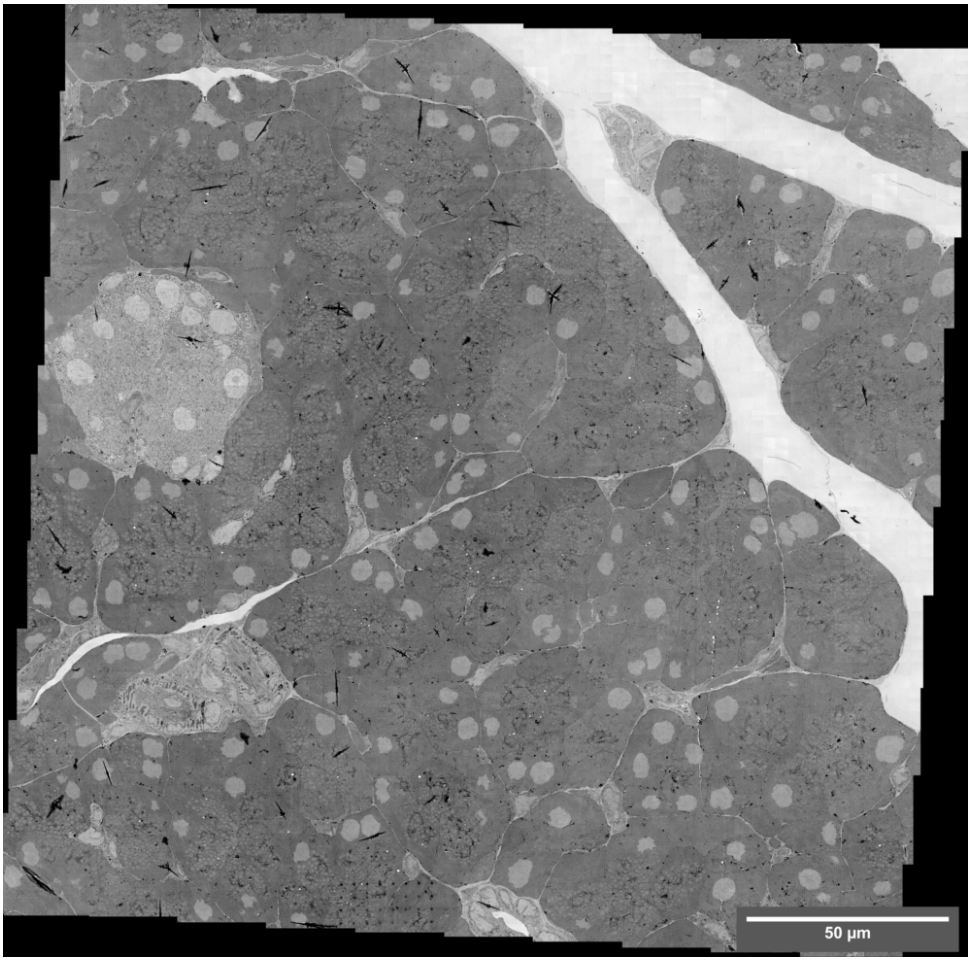


Figure 5.15: 10x10 megafield of an 80nm thick rat pancreas section stained by the OTO protocol. The image was acquired at a 3.2µs dwell time and a landing energy of 5keV. For digital versions of these images, see the following links. TU Delft Catmaid Nanotomy.org

## 5.5. CONCLUSION

In this chapter, we have presented a Multi-beam prototype that can image thin tissue sections. We have shown successful alignments of both the electron and light optics. The distortion present in a multi-beam pattern can successfully be mitigated so that stitching is not required with a single field. The final result was the acquisition of a 10×10 mega-field, which proves that the machine works as intended.

## 5.6. ACKNOWLEDGMENTS

This chapter has seen a lot of help from Andries Effting, Daan Boltje, and Job Fermie from Delmic B.V. for the detection, optical path, and megafield acquisition. Furthermore, there was a lot of assistance with regard to the acquisition from Marc van Eert, Frank Ambrosius, and Robert Wassens from Technolution. Lastly, I would like to thank Radim Šejnoha and Bohuslav Sed′a from Thermo Scientific for their help with the SEM.

# BIBLIOGRAPHY


[1] T. scientific. "Apreo 2 sem". (2021), [Online]. Available: https://www.thermofisher.com/nl/en/home/electron-microscopy/products/scanning-electron-microscopes/apreo-sem.html.

[2] Thorlabs. "Gvs212/m - 2d large beam (10 mm) diameter galvo systems". (2021), [Online]. Available: https://www.thorlabs.com/thorproduct.cfm?partnumber=GVS212/M (visited on 12/21/2021).

[3] J. Stopka, "Analytical formulae for trajectory displacement in electron beam and generalized slice method", *Ultramicroscopy*, vol. 217, p. 113 050, 2020.

[4] A. Mohammadi-Gheidari, *PhD Thesis: 196 Beams in a Scanning Electron Microscope*. 2013, ISBN: 9789461919854.

[5] Nikon. "Cfi plan apo lambda 40xc". (2021), [Online]. Available: https://www.microscope.healthcare.nikon.com/products/optics/selector/comparison/-1848 (visited on 12/21/2021).

[6] Hamamatsu. "Mppc s14160/s14161 series". (2021), [Online]. Available: https://www.hamamatsu.com/resources/pdf/ssd/s14160_s14161_series_kapd1064e.pdf (visited on 12/21/2021).

[7] D. Drouin, A. R. Couture, D. Joly, X. Tastet, V. Aimez, and R. Gauvin, "CASINO V2.42 - A fast and easy-to-use modeling tool for scanning electron microscopy and microanalysis users", *Scanning*, vol. 29, no. 3, pp. 92–101, 2007. DOI: 10.1002/sca.20000.

[8] J. Schindelin, I. Arganda-Carreras, E. Frise, *et al.*, "Fiji: An open-source platform for biological-image analysis", *Nature methods*, vol. 9, no. 7, pp. 676–682, 2012.

[9] S. Preibisch, S. Saalfeld, and P. Tomancak, "Globally optimal stitching of tiled 3d microscopic image acquisitions", *Bioinformatics*, vol. 25, no. 11, pp. 1463–1465, 2009.

[10] J. Stopka and P. Kruit, "Statistical coulomb interactions in multi-beam sem", *International Journal of Modern Physics A*, vol. 34, no. 36, p. 1 942 021, 2019.

[11] J. Stopka, W. Zuidema, and P. Kruit, "Trajectory displacement in a multi beam scanning electron microscope", *Ultramicroscopy*, vol. 223, p. 113 223, 2021.

# 6

# VALORIZATION OF THE DELFT MULTI BEAM SEM

In the third year of this research, the valorization of the prototype commenced. In the preceding years, we demonstrated the feasibility of obtaining high-quality contrast images using the imaging technique described in chapter 2. The original objective was to demonstrate imaging using secondary electrons and incorporate it as one of the imaging modalities in the SEM. Secondary electron imaging offered several advantages, primarily because researchers were familiar with the technique. Zeiss had previously shown the possibility of imaging biological tissue using secondary electrons in a multi-beam configuration. Even though secondary electrons were detected, it was still believed that the primary contrast mechanism was mainly derived from backscattered electrons. These electrons induced secondary electrons in the material, which were then detected (referred to as SE2's). Ren [1] demonstrated that, with certain techniques, this imaging was also achievable in the initial prototype in Delft. However, there were significant limitations in the imaging process, including low detection efficiency. To overcome this limitation, a completely new column design was necessary. From the beginning, the goal was to retrofit an existing single-beam SEM and transform it into an MBSEM. Consequently, secondary electron imaging was no longer considered a viable imaging modality.

To make the development possible, a consortium was created with three companies and the Delft University of Technology. Technolution B.V. provided its expertise in electronics and signal processing, Delmic B.V. served as a system integrator with knowledge in detection optics and stage design, and Thermo Scientific handled everything related to the scanning electron microscope. The po-

sition of TU Delft was primarily advisory and as the owner of some of the intellectual property.

Before constructing the first prototype, several decisions needed to be made. First and foremost, the column used in the initial TU Delft prototype, based on the FEI Nova NanoSEM, had recently been discontinued and could not be used. Other options had various benefits that needed careful consideration, such as beam deceleration in the final lens (beneficial for maximum current at high resolution), electrostatic scanning (beneficial for throughput), the existence of an intermediate lens (also beneficial for maximum current at high resolution), and cost. Unfortunately, no single column contained all the optimal features, so it was eventually decided that modifying the Nicole column currently in production by Thermo Fisher Scientific, as used for their Apreo 2 SEM, would be the best option. This also fixed the number of beams and the pitch between them, optimized for this specific column. In the early prototypes, 196 beams were employed, with each beam delivering up to 1nA of current. Due to the high beam energy (15keV) in this prototype, Coulomb interactions were not problematic. However, realizing that lower energy electrons would provide better contrast, the Coulomb interactions in the new column had to be optimized for, leading to a reduction in the number of beams. The pitch was then optimized for a combination of throughput and resolution.



Another crucial decision was how to handle the scanning beams on the detector. To make a well-informed decision, the Delft prototype (with the old Elstar column) was used as a Functional Model alpha (FuMo alpha). In this functional model, the performance of the scanning stage and the silicon photomultiplier detector array was assessed. It was discovered that while the scanning stage worked well outside of a vacuum, the lack of lubrication caused issues in the SEM vacuum chamber. Descan mirrors were added to the same optical system to assess the option of "step and scan" imaging, which quickly showed promising results, leading to the decision to adopt this approach. To advance further in the development, a second microscope, FuMo beta, was constructed. This prototype was based on an Apreo SEM, with simple prototype models of the electron optics, detector optics, and the detection system. Important lessons were learned about the scanning system, detector optics, and suggested upgrades for the electron optics. The process of going through two functional models before the final build proved highly successful, as it eliminated the need for exhaustive theoretical discussions and provided relatively quick answers to critical questions. All concepts were first explored in the two functional models before being incorporated into the final system.

Although the assessment showed a well-functioning MBSEM, the system still heavily relied on manual calibrations and settings. Implementing these manual

calibrations into automated systems proved to be a substantial task and caused significant project delays. It is challenging to address this issue since the hardware must be operational before certain software features can be implemented. While functional models were beneficial for hardware development, they were not always suitable for software development. This should be considered and planned for in any project of this nature.

## 6.1. FINAL FAST-EM CONFIGURATION

The final system now available on the market and sold by Delmic B.V. has different specifications from the prototype used in chapter 5. These specifications are listed below, along with a brief explanation:

- 1nA per beam current.
- To overcome the Coulomb interactions present in a system with 1nA per beam, an additional intermediate lens is added to the electron optical system.
- Fast beam shift interface to correct for stage inaccuracies. No post-processing is required to stitch fields.
- Extended beam shift range to allow for multi-field imaging.
- Picoscale [2] laser interferometer supplied by SmarAct GmbH to measure the stage position and correct for its inaccuracies.
- A stage with a 150ms settling time and a range to cover 9 scintillators of 15mm×15mm.
- A light optical focus tracker to keep both the electron and light optical systems in focus during acquisition.
- An integrated, motor-actuated k-mirror [3], [4] designed and produced by Delmic B.V. Used for the optical rotation of the optical path, eliminating the need to rotate the detector.
- Faster galvo-mirrors produced by Scanlab, allowing for dwell times as low as 400ns [5].

As of the current writing, this system has been in the field for 2.5 years. During this time, a significant amount of imaging was performed, and various upgrades were added to the system. The source module was redesigned, the scintillator production process was improved, the calibrations outlined in the previous chapter were fully automated, and a graphical user interface was finalized.

The consortium is still addressing some remaining issues, demonstrating that even though a product is finalized and has been on the market for a significant amount of time, development never truly ceases.

# 7

# CONCLUSION

In this thesis, the design and engineering considerations for a multi-beam scanning electron microscope (MBSEM) are discussed. This microscope can benefit biological research in various ways. It can provide new insights into the inner workings of a multitude of biological systems that were hard to obtain using previously existing instrumentation. For instance, a higher throughput gives the option to perform statistical analysis on multiple samples instead of concluding only one or a few snapshot images of one sample. In chapter 1, some questions were posed regarding the transmission imaging implemented in this MBSEM. We have reached the following conclusions in this thesis:

- Transmission imaging with a section directly placed on a scintillator provides good images, and there is a landing energy (around 5keV) where the product of the CNR and SNR of the imaging method shows a maximum. This optimum energy, however, varies with the sample, and therefore the energy is still selectable in the product.
- Scintillator surface quality is crucial; scratches on either its surface or the coating layer will deteriorate imaging. Ion beam polishing was found to be the best method for obtaining good surface quality.
- Granularity in the coating layer is visible in transmission imaging. Boron shows the lowest amount of granularity in the coating, while Molybdenum is a second option with slightly more granularity.
- Lower energies ($\lesssim$4keV) for thicker sections ($\gtrsim$ 60nm) yield lower resolution due to beam spreading in the sample.

- YAG:CE as a scintillator is a good substrate for transmission imaging. It provides a good amount of light, is cost-effective, and its emission spectrum matches well with the selected detectors. Plastic scintillators are not an option due to fast bleaching.

To implement this imaging modality in a commercial system, several analyses and tests were performed, leading to the following conclusions:

- Silicon photomultiplier arrays are a well-suited detector as they are fast and sensitive with a large dynamic range.
- Scanning the electron beams of the grid in just one direction and using the stage for the scan in the other directions is theoretically possible but places very high requirements on the stage (accuracy and stability), electron optics (grid distortions), and scanning system (overhead).
- Descanning of the detection signal using descan mirrors is easily implemented and yields good images.
- Replacing some of the necessary stage movements with an electron beam step and scan procedure using beam shifts can increase the throughput of a multi-beam system by up to a factor of two at dwell times lower than 500ns. The beam shift has a settling time that is a factor of 100 lower than that of a suitable scan stage.



In order to simplify the design from an academic prototype to an actual product, several choices had to be made:

- With a relatively slow scanning system (magnetic scanning) and common stage settling times (greater than 150ms), it is better to opt for a low number of beams with a large pitch than for a high number of beams with a small pitch. The main consideration for this is sustained throughput.
- From a light optical perspective, it is easier to have a fixed pitch than to have a variable pitch.
- Only transmission imaging on a scintillator was implemented, which performs better than backscatter imaging of heavy metal-stained embedded tissue sections.

For the user to be able to use the system properly, several alignment protocols are required. In this thesis, the following alignments were identified and protocols developed:

- Light optics to electron optics alignment
- Beam scan direction alignment
- Beam spots to detector alignment
- Descan alignment
- Scan amplitude
- Grid distortion correction by use of a second stigmator
- Dark level and gain calibration

Finally, we built a system that can theoretically achieve a maximum throughput of 400Mpix/s. At the end of this research, the system showed a maximum throughput of 50Mpix/s at a dwell time of 1µs. Multiple software upgrades have to be implemented to reach the highest achievable speed. At the current speed, however, the system is ready to help researchers gain new insights into the field of biology. A major hurdle, however, will be the automated interpretation of the images, which is currently a large bottleneck to the final workflow throughput.

# ACKNOWLEDGEMENTS

Pieter, thank you for being my promotor and guiding my development through these years. Thanks especially for explaining Physics in a way I never thought of before. Your support has been invaluable in the completion of this thesis. Jacob, thanks for your (co)supervision and always helping in the discussions about the system.

When I started this project, I had enormous help from Yan Ren, my predecessor. I started out with limited knowledge of optics and electron microscopy; you pointed me in the right direction. After that, I relied on the technical knowledge of Dustin Laur. Dustin, you supported me when I wanted to take something apart, engineer the (almost) impossible, or destroy something. Besides work, I have also enjoyed bartending together in TPKV most Fridays' and your kind friendship.

Thanks also to Paul Keizer, Shammi Rahangdale, and Lennard Voortman for their help on imaging with the first prototype. Without your input, I couldn't have created the first, somewhat good-looking, multi-beam transmission images.

I look back fondly on working in the Charged Particle Optics group. Kees, I have always had great discussions with you - both on the project and otherwise. The long days of experiments were made easier by the excellent camaraderie within the group. My good friends "Gerwrard" and Kerim have since moved to the United States - I will always cherish our time together. I've enjoyed the daily coffee ritual and the weekly work discussions with the rest of the PhDs and technicians in the group: Carel, Gaudhaman, Han, Hideto, Jayson, Jan, Johan, Leon, Marijke, Sangeetha, Thomas, Robert, Dušan, and more recently, Laura, Yoram, Mathijs, Vidya, Ryan and Aya.

I would also like to thank the support from Delmic, especially Sander, who believed in the project from very early on. Some of this work would have been impossible without the help of Andries, who always has great ideas on how to move forward.

From high school, I had two great examples, and finally, I can follow in their footsteps of becoming a doctor of philosophy. Gerrit and Mart Johan, I'm so glad we could be each other's paranymphs, and now, with my defense, we complete the circle.

During this time, it was great to get away and spend many evenings at Locus Publicus. It is sometimes hard to remember those evenings, but I am reasonably

sure it was great to hang with the friends I made during my time in Delft: Danilo, Sid, PP, Jett, Ashwath, and Waltie. Big thanks to my family for consistently believing that I could finish this thesis.

Last but not least, I would like to thank my best friend and life partner, Aditi. This work led me to you, and for that alone, it is already worth it. It's incredible to think that when we first met in Pieter's office, we had no idea that our journey would lead us to start a family together (hi Cheenu!). You both mean the world to me.

# List of Publications

10. **Fermie, J., Zuidema, W., Šejnoha, R., Wolters, A., Giepmans, B., Hoogenboom, J., & Kruit, P.** , *High-throughput imaging of biological samples with Delmic's FAST-EM.*, Microscopy and Microanalysis, 27(S1), 558-560. (2021).

9. **Stopka, J., Zuidema, W., & Kruit, P.** , *Trajectory displacement in a multi beam scanning electron microscope.*, Ultramicroscopy, 223, 113223. (2021).

8. **Zuidema, W., & Kruit, P. (2020).** , *Transmission imaging on a scintillator in a scanning electron microscope.*, Ultramicroscopy, 218, 113055. (2020).

7. **Fermie, J., Zuidema, W., Wolters, A. H. G., Giepmans, B. N., & Hoogenboom, J. P.**, *Rapid and Seamless Imaging of Biological Specimens Using a Novel Optical Scanning Transmission Electron Detector.*, European Microscopy Congress 2020.(2020).

6. **Hoogenboom, J. P., & Zuidema, W.** , *Method for inspecting a sample in a charged particle microscope.*, Patent: OCT-17-084 (2020).

5. **Kruit, P., & Zuidema, W.** , *A dedicated multi-beam SEM for transmission imaging of thin samples.* , Microscopy and Microanalysis, 25(S2), 1034-1035.(2019).

4. **Zuidema, W., Hoogenboom, J. P., & Kruit, P.** , *Improved Image Quality in SEM Imaging of Thin Tissue Sections.* , Microscopy and Microanalysis, 23(S1), 564-565.(2017).

3. **Hemelaar, S. R., De Boer, P., Chipaux, M., Zuidema, W., Hamoh, T., Martinez, F. P., ... & Schirhagl, R.** , *Nanodiamonds as multi-purpose labels for microscopy.* , Scientific reports, 7(1), 1-9.(2017).

2. **Zuidema, W., Ren, Y., Hoogenboom, J., Hagen, C. and Kruit, P.,** , *Transmission imaging of biological tissue with the Delft multi-beam SEM.* , European Microscopy Congress 2016: Proceedings (pp. 394-395).(2016).

1. **Zuidema, W.**, *Investigation of the coarse grained heat-affected zone microstructure and hardness of multipass welded X65 linepipe steel.* , Delft Univeristy of Technology (2015).